universität wien

DISSERTATION | DOCTORAL THESIS

Titel | Title

Ion-Laser-Interaction Mass Spectrometry of ^{90}Sr for industrial scale operation

verfasst von | submitted by

Oscar Marchhart BSc MSc

angestrebter akademischer Grad | in partial fulfilment of the requirements for the degree of

Doktor der Naturwissenschaften (Dr.rer.nat.)

Wien | Vienna, 2025

Studienkennzahl lt. Studienblatt | Degree programme code as it appears on the student record sheet:	UA 796 605 411
Dissertationsgebiet lt. Studienblatt | Field of study as it appears on the student record sheet:	Physik
Betreut von | Supervisor:	Dr. Dennis Mücher Univ.-Prof. i.R. Dipl.-Ing. Dr. Robin Golser

Ion-Laser-Interaction Mass Spectrometry of ^{90}Sr for industrial scale operation

Doctoral thesis

for

the award of the doctoral degree,

accepted as a Cotutelle de thèse by
the Faculty of Mathematics and Natural Sciences
of the University of Cologne
&
the Faculty of Physics of the University of Vienna

submitted by

Oscar Marchhart, BSc, Msc

accepted in the year 2026

Acknowledgements

I would like to express my deepest gratitude Prof. Robin Golser for believing in me and giving me the opportunity to do my PhD-thesis. I am also grateful that he provided the majority of the funding, as well as his support throughout all stages of the thesis.
Since my thesis is a Cotutelle de thèse, I would also like to thank Prof. Dennis Mücher for supporting this project and taking on the role of supervisor of from the partner university. In addition, I would like to thank Prof. Tibor Dunai and Dr. Erik Strub for funding the rest of my PhD-thesis.
I also want to thank the entire VERA staff team for their support, especially Alfred Priller and Peter Steier for their continuous software related and technical support concerning the test bench setup at VERA. Silke Merchel for her help, expertise, and patience regarding all chemical related questions, as well as for her help in the chemistry lab. Martin Martschini for always being wiling to lend an ear and helping out with his ion cooler expertise whenever needed. Ewald Friedl from the workshop for helping me with electrical issues at the test bench and for producing new cathodes for the ion source. Helga Schmelzer-Vincro and Sigrid Lielacher for their support in all bureaucratic matters and Stefan Lehr for cooking delicious meals on "Nudeldonnerstag".
I feel indebted to Markus Schiffer, with who I worked closely at the test bench setup, construction of the ALIS setup, and conducting the AMS measurements at CologneAMS. He supported me throughout the thesis, helping me to overcome all physics related problems.
Additionally, I want to thank the entire AMS group of CologneAMS for being so welcoming, which made my stay at Cologne much easier. Special thanks to Stefan, Gereon, Timm-Florian, and Derin for their help at the ALIS setup.
I want to thank my colleagues Alexander Wieser, Michael Kern, Andreas Wiederin, Stephanie Adler, Janis Wolf, Daniel Baumgartner, Felix Albrecht, Sophie Schoberleitner, Tabea Fuchs, Esad Hrnjic, Clemens Unterweger and Dennis Ibrahimovic for the fun atmosphere in the office and for all the fruitful discussions and rants.

Finally, I want to thank my parents, Christian and Karin, from the bottom of my heart for all the support, not only during the dissertation. I am deeply indebted to everything they have done and sacrificed for me throughout my life. Additionally, I also want to thank my siblings for always being by my side. Ultimately, I am grateful for my family, for their support, and for always enduring me.

Abstract

^{90}Sr ($T_{1/2}$ = 28.91 a) is highly radiotoxic nuclide produced with high yield in nuclear fission. Its origin in the environment and global distribution is almost exclusively of anthropogenic nature through releases from atmospheric nuclear weapons tests, nuclear power plants or nuclear fuel reprocessing plants. This work demonstrates the feasibility of measuring ^{90}Sr in soil and concrete samples on an industrial scale, i.e., processing and measuring hundreds to a thousand samples per year, using ion-laser-interaction assisted accelerator mass spectrometry (AMS).
In a collaboration between the University of Cologne and the University of Vienna a new ion cooler design has been developed, built and its performance has been tested. The new design features elliptically shaped injection and extraction electrodes, as well as a new guiding electrode structure. The guiding field strength produced by the guiding electrodes (5 - 20 V/m), has a noticeable effect on the ion residence time, which typically ranges from a few to tens of ms. Overall, ion cooler transmissions of up to 30% have been achieved for $^{27}AlO^-$ and $^{63}Cu^-$ beams and up to 25% for $^{88}SrF_3^-$.
First AMS measurements of ^{90}Sr were successfully conducted with the Anion Laser Isobar Separator (ALIS) setup at the 6 MV accelerator of CologneAMS. A blank level of $^{90}Sr/Sr = (6.94 \pm 4.29) \cdot 10^{-13}$ was achieved, which corresponds to a limit of detection of 11 mBq. Reference material from the 10^{-11} range down to the 10^{-12} range has been successfully measured, and their linearity was reproduced. For AMS measurements, the 3+ charge state is used at a terminal voltage of 5 MV with an accelerator transmission of 22%. ALIS achieves an isobar suppression of up to $3 \cdot 10^2$ using a He buffer gas in conjunction with a 532 nm laser. Furthermore, the extraction of SrF_3^- results in a Zr suppression of $< 3 \cdot 10^3$ in the ion source and the Zr suppression in the detector reaches up to 10^2, yielding a total ^{90}Zr suppression of $> 10^6$.
A new chemical sample preparation protocol for AMS measurements of ^{90}Sr in soil and concrete samples has been developed. The processing of one sample batch, which generally contains between six and ten samples, requires approximately 40 h of working time, with a projected completion time of four to five working days. With the current protocol one person could process between 350 - 520 samples per year. The validity of the sample preparation has been successfully verified at VERA, measuring IAEA reference material for soil samples and by comparison of LSC results with the AMS results for concrete samples. With the new sample

preparation protocol, high chemical yields and quality factors around 90% are achieved for both concrete and soil. It has been demonstrated that samples in the range of 100 mg up to 10 g yield accurate AMS results. For large samples (> 5 g), this is achieved by a "leachate aliquot" approach. In this approach, the entire sample is leached, but only a small liquid aliquot is further processed. Nevertheless, the obtained AMS result is still representative for the whole sample. Furthermore, the AMS measurement efficiency of ^{90}Sr was improved by up to 70% due to higher counting statistics coming from better performance of the processed samples.

Zusammenfassung

^{90}Sr ($T_{1/2} = 28.91$ a) ist ein hochgradig radiotoxisches Nuklid, das mit hoher Ausbeute bei der Kernspaltung entsteht. Der Ursprung und die globale Verbreitung sind durch Freisetzungen aus atmosphärischen Kernwaffentests, Kernkraftwerken oder Wiederaufbereitungsanlagen nahezu ausschließlich anthropogener Natur. Die Arbeit demonstriert die Durchführbarkeit der Messung von ^{90}Sr Messung im industriellen Maßstab in Boden- und Betonproben, d.h. die Verarbeitung und Messung von Hunderten bis tausend von Proben pro Jahr, mittels durch Ionen-Laser-Wechselwirkung unterstützte Beschleunigermassenspektrometrie (AMS).
Im Rahmen einer Zusammenarbeit zwischen der Universität zu Köln und der Universität Wien wurde ein neuer Ionenkühler entwickelt, gebaut und seine Funktionalität getestet. Das neue Design verfügt über elliptisch geformte Injektions- und Extraktionselektroden sowei eine neuartige Leitelektrodenstruktur. Die von den Leitelektroden erzeugte elektrische Feldstärke (5 - 20 V/m) wirkt sich spürbar auf die Aufenthaltsdauer der Ionen aus, die typischerweise einige ms bis einige zehn ms beträgt. Für $^{27}AlO^-$ und $^{63}Cu^-$ wurden Ionenkühlertransmissionen von bis zu 30% und für $^{88}SrF_3^-$ von bis zu 25% erreicht.
Am 6 MV Beschleuniger von CologneAMS wurden erste erfolgreiche AMS Messungen von ^{90}Sr mit dem Anion Laser Isobar Separator (ALIS) durchgeführt. Dabei wurde ein Blanklevel von $^{90}Sr/Sr = (6{,}94 \pm 4{,}29) \cdot 10^{-13}$ erreicht, was einer Nachweisgrenze von 11 mBq entspricht. Referenzmaterial im Bereich von 10^{-11} bis 10^{-12} wurden erfolgreich gemessen und die Linearität konnte reproduziert werden. Für die AMS Messungen wurde der 3+ Ladungszustand verwendet, welcher bei einer Terminalspannung von 5 MV eine Transmission von 22% hat. ALIS, mit He als Puffergas und einem 532 nm-Laser, erreicht eine Isobarenunterdrückung von bis zu $3 \cdot 10^2$. Die Extraktion von SrF_3^- aus der Ionenquelle führt zu einer Zr Unterdrückung von $< 3 \cdot 10^3$ und im Detektor wird eine Unterdrückung von bis zu 10^2 erreicht, wodurch eine Gesamtunderückung von $> 10^6$ für ^{90}Zr erzielt wird.
Für AMS Messungen von ^{90}Sr in Boden- und Betonproben wurde desweiteren eine verbesserte chemische Probenaufbereitung entwickelt. Die neue Aufbereitung eines Probenbatches, welcher üblicherweise aus sechs bis zehn Proben besteht, benötigt ca. 40 h, wodurch sie in vier bis fünf Arbeitstagen durchführbar ist. Eine Person ist dadurch in der Lage jährlich zwischen 350 - 520 Proben aufzubereiten. Die Validität wurde bei VERA für Bodenproben durch Messungen von IAEA-Referenzmaterialien und für Betonproben durch den Vergleich von LSC Ergebnissen

mit den AMS Ergebnissen überprüft. Mit der neuen Probenaufbereitung werden hohe chemische Ausbeuten und "Quality Faktoren" erzielt, welche für Boden- und Betonproben im Bereich von 90% liegen. Es wurde gezeigt, dass Proben im Bereich von 100 mg bis 10 g genaue AMS-Ergebnisse liefern. Bei großen Proben (> 5 g) wird dies durch einen "Auslaugungsaliquot"-Ansatz erreicht. Bei diesem Ansatz wird die gesamte Probe ausgelaugt, aber nur eine kleines Flüssigkeitsaliquot weiterverarbeitet. Dennoch erhält man durch die AMS Messung weiterhin ein genaues Resultat, welches repräsentativ für die gesamte Probe ist. Desweiteren wurde durch die neue Aufbereitung die Zählstatistik von AMS Messungen von ^{90}Sr wurde verbessert, wodurch die Messeffizienz um bis zu 70% steigt.

Contents

1. Introduction **1**

1.1. Accelerator Mass Spectrometry 1
1.2. The radionuclide ^{90}Sr 5
1.2.1. Production of ^{90}Sr 5
1.2.1.1. Nuclear fission 5
1.2.1.2. Natural and anthropogenic occurrence 7
1.2.2. Measurement methods for ^{90}Sr 9
1.2.2.1. Radiometric method 9
1.2.2.2. Ion-laser-interaction assisted AMS 9
1.2.2.3. Other mass spectrometric techniques 10
1.2.3. Clearance level of ^{90}Sr 11
1.2.4. AVR - a nuclear high-temperature gas reactor 12
1.2.5. Applications of ^{90}Sr 13
1.3. Novel technique for low-energy isobar suppression using RFQ ion guides 15
1.3.1. Mathieu equations and ion motion 15
1.3.2. Laser photodetachment 16
1.3.3. Buffer gas cooling 19
1.3.4. Anion Laser Isobar Separator - ALIS 20

2. Performance tests of the RFQ ion guide at Vienna **25**

2.1. Test bench setup 25
2.2. Ion optics 27
2.3. Ion cooler transmission 28
2.4. Injection into the RFQ ion cooler 31
2.5. Ion residence time 34

3. Development and validation of a new sample preparation protocol for AMS measurements of ^{90}Sr in concrete and soil at VERA **39**

3.1. AMS measurement routine at VERA 39
3.2. Analyzed samples 41
3.3. Aim of the AMS sample preparation 44

3.4. Investigated modifications for potential improvements of the sample preparation . . . 46
3.4.1. AMS results of the investigated modifications . . . 48
3.5. New sample preparation protocol for ^{90}Sr in concrete and soil . . . 50
3.6. Validation of the sample preparation . . . 54
3.6.1. AMS results of the soil samples . . . 54
3.6.2. AMS results of the concrete samples . . . 56
3.7. Target performance of processed samples . . . 60

4. Investigations and AMS measurements of environmental samples after validation of the newly developed protocol 63
4.1. Modification of the newly developed protocol for potential cost reduction . . . 63
4.1.1. AMS results of the cost reduction tests . . . 65
4.2. Analyzed samples . . . 68
4.3. Sample preparation of the Rur river samples . . . 71
4.3.1. AMS results of the Rur river samples . . . 72
4.4. AMS results of the contaminated soil samples . . . 75
4.5. AMS results of the nuclear reactor concrete samples . . . 78
4.6. Target performance of processed samples . . . 79

5. Development of an ion-laser assisted AMS measurement routine for ^{90}Sr at CologneAMS 81
5.1. Setting up the ion source and ion source performance . . . 81
5.1.1. Positioning of the ion source . . . 81
5.1.2. SrF_3^- and ZrF_3^- molecule formation in the ion source . . . 86
5.1.3. Ionization yield of SrF_3^- . . . 88
5.2. AMS measurements and performances . . . 90
5.2.1. AMS measurement routine at CologneAMS . . . 91
5.2.2. Isobar suppression . . . 93
5.2.2.1. Isobar suppression in the ion source . . . 93
5.2.2.2. Isobar suppression with ALIS . . . 93
5.2.2.3. Isobar suppression in the detector . . . 97
5.2.2.4. Overall isobar suppression . . . 99
5.2.3. Ion cooler transmission . . . 99
5.2.4. Accelerator transmission and charge state yield . . . 100
5.2.5. Transmission throughout the facility . . . 104
5.2.6. Overall detection efficiency . . . 105
5.3. AMS results for ^{90}Sr . . . 106
5.3.1. Blank level . . . 106
5.3.2. Reference materials . . . 107

6. Conclusion and Outlook **111**

Appendix A. Code of ion optic simulations at Vienna **115**

Appendix B. Rur river batch: Additional sample information **119**

Appendix C. Complete sample list of all processed samples **121**

Bibiliography **125**

1. Introduction

1.1. Accelerator Mass Spectrometry

Accelerator Mass Spectrometry (AMS) is the most sensitive method for the detection of long-lived trace nuclides with the highest efficiency. AMS is capable of measuring isotopic abundances in the range of 10^{-12} – 10^{-16} by almost complete suppression of isobaric interference. Hence, AMS is a multidisciplinary technique which is used in a variety of different fields of research, e.g., archaeology, astrophysics, geology, oceanography among others [1, 2].

One of the major advantages of AMS over radiometric measurements is that it is feasible for trace isotopes with half-lives in the range of $T_{1/2} \geq 1000\,\mathrm{a}$, as the material and time required for radiometric measurements would vastly exceed the time, efficiency and cost of AMS measurements. Whereas AMS typically requires only one gram or less of sample material and a few hours of measuring for sufficient counting statistics, radiometric methods on average need much larger amounts of material, sometimes up to kg, and longer counting times for similar statistics [3, 4].

In general, the sensitivity limit of mass spectrometric methods (MS), i.e., inductively coupled plasma mass spectrometry (ICP-MS), resonance ionization mass spectrometry (RIMS), thermal ionization mass spectrometry (TIMS) and AMS suffer from the interference of isobars. The utilization of a tandem accelerator enables AMS to accelerate ions up to the MeV range. During acceleration, the injected anions undergo charge exchange and molecules are dissociated, including isobaric molecules. Subsequently, the fragments are separated from the isotope of interest using a mass spectrometer. This drastically reduces the isobaric background.

Typical AMS facilities consist of an ion source, producing negatively charged ions; two mass spectrometers, i.e., a combination of electric and magnetic components used as filters; an accelerator (tandem accelerator); and a detector.

Ion source

At the beginning of every AMS facility an ion source is located. In most cases, a source of negative ions by cesium sputtering (SNICS) [5, 6] from National Electronic Corporation (NEC), High Voltage Engineering (HVE) [7], or Ion Plus [8] is used to produce an anionic ion beam with tens of keV of energy. For the sputtering process, solid target material is pressed into cathodes, which are typically either made of copper or aluminum. Either one cathode is inserted into the ion source at a time, or several cathodes are inserted simultaneously using a multi-cathode wheel. The cesium used for sputtering evaporates in an oven and flows into the ion source area. Cs atoms are positively ionized on the hot surface of the ionizer. Applying a negative potential of a few kV to the cathode, Cs beam is accelerated towards the sample and the sample material is sputtered, whereby all negatively charged anions are extracted out of the ion source. A small Cs layer condensates on the cathode surface increasing the yield of negative ions produced in the ion source [5, 6].

Principles of mass spectrometry

After extraction the ion beam with energies in the keV range, the ion beam is filtered with a mass spectrometer according to the mass over charge (m/q) ratio. A mass spectrometer is a combination of an electrostatic analyzer (ESA) and a bending magnet (BM), exploiting differences in the circular motion of charged particles with different energy and mass in an electric or magnetic field due to the Lorentz force to ultimately filter a specific m/q ratio [9].

The ESA consists of two cylindrical or spherical electrodes with a potential difference between them. For a stable circular trajectory of the charged particle, the centripetal force and the Lorentz force have to be of equal magnitude, yielding the following equation

$$\frac{mv^2}{r} = qE \tag{1.1}$$

where m is the mass of the particle, q is the charge of the particle, r is the radius of the circular motion, v is the velocity of the particle, and E is the electric field between the electrodes. Substituting the kinetic energy $E_{kin} = \frac{mv^2}{2}$ of the particle into eq. 1.1 and rearranging some of the parameters yields

$$\frac{E_{kin}}{q} = \frac{rE}{2} = const. \tag{1.2}$$

For a charged particle, this equation is constant for a fixed electric field and geometry of the ESA, i.e., fixed bending radius. Therefore, an ESA acts as an energy over charge filter (E/q).

The bending magnet consists of two pole shoes with opposite magnetic polarity, typically generated by electromagnets. Inside the gap of the pole shoes of BM a constant and homogeneous magnetic field is present. The charged particles are, in turn, forced on a circular motion inside the BM. The same argument as for the ESA can be applied in the presence of a magnetic field to obtain

$$\frac{mv^2}{r} = qvB \tag{1.3}$$

where B is the magnetic field between the pole shoes, m,v r and q are identical to the parameters used in eq. 1.1. Substituting $p = mv^2$ into eq.1.3 yields

$$\frac{p}{q} = rB \tag{1.4}$$

where p is the momentum of the particle [10]. Hence, a BM as a standalone filter acts as a p/q filter. A final substitution of $p = \sqrt{2mE_{kin}}$ into eq. 1.4 results in

$$\frac{\sqrt{2mE_{kin}}}{q} = rB = const \tag{1.5}$$

which, similar to the ESA, is constant for a fixed geometry, magnetic field and kinetic energy (e.g. selected with an ESA). Therefore, using both components subsequently acts as an m/q filter. [9]

Tandem Acelerator

The m/q filtered anion beam is injected into the accelerator, the main component of any AMS facility. The accelerator has a positive terminal potential, which can

range from 200 kV up to 14 MV depending on the facility [2]. The injected anions are accelerated towards the terminal. In the center of the accelerator there is either a gas stripper or thin foils that remove electrons from the anions and changes their polarity so that they are accelerated with the same potential in the direction of the accelerator exit. The outcome of the positive charge state distribution depends on the terminal voltage and stripping medium. Generally, small molecules from light elements with charge state $\geq$3+ dissociate during the stripping process and only their fragments leave the accelerator [11–13]. However, this does not apply to actinides, e.g. UH^{3+} and ThH^{3+} [14]. In such cases other isobar suppression methods are required. After the accelerator, a second high-energy mass spectrometer filters the cationic ion beam for one specific charge state before entering a detector. Therefore, AMS is typically capable of completely suppressing molecular isobars and only elemental isobars as well as m/q interference remain. The suppression of highly abundant elemental isobars is more challenging as they can not be sufficiently separated from the isotope of interest with the high-energy mass spectrometer. In some rare cases, this can be avoided because some isobars do not form negative ions due to their negative electron affinities, e.g. ^{14}N, ^{26}Mg, ^{129}Xe. However, this is the exception, so other means of isobar suppression is required.

Detection and further isobar suppression methods

Commonly used detectors in AMS are gas ionization chambers (GIC) with split anodes. They exploit differences in energy-loss in matter, since the stopping power depends on the nuclear charge number, effectively separating isobars and m/q interferences from the isotope of interest in an energy-loss spectrum [15–17]. If the separation is insufficient, more sophisticated separation methods are required, e.g., gas-filled magnets can separate isobars by forming different average charge states through charge exchange interactions with the gas [18–21]. Alternatively, degrader foils [22, 23] or a foil stack in front of the detector entrance window [24] can be used. However, most of these methods only suppress the isobars sufficiently at high energies when accelerators with terminal voltages of ≥ 6 MV are used.

In the last decade, two new techniques for AMS have been developed that do not rely on the energy-loss in matter to separate elemental isobars from the isotope of interest. One uses a gas reaction cell to suppress the isobar via anion-gas

reactions [25–27]. The other one uses the interaction of a high intensity laser beam with the anion ion beam inside a gas-filled radiofrequency quadrupole (RFQ) [28, 29]. This technique will be referred to as ion-laser-interaction assisted AMS for the rest of this work. Both techniques, utilize RFQs to decelerate anions extracted from the ion source, typically in the keV range, down to a few eV or even lower. This is done to increase either the interaction time between the laser beam and the anion beam for laser photodetachment [28] or for electron transfer and ion dissociation reactions with the reaction gas within the reaction cell [30]. The Ion-Laser InterAction Mass Spectrometry (ILIAMS) setup at the Vienna Environmental Research Accelerator (VERA) [31] and the Isobar Separator for Anions [30, 32] have successfully demonstrated the isobaric suppression capabilities of these techniques for AMS.

1.2. The radionuclide ^{90}Sr

This section summarizes the most important information of the investigated radionuclide ^{90}Sr ($T_{1/2} = 28.9 \pm 0.04$ a [33]). This information also serves as motivation for the development of the new advanced RFQ ion cooler for rapid analysis of ^{90}Sr by ion-laser-interaction assisted AMS.

1.2.1. Production of ^{90}Sr

The trace nuclide ^{90}Sr is almost exclusively produced anthropogenically in nuclear fission reactors or by nuclear weapons, e.g., during the nuclear weapons test in the 1950s and 1960s. However, a minute amount is also produced naturally by spontaneous fission of ^{238}U in the Earth's crust.

1.2.1.1. Nuclear fission

Neutron induced fission of heavy nuclides, e.g., ^{233}U, ^{235}U, ^{239}Pu, into smaller fission fragments represents an exothermic reaction in which typically around 200 MeV are released, consisting of the kinetic energy of the primary fission products and the excitation energy of the fragments released via decay processes [34]. For each fission process typically two or three neutrons and two fission fragments

are produced. In rare cases, three or four fission fragments are produced called ternary and quaternary fission, respectively. For neutron induced fission by thermal neutrons (25 meV), the fission fragments differ significantly by mass and can be divided into two groups. The lighter fragments between 80 - 112 amu and the heavier fragments between 125 - 160 amu. However, the mass of the fragments of the lighter group heavily depend on the parent nuclide undergoing fission (see Fig. 1.1). The probability that products with the same mass are formed during fission increases with the energy of the incident neutron [34]. Since the produced fission fragments are neutron-rich, they decay towards the valley of stability through β^--decay. The cumulative fission yield is the integrated probability of an individual fission yield occurring in a specific isobaric decay chain. In other words, it is the sum of the fission yields in a decay chain up to the first stable or long-lived nuclide.

There are two classes of fissionable nuclides, fissile and fertile nuclides. Fissile nuclides have high neutron induced cross sections thus they will undergo fission

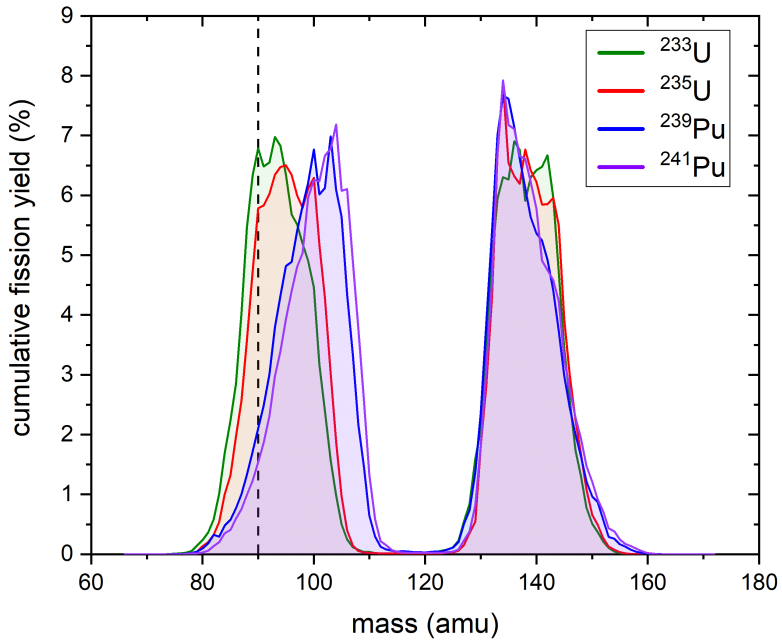

Figure 1.1.: Cumulative fission yield dependence on the mass of the fission fragments for thermal neutron induced fission of ^{233,235}U and ^{239,241}Pu. Note that the dashed line at mass 90 amu indicates the relevant cumulative fission yields for the production of ^{90}Sr. The shown data was taken from [35].

when bombarded by neutrons of any energy. In contrast, fertile nuclides have significantly lower cross sections, particularly for low-energy neutrons, and are more likely to capture the neutrons without undergoing fission. However, through neutron capture and subsequent radioactive decay fertile nuclides can transmute into fissile nuclides [34]. For example, ^{232}Th and ^{238}U are typical fertile nuclides which, after neutron capture, decay to ^{233}U and ^{239}Pu, which are fissile nuclides and therefore will undergo fission. Fertile nuclides may directly undergo fission if bombarded by high-energy neutrons in the MeV range due to a significantly higher cross section at high neutron energies [34]. In Fig. 1.2 the neutron induced fission cross section is plotted against the energy of the incident neutron for some uranium and plutonium nuclides, highlighting the difference in the cross section between fertile and fissile nuclides for thermal neutrons.

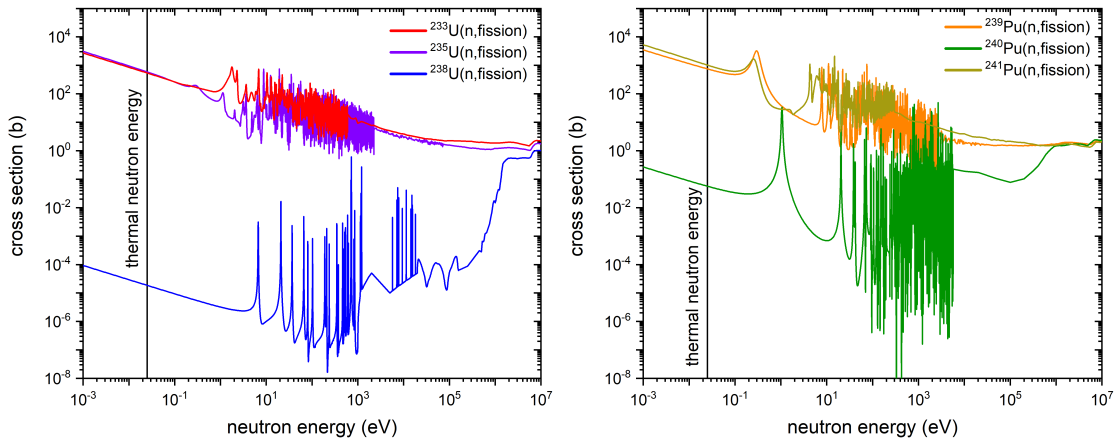

Figure 1.2.: Energy dependence of the neutron induced fission cross section for (a) ^{233,235,238}U and (b) ^{239,240,241}Pu. Depending on the cross section one can distinguish between fertile and fissile nuclides. The shown data was taken from [36]

1.2.1.2. Natural and anthropogenic occurrence

The natural occurrence of ^{90}Sr, produced through spontaneous fission of ^{238}U, can be estimated as follows. The natural abundances of uranium and strontium in the Earth's crust are 2.5 ppm and 340 ppm, respectively [37]. In addition, the natural abundances of ^{88}Sr and ^{238}U are 82.58% and 99.3%. Thus, the isotopic ratio of

^{88}Sr/^{238}U can be estimated to be 113 in the crust. Assuming secular equilibrium and a cumulative fission yield of ^{90}Sr between 5.41% [38] to 5.85% [35], yields an isotopic ratio of ^{90}Sr/^{238}U $\approx 2 \cdot 10^{-16}$. This leads to an estimated natural ratio of ^{90}Sr/^{88}Sr $\approx 1.8 \cdot 10^{-18}$, corresponding to an activity of 0.001 mBq/g. It is clear from this rough estimation that the measured activities of ^{90}Sr are almost exclusively due to human activity.

During the period from late 1940 to the early 1960s, an astonishing number of approximately 350 atmospheric thermonuclear bomb tests were conducted at various test sites in the northern hemisphere [39]. During this period, an estimated 600 PBq of ^{90}Sr was released. This includes releases of 2.37 TBq into the air at Hanford (USA), an inventory of 55.8,PBq from underground tests at the Nevada Test Site (USA) and tests from France in French Polynesia of 8.15 PBq [40]. In addition, the Meteorological Research Institute (MRI) in Tsukuba (Japan), conducted a series of measurements from 1959 to 1984 to obtain the deposition of ^{90}Sr at the MRI from thermonuclear tests, e.g., originating from Chinese tests. The cumulative amount of ^{90}Sr deposited over this period was estimated to be approximately 2.89 GBq/km^2, with annual deposition rates ranging from 0.56 MBq/km^2 to 706.7 MBq/km^2 [41].

Besides the bomb test, other contributions come from the nuclear fuel cycle. Since ^{90}Sr is produced during the fission of fuel elements, it will be stored in repositories after the fuel rods have been used and undergone reprocessing. One example of such a repository is the Yucca Mountain repository, where a total of approximately $9.69 \cdot 10^4$ PBq are stored [40]. Correctly processed and stored waste is not contributing significantly to the global environmental levels of strontium. However, accidents can happen during the operation of nuclear power plants, e.g., the Chernobyl (1986) and Fukushima (2011) accidents, which can release significant amounts of strontium into the environment. Around 10 PBq of ^{90}Sr was released during the Chernobyl accident [40, 42], compared to an estimated release of 0.4 PBq to 1 PBq into the Pacific Ocean following the Fukushima accident [43, 44].

Authorized releases of ^{90}Sr and other radioisotopes into the environment from reprocessing facilities, e.g., Sellafield (UK) and La Hague (France), represent another anthropogenic source of ^{90}Sr in the environment. At Sellafield, annual discharges

of ^{90}Sr from 1952 to 1992 into the Irish Sea varied between around 4 TBq/a to 500 TBq/a and discharges to the atmosphere were around 0 Bq/a up to 200 GBq/a [45].
A potential, albeit not yet significant, source of contribution is the unintended release through nuclear devices such as radioisotope thermal generator (RTG). These devices use radioisotopes, such as ^{90}Sr, to produce electricity (see section 1.2.5) and at least two losses of RTGs at sea with roughly 25 PBq and 1 PBq [46] are documented. In 2001, around 500 RTGs were in use globally, with a total activity of approximately 5000 PBq [46].

1.2.2. Measurement methods for ^{90}Sr

1.2.2.1. Radiometric method

The state-of-the-art detection method of ^{90}Sr ($T_{1/2} = 28.9 \pm 0.04$ a [33]) is via radiometric measurements of its daughter nuclide ^{90}Y ($T_{1/2} = 64.05 \pm 0.02$ h [33, 47]). Commonly used techniques for ^{90}Sr include liquid scintillation counting (LSC) and Cherenkov counting [3, 48, 49]. As ^{90}Sr is a pure and low-energy β^- emitter, a complex and thorough chemical separation of ^{90}Sr from all other emitting components is required prior to measurements, which is time-consuming [50]. Subsequently, roughly two weeks of waiting time is required to reach secular equilibrium of ^{90}Sr and ^{90}Y [50, 51]. Furthermore, relatively large amounts of sample material, e.g., tens of g up to kg, are required compared to AMS. Moreover, the measurement times of radiometric methods can surpass ten hours for low-level samples [3]. Some rapid methods exist that do not require to wait for secular equilibrium. However, these methods trade analytical turnover time in favor of lower precision and counting efficiency [50].

1.2.2.2. Ion-laser-interaction assisted AMS

Conventional accelerator mass spectrometry (AMS) facilities require large accelerators with terminal voltages ≥ 6 MV to measure ^{90}Sr. Nevertheless, even at high energies, only detection limits (LoD) around the radiometric limit of a few mBq are achieved [52, 53]. However, the utilization of ion-laser-interaction assisted AMS

has demonstrated the capability to achieve a substantially lower LoD on the order of $< 0.02\,\mathrm{mBq}$. This corresponds to a blank level of $^{90}\mathrm{Sr}/^{88}\mathrm{Sr} < (0.45 \pm 1.02)\cdot 10^{-15}$ [54], which represents a more than hundredfold improvement compared to radiometric methods and other techniques. Prior to the Anion Laser Isobar Separator (ALIS) setup at CologneAMS, ion-laser-interaction assisted AMS measurements were exclusively conducted using the Ion-Laser InterAction Mass Spectrometry (ILIAMS) setup at the Vienna Environmental Research Accelerator (VERA), as it was a globally unique setup at an AMS facility. At present, ILIAMS at VERA remains the sole setup that achieves the ultra-low LoD for ^{90}Sr as previously mentioned. The technique exploits differences in the electron affinities (EA) of atomic or molecular anions in order to neutralize the isobar via laser photodetachment, ion-gas reactions, or a combination of both [15, 31, 54, 55] (see section 1.3). Combined with conventional AMS, where molecular isobars are destroyed using an accelerator and the resulting fragments are separated by a high-energy mass spectrometer, this measurement technique achieves the utmost abundance sensitivity for all applicable nuclides. The high isobar suppression capabilities of ion-laser-interaction assisted AMS render the necessity of large accelerators for the efficient measurement of ^{90}Sr and other applicable nuclides redundant. Furthermore, the measurement of low-level samples can be achieved faster and with less material compared to their radiometric counter parts. Thus, ion-laser-interaction assisted AMS has the potential to provide a fast, highly sensitive and reliable alternative to radiometric measurements of ^{90}Sr. Furthermore, it enables the measurement of ^{90}Sr in ultra-low samples that exceed the LoDs of other techniques. However, at the cost of long measurement times.

1.2.2.3. Other mass spectrometric techniques

In general, mass spectrometric techniques such as inductively coupled mass spectrometry (ICP-MS), thermal ionization mass spectrometry (TIMS), resonant ionization mass spectrometry (RIMS) and conventional AMS do not require secular equilibrium in order to measure ^{90}Sr, which significantly decreases the potential analysis time. Currently, the LoDs of these techniques are typically close to the radiometric limit around a few mBq, as most of them suffer from interference of

the abundant isobar ^{90}Zr, requiring dedicated chemical isobar separation [52, 53, 56–59]. In special cases, TIMS achieves a LoD of around 1 µBq in samples with almost no stable Sr present ($< 10^{-7}$ Sr/g). Nevertheless, in typical environmental samples containing at least 100 μg of stable Sr, it is still around a few mBq [60]. To determine ^{90}Sr via conventional AMS, it is necessary to accelerate ^{90}Sr to high energies of typically ≥ 50 MeV to sufficiently separate ^{90}Sr from ^{90}Zr in the single particle detector [52, 53].

1.2.3. Clearance level of ^{90}Sr

In the event of disposing of potentially radioactively contaminated material, the measurement and clearance of the material is a prerequisite. Should the specific activity of a particular radionuclide not exceed the specified clearance level, it may be recycled or disposed of without regulations, otherwise the disposal is subject to regulations and recycling is prohibited. The clearance levels for each radionuclide is regulated individually for each country.In this work, the main focus will be on the regulations in Germany for ^{90}Sr, with an emphasis on soil and concrete as materials. However, most regulations regarding the clearance levels in Austria are very similar to Germany. They can be found in the Strahlenschutzverordnung of the country [61, 62].

In Germany, the clearance level for ^{90}Sr in soil samples is relatively low, with a threshold value of 2 mBq/g [61], which is close to the LoDs of conventional AMS and radiometric techniques [52]. The clearance level of concrete samples is significantly higher, with a threshold value of 0.6 Bq/g, for the disposal of $\geq$ 1000 t/a of construction waste and up to 1000 t/a in landfills [61]. There are even more levels for special cases, but these are the relevant ones for this work. To summarize, the clearance level for soil samples is very close to the radiometric LoD, and thus it would require large sample sizes to analyze the ^{90}Sr activity in a reasonable time. With regard to the LoD, it is sightly better for concrete samples. Nevertheless, the measurement of 1000 t or more per year necessitates a significant time investment required for chemical sample preparation and measurements.

Following Germany's decision in 2011 to phase out nuclear power, a substantial amount of material will require clearance measurements during the decommission-

ing of nuclear facilities. This is achieved via measurements of a select number of radionuclides as part of nuclide vectors. These nuclide vectors allow other radionuclides to be estimated without the need for specific measurements. Typically, ^{90}Sr is not included in nuclide vectors. However, in special cases, ^{90}Sr is also measured, e.g., the Arbeitsgemeinschaft Versuchsreaktor (AVR). Thus, ion-laser-interaction assisted AMS, which has a much lower LoD [31] and requires less material and measurement time per sample than radiometric measurements (see section 1.2.2), could be an interesting addition to ^{90}Sr measurements during the decommissioning of some nuclear facilities. Therefore, the University of Cologne and the University of Vienna collaborated to develop a new, advanced RFQ ion cooler. The goal was to increase the ^{90}Sr measurement efficiency and subsequently be able to handle an industrial scale sample throughput, i.e., on the order of hundreds to thousand of ^{90}Sr samples per year. Together with a newly developed sample preparation protocol, which is fast, simple and cost-efficient, it was demonstrated that ion-laser-interaction assisted AMS has the potential to be a competitive alternative or supplementary method to radiometric measurements (see chapter 3).

1.2.4. AVR - a nuclear high-temperature gas reactor

The AVR was a nuclear high-temperature gas reactor located in Jülich, Germany. A picture of the reactor building is shown in Fig. 1.3. Construction of the reactor began in 1960, and it was operational for 21 years from 1967 until 1988. During this period, there were several incidents, one of which occurred in 1978. This incident involved water ingress, resulting in a substantial transfer of ^{3}H and ^{90}Sr activity from the primary circuit to the ingressed water [63]. The contaminated water was partially released to the reactor building and the surrounding area. Ultimately, this incident led to the contamination of the reactor confinement, of the groundwater and soil surrounding the reactor [63, 64]. Another report states that traces of strontium and other fission products were found in the rainwater, ground and the gap between the reactor building and the hot workshop [65].
Specifically because of the 1978 incident specifically, the AVR has a significant and well-known contamination with ^{90}Sr in the concrete, as well as some contaminated soil in the local area. Since the reactor was shut down in 1988, it has been in

the decommissioning phase. Due to several incidents and known contamination with ^{90}Sr, the decommissioning process is time-consuming and expensive. Large amounts of potentially contaminated concrete and soil samples have to be measured in order to monitor the ^{90}Sr content. Concrete and soil can only be recycled or disposed of without regulations if the ^{90}Sr content is below the clearance limit. Hence, decommissioning is ongoing but progress is slow. Consequently, this makes it a valuable collaboration partner for the development of ^{90}Sr measurements in soil and concrete samples via AMS on an industrial scale.

Figure 1.3.: Picture of the AVR reactor site, a nuclear high-temperature reactor located in Jülich, Germany. © Jülich Research Center

1.2.5. Applications of ^{90}Sr

The highly radiotoxic nuclide ^{90}Sr is a produced with high yield in nuclear fission and highly mobility in the environment. Due to its chemical similarities to calcium, it is easily incorporated into bones or teeth after ingestion or inhalation [66]. In addition, its biological half-life is around 13.5 a following the uptake of ^{90}Sr in the human body [67, 68], meaning it can deposit a significant dose within a human lifetime and contribute the development of cancer, e.g., leukemia [69]. Therefore, regular monitoring of ^{90}Sr in the environment is important, especially after known

releases, as it poses a major health risk. During the decommissioning process of shut down nuclear reactors or power plants, a large number of samples must be analyzed to determine whether parts of the reactor site exceed the clearance level for a number of various fission nuclides. Such nuclides are typically LSC nuclides used in nuclear decommissioning, e.g., ^{41}Ca and ^{55}Fr [70, 71], or less common nuclides such as ^{90}Sr. Hence, fast analysis and high sample throughput are desirable for special cases such as ^{90}Sr at the AVR reactor.

Besides its application of monitoring ^{90}Sr in the environment due to potential health concerns, this divers trace nuclide has other applicants, such as acting as an environmental tracer. For example, it can be used to study vertical water mass mixing and sedimentation processes [72]. Due to its mobility in soils and groundwater, and its chemical similarity to calcium, the environmental migration behavior of ^{90}Sr, especially in plant/soil systems, is being investigated thoroughly [73, 74].

Additionally, it can also be used in medicine and industry. In medicine, ^{90}Sr/^{90}Y β-sources have a very niche use in brachytherapy, a type of radiation therapy where a sealed source is either placed inside or very close to the treated area. This can also be used to treat or prevent certain diseases, e.g., in-stent restenosis [75]. Another example of a medical application is the adjuvant treatment of conjuctival melanoma [76].

Its use in industry is also very diverse. Radioisotope thermal generators (RTG) are nuclear battery devices that produce an electric potential through the Seebeck effect, utilizing the heat generated by the radioactive decay. The main selling point of RTGs is their high reliability and longevity, and are used to power unmanned lighthouses, coast guard lights, satellites, or space exploration equipment [77, 78]. Although the main nuclide used in RTGs is ^{238}Pu, the decreasing availability and cost of this nuclide means that potential replacements are being investigated, including ^{90}Sr and ^{241}Am, which appear to be the best alternatives to ^{238}Pu in the near future [77–79]. Nevertheless, ^{90}Sr is already in use in unmanned lighthouses and coast guard lights [46, 77]. Another industrial application of ^{90}Sr is in thickness measurements, either by measuring the transmission of the emitted β-particles or via backscattering. Both techniques differ in terms of achievable precision and thickness [80, 81].

There are also other types of radioisotope batteries known as betavoltaic batteries (BV). Here, ^{90}Sr/^{90}Y is used as a β-source, bombarding a p-n junction to generate electron-hole pairs [82]. Recent developments in this area utilize a ^{90}Sr battery based on the dual effects of BVs and beta-photovoltaic (BPV) for increased output [83].

1.3. Novel technique for low-energy isobar suppression using RFQ ion guides

In this section, the physical principles of the suppression of low-energy isobars by ion-laser interaction in a gas-filled radio-frequency quadrupole (RFQ) ion cooler are discussed in detail. The technique of ion-laser-interaction assisted AMS enables a wide range of radionuclides to be measured by AMS with the highest sensitivity, including some previously unfeasible radionuclides.

1.3.1. Mathieu equations and ion motion

A radio-frequency quadrupole (RFQ) ion cooler is a gas-filled linear Paul trap that radially confines the injected ions. This process can be described by the Mathieu equations, and the stability criteria of the ion motion are derived from these equations [84]. In contrast to mass filtering applications of Paul traps, RFQ ion coolers for AMS purposes only act as ion guides and do not use a DC voltage superimposed to the RF voltage. Thus, the Mathieu parameter a ($a \propto U_{DC}$) vanishes, and the ion motion is dominated by the Mathieu parameter

$$q = \frac{4QU_{RF}}{mr_0^2\omega^2} \tag{1.6}$$

where Q is the charge of the particle, U_{RF} is the amplitude of the RF voltage, r is the radius of the RF rods, r_0 is the inscribed radius of the RF rods and ω is the angular RF frequency. Stable trajectories for the ions occur for values $q < 0.908$ [84–87]. For q values < 0.4 radial confinement of the ions can be approximated by a pseudopotential well

$$V_{RF}(r) = \frac{qU_{RF}}{4r_0^2}r^2 \tag{1.7}$$

with well depth $D = \frac{qU_{RF}}{4}$, where q is the corresponding Mathieu parameter [86]. Buffer gas cooling inside RFQ ion guides is a widely used technique to dampen the radial and axial motion of the trapped ions and to reduce the ion beam emittance [85, 86, 88]. By cooling down the ions using a light buffer gas, typically He, the residence time inside the RFQ ion guide increases. This is beneficial for neutralization of isobars via laser photodetachment for AMS measurements, since it is a non-resonant process with low a cross section typically on the order of Mb. To prevent the ions of interest from being neutralization by collisional detachment with the buffer gas, the collision energy has to be below the electron detachment energy. Therefore, the ions need to be decelerated before entering the buffer gas-filled RFQ section [87].

1.3.2. Laser photodetachment

Laser photodetachment is one of the two main isobar suppression channels within a gas-filled RFQ ion cooler. It describes the process of a photon (γ) detaching the weakly bound additional electron of an atomic or molecular anion (A^-), creating a neutral atom or molecule (A) and a free electron (e^-)

$$A^- + \gamma \rightarrow A + e^- \tag{1.8}$$

The energy of the photon can be derived from $E_\gamma = h\nu$, where h is Planck's constant and ν is the frequency of the interacting photon. For the photon to detach the electron, a certain energy threshold has to be exceeded. In the case of an atomic anion, this threshold corresponds to the electron affinity (EA), which is defined as the difference between the total energies of the ground state and its negative ion [89].

The EAs of atomic Zr and Sr anions do not meet the requirements for laser photodetachment. However, it has been demonstrated that the utilization of their anionic tri-fluoride molecules constitutes a suitable system for the suppression of ^{90}Zr [31] (see also Fig. 1.5). When considering molecules, the concept of EAs be-

comes more complex. The EA of a molecule R is defined as the transition energy from the ground vibrational/rotational state of the anion ($|R^-, v'' = 0, J'' = 0>$) to the ground vibrational/rotational state of the neutral ($|R, v' = 0, J' = 0>$) [89]:

$$EA(R) = \Delta E(|R, v' = 0, J' = 0> \leftarrow |R^-, v'' = 0, J'' = 0>) \tag{1.9}$$

For purposes of clarity, this is illustrated in Fig. 1.4. In addition to the EA, Fig. 1.4 shows two further transitions: the vertical detachment energy (VDE) and the vertical attachment energy (VAE). These energies provide upper and lower boundaries of the EA, respectively [89]. It should be noted that the extracted molecules of the ion beam may not all be in the vibrational/rotational ground state. Conse-

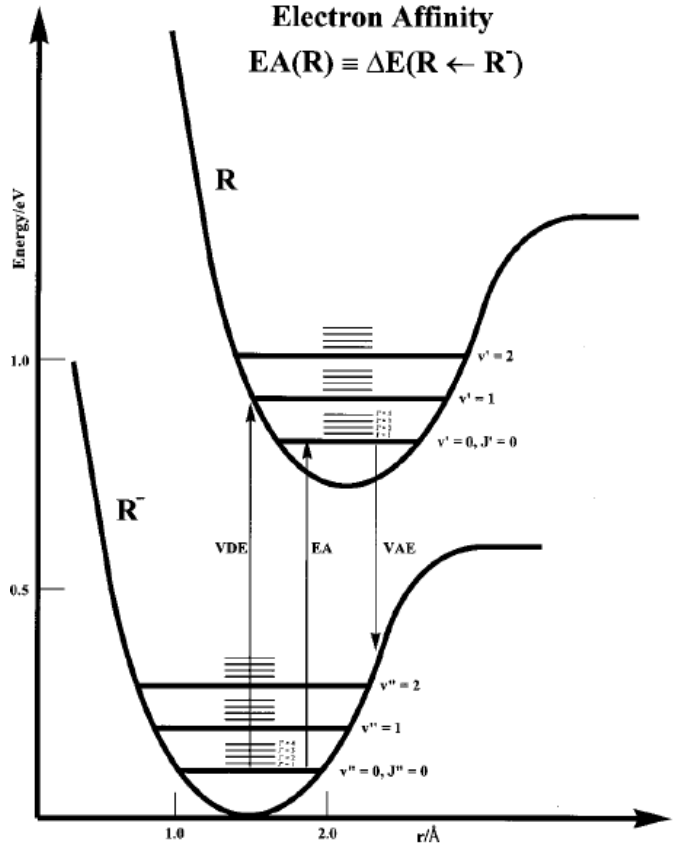

Figure 1.4.: Qualitative diagram of potential energy surfaces for an anionic molecule R^- and its neutral molecule R. Transitions shown represent the vertical detachment energy (VDE), electron affinity (EA) and the vertical attachment energy (VAE). The picture was taken from [89].

quently, the energy required to detach the electron could deviate from the EA. Therefore, a significant amount of the isotopes of interest could still be neutralized via laser photodetachment even if the photon energy is below the theoretical EA. Thus, a laser with photon energy close to the EA could result in a lower overall suppression factor compared to a laser with lower photon energy. Hence, for ion-laser-interaction assisted AMS measurements using molecular systems, it might not be advantageous to strive for the photon energy to be close as possible to the EA of the isotope of interest.

In comparison to resonant processes the cross section of laser photodetachment is very low, typically on the order of Mb. The cross section ($\sigma(E_\gamma)$) in the vicinity of the threshold energy is described by the Wigner law and in our case can be written as

$$\sigma(E_\gamma) \begin{cases} \propto (E_\gamma - EA)^{l+\frac{1}{2}} & \text{for } E_\gamma \geq EA \\ = 0 & \text{for } E_\gamma < EA \end{cases} \tag{1.10}$$

where E_γ is the energy of the photon and l is the angular momentum of the detached electron. This relation is illustrated qualitatively in Fig 1.5 for SrF_3^- and its isobar for ZrF_3^-.

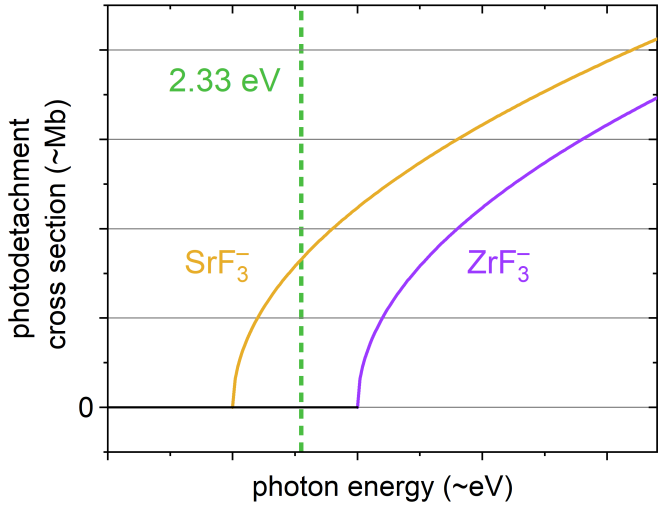

Figure 1.5.: Qualitative drawing of the photodetachment cross section against the laser energy used in AMS measurements of strontium [31]. Note that the depicted cross section assumes an outgoing s-wave electron.

Lastly, the number of suppressed anions $N_{supp.}$ can be given by

$$N_{supp.} = N_0 \cdot (1 - e^{-\sigma \Phi t}) \tag{1.11}$$

where N_0 denotes the number of ions before the interaction with the photons, σ the cross section of laser photodetachment, Φ the photon flux and t the interaction time of photons with the ion beam. Since the cross section is constant for a given photon energy, the isobar suppression depends on the photon flux and the interaction time. However, the photon flux is limited by the power of the laser, thereby rendering the interaction time the most easily adjustable parameter to increase the isobar suppression.

1.3.3. Buffer gas cooling

Reactions with the buffer are the second suppression channel, which can significantly suppress isobars via ion-gas reactions inside the ion cooler. Buffer gas cooling inside RFQ ion traps is a widely used technique, predominantly applied with positive ions, since the ionization potential is typically much larger than the detachment energies of anions [85, 88]. Therefore, when using the much more fragile anions, care must be taken to avoid neutralizing the injected anions inside the RFQ ion cooler. For collisional detachment to occur, the center-of-mass energy in collisions with the buffer gas atoms must exceed the EA of the incoming ion [28, 86]. This can be described by

$$EA < E_{ion} \cdot \frac{m_{gas}}{m_{gas} + m_{ion}} \tag{1.12}$$

where E_{ion} denotes the anion energy and $m_{gas,ion}$ the masses of the anion and the buffer gas atoms, respectively. Therefore, it is essential to electrostatically decelerate the anions to a few tens of eV before entering the buffer gas, and the buffer gas should be as light as possible to minimize the energy transfer per collision [28]. Hence, typically He is used as the buffer gas of choice.
If laser photodetachment is used as the main suppression channel of isobars, the primary function of the buffer gas is the cooling of the ions to increases their residence time inside the ion cooler. This is due to the fact that an increase in the interaction times between the laser beam and the ion beam leads to an enhanced

isobar suppression (see eq. 1.11). The use of ion-gas reactions inside a gas-filled reaction cell as the sole isobar suppression mechanism for AMS measurements is studied at the A.E. Lalonde AMS Laboratory in Ottawa. The research includes a range of different anion-gas reactions in a reaction cell to suppress isobars for AMS purposes. The research has demonstrated that this technique is capable of suppressing specific isobars by several orders of magnitude [25–27, 30, 90], comparable to suppression factors of laser photodetachment.
In the case of ^{90}Sr, it has been shown that the admixture of small amounts of O_2 ($\approx 3\%$) to the He gas is beneficial for isobar suppression of Zr. This is used in combination with laser photodetachment for AMS measurements of ^{90}Sr at VERA to maximize the suppression [31].

1.3.4. Anion Laser Isobar Separator - ALIS

The Anion Laser Isobar Separator (ALIS) is a recently constructed low-energy isobar suppression setup at CologneAMS of the University of Cologne. It was inspired by the success of the established Ion-Laser InterAction Mass Spectrometry (ILIAMS) setup at VERA of the University of Vienna [31]. Despite being based on ILIAMS, the ALIS setup features several significant design changes of the RFQ ion cooler. These changes were implemented with the aim to improve the performance of the system and to open up possibilities for future additions, e.g., for ion beam analysis inside the cooler [91]. A schematic drawing of the setup next to the 6 MV tandem accelerator in the accelerator hall is shown in Fig. 1.7.
The main components of ALIS are a 134 mulit-cathode (MC) SNICS ion source, a 90° double focusing bending magnet (BM), the gas-filled RFQ ion cooler and a 90° double focusing electrostatic analyzer (ESA). The ions are extracted from the MC-SNICS ion source with up to 30 keV, directly followed by the BM for a first mass separation before injecting the filtered ion beam into the ion cooler. Prior to entering the ion cooler, the ions are electrostatically decelerated to a few tens of eV. This is to prevent collisional detachment of the anions with the buffer gas (see section 1.3.3). Before exiting the ion cooler, the ions are reaccelerated and subsequently deflected by the ESA into the pre-existing beam line of the 6 MV tandem accelerator at CologneAMS. To ensure good focusing of the ion beam,

ion optic lenses are placed in front of the ion cooler and after the ion cooler (see Fig. 1.7). The combination of a BM and an ESA ensures that the correct m/q ratio is injected into the pre-existing beam line and consequently into the accelerator.
The design changes include some quality of life changes, such as a vacuum chamber that can be opened from the top, enabling direct access to the RFQ ion cooler. The fast and easy accessibility of the ion cooler makes potential maintenance or design modifications, e.g., repairing of electric contacts or exchanging the quadrupole with an octupole, more convenient and less time-consuming. A schematic drawing of the ion cooler is shown in Fig. 1.6.
The first major change is the use of elliptically shaped electrodes for both the electrostatic deceleration and the reacceleration process during the injection and extraction stages, respectively. Simulations of the elliptically shaped electrodes, especially for the injection part, suggest that they posses the ability to focus ion beams into the ion cooler through a 3 mm aperture [91]. This is important because it appears that an extracted SrF_3^- ion beam has a high beam emittance due to space charge effects of the tens of µA of $^{19}F^-$ ions extracted as well [92]. In order to avoid losses during the injection, it is necessary to either limit the extracted ion beam current or to improve the focusing into the ion cooler through the narrow aperture. The aim of the new injection optics was to minimize ion beam losses, even at higher ion beam currents of ≥ 300 nA of SrF_3^- out of the ion source. This would improve the measurement efficiency and subsequently decrease the required

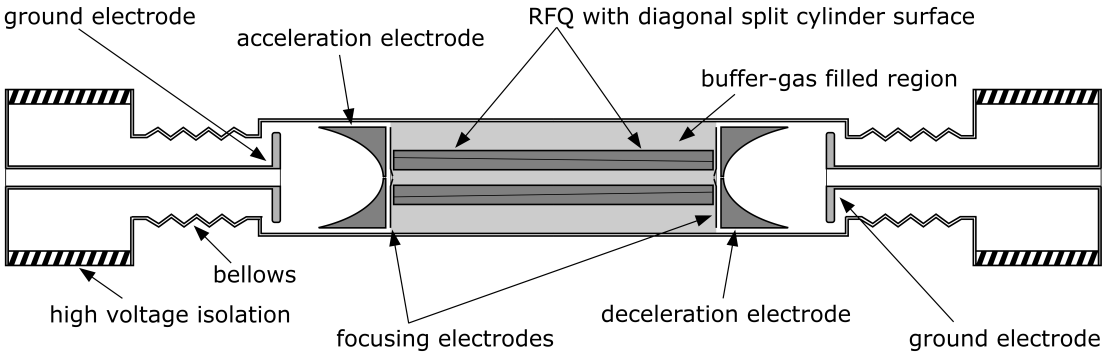

Figure 1.6.: Schematic drawing of the ALIS ion cooler. The injection/extraction of the ion cooler is symmetric and the guiding electrodes diagonal splitting is indicated as well. Note that the ion beam would come from the right side, since the deceleration electrode is there. The picture was taken from [91].

measurement time per sample. However, at present this has not yet been achieved due to unexpected collisional detachment losses during the injection into the ion cooler (see section 2.3).
The second major change is the guiding electrode structure. During the dampening of the ions caused by collisions with the buffer gas, the ions constantly lose energy. Since trapping of the anions is not desired, it is essential to ensure that injected ions exit the ion cooler within a reasonable residence time on the order of ms. Hence, a small potential longitudinal to the ions is applied, causing the ions to be slowly pulled towards the exit. This is referred to as the guiding field, produced by the guiding electrodes. To create such a field ILIAMS uses guiding rods that are inclined towards the exit between the radiofrequency (RF) rods [28]. For the ALIS ion cooler, cylindrical surfaces are split, with the cut being inclined, and then placed on top of the RF rods with an insulating layer between them. Simulations show that this geometry generates a guiding field similar to ILIAMS. However, compared to ILIAMS, the same guiding field strength can be achieved with significantly reduced applied voltages on the half shells of the guiding electrodes [91]. It has been demonstrated experimentally that this electrode structure functions as intended (see section 2.5). With the new structure, no guiding rods are positioned between the RF rods. This has the potential to enable analysis of the ion beam inside the ion cooler, e.g., with cavity ring down spectroscopy, since a laser may now be able to pass through the space between the RF rods. However, this is still far from realization and implementing such a device could pose many other problems and was not part of the thesis.

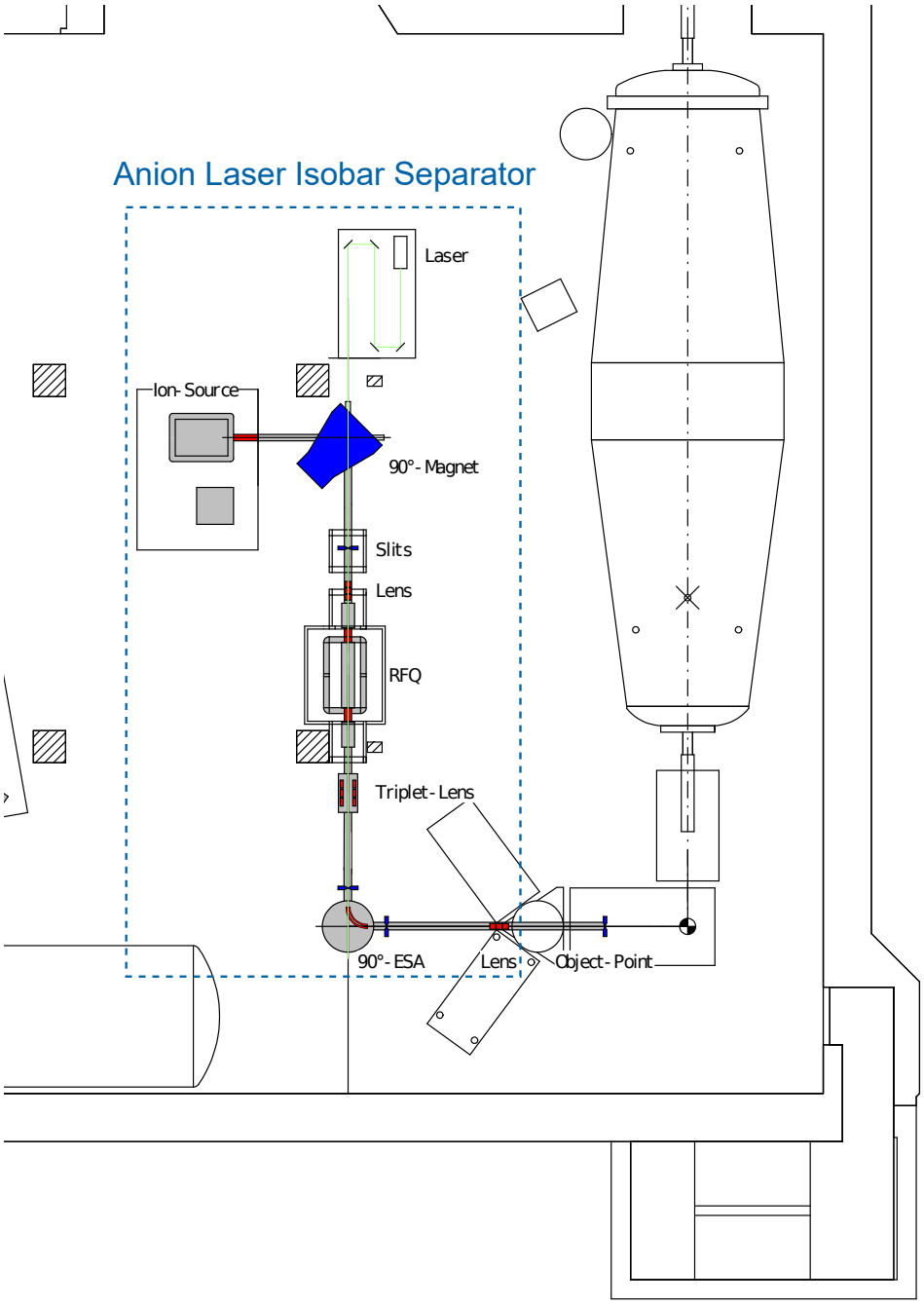

Figure 1.7.: Schematic drawing of the ALIS setup. ALIS is a low-energy isobar suppression setup for the 6 MV tandem accelerator at Cologne AMS. Note that the ALIS beam line only includes the components inside the blue box and is then connected to the already existing beam line of the 6 MV accelerator. Note that the drawing was provided by courtesy of Markus Schiffer.

2. Performance tests of the RFQ ion guide at Vienna

The RFQ ion cooler and its parts were constructed in Cologne. After construction, vacuum leak tests of the vacuum chamber and tests of the electronics were carried out before it was transported to Vienna for the performance tests. These tests were performed on a designated test bench setup. This chapter contains all relevant ion cooler performance tests that were conducted, along with the results obtained. The data presented in this chapter is based on the publication by Marchhart et al. 2025 [87].

2.1. Test bench setup

The performance tests of the Anion Laser Isobar Separator (ALIS) ion cooler were conducted on a dedicated test bench setup, which is an adapted and modernized version of the Ion Laser InterAction Setup (ILIAS) test setup of the VERA [28, 29]. A schematic drawing of the complete setup is shown in Fig. 2.1, which includes specific components that are only used for the ion residence time measurements, i.e., a micro channel plate (MCP) and a fast high voltage transistor switch (see section 2.5). Since a significant amount of components were still installed from the ILIAS setup, minimal effort was required to set up the injection part. For the purpose of improving the systems focus of the injection, a magnetic quadrupole doublet and magnetic steerers in x and y direction were added. The addition of the magnetic steerers followed initial test results, which showed ion beam losses of up to 80% between the Faraday Cup (FC) directly after the bending magnet and the FC in front of the RFQ ion cooler (see Fig 2.1). The extraction part was designed and constructed from scratch and set up according to a series of conducted ion optical simulations, described in more detail in section 2.2.

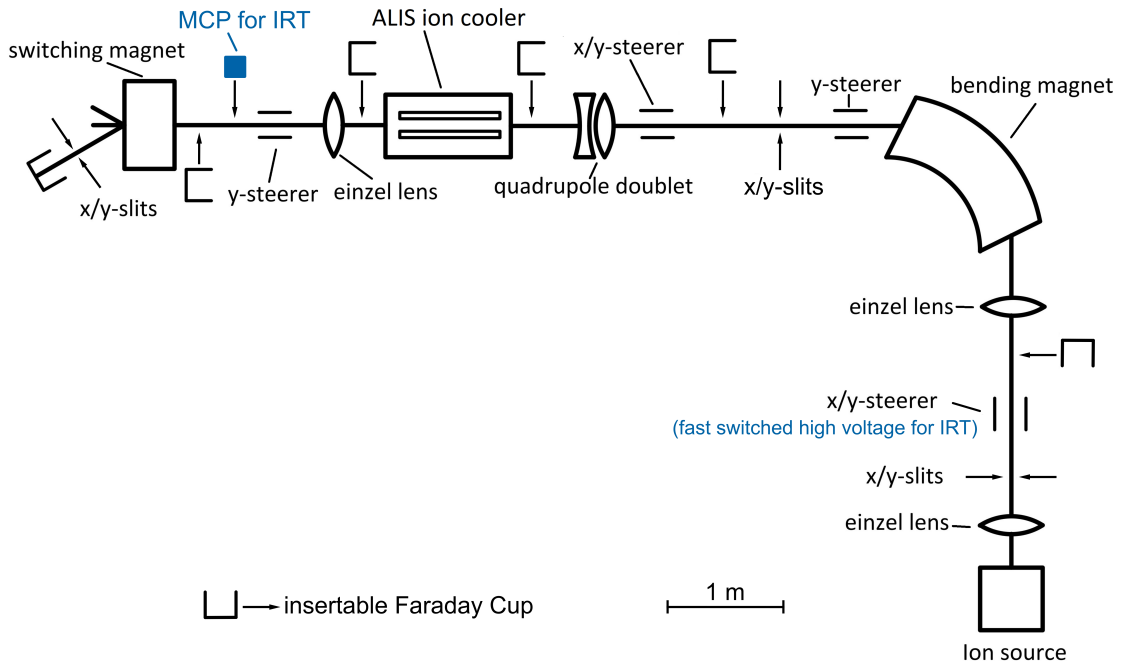

Figure 2.1.: Schematic drawing of the experimental test bench setup for the performance tests of the RFQ ion cooler. The mass filtered anions are decelerated before entering the ion cooler and reaccelerated after leaving it. Using the switching magnet after the ion cooler as another mass filter allows to to analyze the extracted ion beam for it constituents, e.g., newly formed molecules or molecular fragments due to ion-gas reactions inside the ion cooler. The schematic includes the setup for the ion residence time (IRT) measurements, labeled in blue (see section 2.5). The picture was taken from [87].

The test bench setup consists of a single SNICS II ion source from NEC, producing and extracting anions of up to 30 keV of energy. A 90° double focusing bending magnet after the ion source allows to filter and inject a selected mass into the ion cooler. The ion cooler is put on high-voltage up to a maximum of −30 kV, in order to electrostatically decelerate the ions to a few tens of eV of energy before focusing them through a 3 mm aperture into the RFQ section. The field produced by the 720 mm long RFQ rods of the linear ion trap confines the anions and a guiding field pulls the ions towards the cooler exit. Voltage differences of typically 10-20 V between the guiding electrode half-shells are sufficient for the creation of the guiding field [91]. Inside the ion cooler, a buffer gas, typically He, is used to further slow down the ions down to a few eV or even sub-eV energies [28]. Upon

exiting the ion cooler, the anion beam is reaccelerated and can be measured as an ion current in a FC. Furthermore, a 30° single focusing switcher magnet allows for mass filtering of the transmitted ion beam. This enables the analysis of the extracted ion beam for its constituents, e.g., newly formed molecules or molecular fragments due to ion-gas reactions within the ion cooler.

2.2. Ion optics

The ion optics were simulated with Limioptic II [93]. This program simulates the ion optics of an ion beam using the transfer matrices, e.g., lenses, magnets etc. [94, 95]. As a starting point for the simulations, the ion beam emittance is required. However, the emittance of the used ion source and the ion beam out of the ion cooler extraction are unknown. Hence, the ion beam emittance had to be estimated for the simulations of the injection and extraction parts of the beam line.

In an effort to avoid underestimating the emittance for the simulations, a 2σ-emittance of $17\,\pi$ mm mrad, encompassing 86.5% of the ion beam, was chosen for the injection part. This corresponds to beam parameters $x_{2\sigma} = 2$ mm, $x'_{2\sigma} = 8.5$ mrad for x and y direction. Simulations of the ion cooler extraction and existing literature suggest that the ion beam emittance and energy spread should be improved following the ion cooler extraction [21, 88], but in the simulation a conservative approach was applied. This means that the same beam emittance used for the simulation of the injection part of was also used for the simulation of the extraction part. As a result, the ion beam is initialized after the RFQ section of the ion cooler with a symmetric ion beam, and the two simulation parts are connected with a dotted line to guide the eye (see Fig 2.2). The injection and the extraction section of the ion cooler has an acceptance of $x_{3\sigma} = 2$ mm, $x'_{3\sigma} = 13.5$ mrad in x and y direction.

The envelope of the ion beam for x and y direction against the nominal path of the whole test bench setup can be seen in Fig. 2.2. The section downstream of the ion cooler has an angular acceptance of $x'_{3\sigma} = 17.6$ mrad restricted by the 40 mm aperture in front of einzel lens 3. The aperture serves as a shield, protecting the electrode from ion collisions.

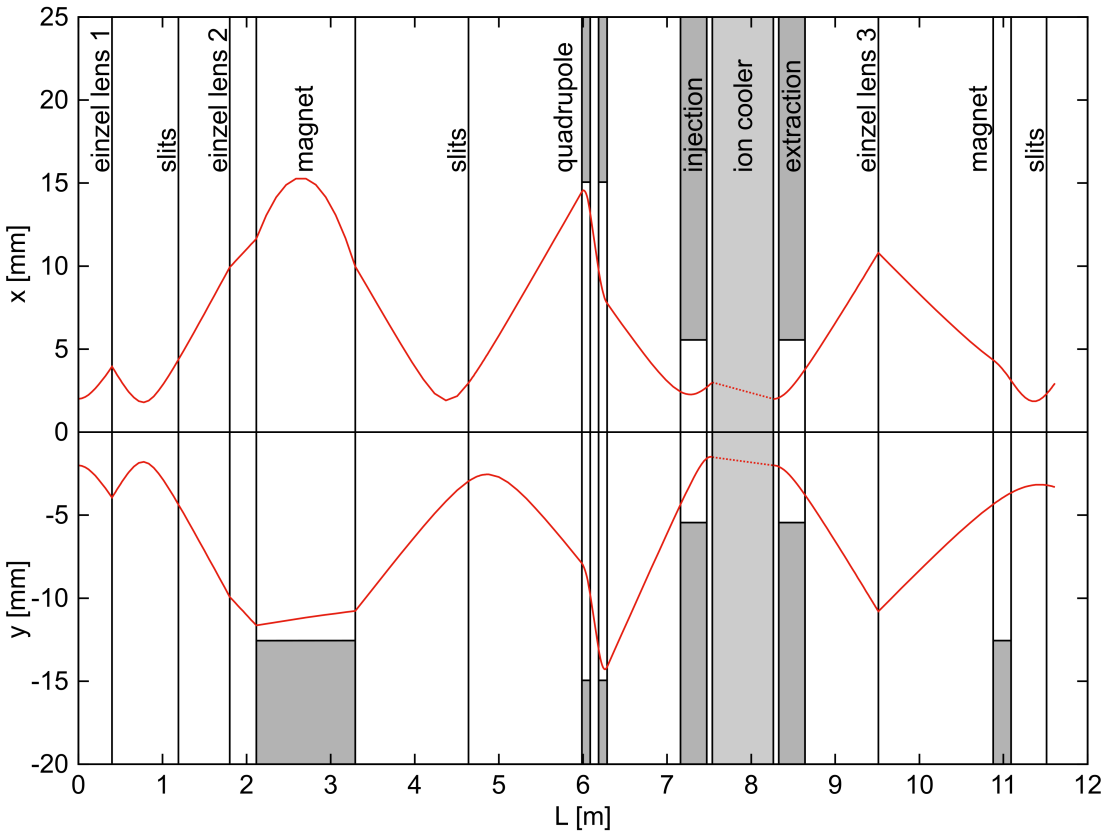

Figure 2.2.: Plot of the envelope of the ion beam in x and y direction against the nominal path at the test bench setup in Vienna. The simulations were performed with Limioptic II [93]. The injection and extraction parts are simulated separately with 2σ-emittances of $17\,\pi$ mm mrad, corresponding to 86.5% of the beam. The beam parameters are $x_{2\sigma} = 2\,\text{mm}$ and $x'_{2\sigma} = 8.5\,\text{mrad}$ for x and y direction. Both simulations are connected with a dotted line to guide the eye. The picture was taken from [87].

2.3. Ion cooler transmission

A crucial factor for high AMS measurement efficiency using an ion cooler is a high cooler transmission, defined as the ratio between the injected ion current and the ion current that can be extracted and further transported. In the case of intense ion beams, i.e., electrically measurable currents, the transmission can be determined with FCs before and after the ion cooler.

Within the ion cooler, there is a possibility for molecules to undergo ion-gas reactions. Hence, the measured ion current directly after the cooler extraction might

contain a significant amount of newly formed molecules or fragments of the injected molecules. Therefore, the setup contains the 30° switcher magnet, followed by a FC to measure the correct transmission (see Fig. 2.1). The transmission tests were performed with $^{27}AlO^-$ (43 amu) and $^{63}Cu^-$ beams, ranging from a few nA up to hundreds of nA, extracted with 23.5 keV energy. The extracted ion beam currents were adjusted by variation of the Cs oven temperature and the ionizer surface temperature of the ion source. A number of crucial parameters during operation that influence the achievable transmission include the buffer gas pressure, the Mathieu parameter q, and the injected ion current [28]. Consequently, the dependence of the cooler transmission on these parameters was investigated. Nonetheless, the dependency of the injected ion current could not be investigated due to injection problems that became apparent during the performance tests (see section 2.4).

The results of the ion cooler transmission with respect to different He buffer gas pressures are shown in Fig. 2.3. The measurements revealed that the transmission remains relatively constant at very minimal buffer gas pressures up to roughly 1.2 Pa, displaying a plateau-like structure, and starts to decrease significantly at higher pressures (see Fig. 2.3). For both ion beams, i.e., $^{27}AlO^-$ and $^{63}Cu^-$, transmissions of up to 30% through the ion cooler were achieved at buffer gas pressures around 1.0 Pa. The buffer gas pressure measurements were taken with an ion gauge in the center of the vacuum chamber of the ion cooler, opposite the gas inlet. It should be noted that this represents a maximum value that may decrease towards the entrance/exit of the ion cooler. A transmission of 30% is at least a factor of two smaller than what the ILIAMS setup at VERA has shown to be achievable [28, 55], and thus hints at significant losses between the injection and extraction of the ion beam. Subsequent investigations revealed that a portion of the ion beam losses can be attributed to losses during the injection into the ion cooler. A more thorough description of these investigations and the obtained results can be found in section 2.4.

Additionally, the transmission dependence with respect to the Mathieu parameter q was measured and is shown in Fig. 2.4 (a). The adjustment of parameter q was achieved by varying the amplitude of the radiofrequency voltage while maintaining the rest of the parameters constant (see eq. 1.6, $r_0 = 5.232$ mm). As buffer gas,

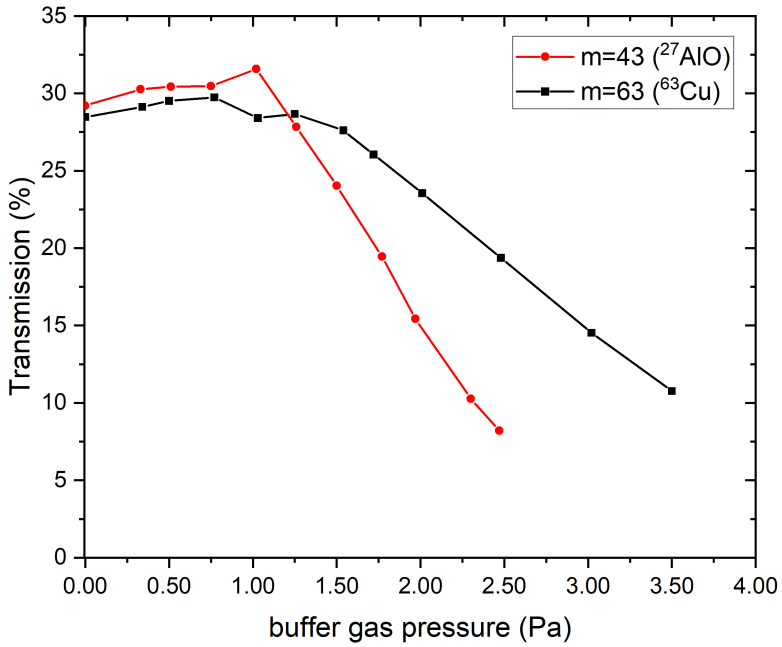

Figure 2.3.: Transmission through the ion cooler as a function of the buffer gas pressure inside the ion cooler, when injecting $^{27}AlO^-$ (red) and $^{63}Cu^-$ (black) ion beams. For the measurements, pure He was used as a buffer gas. At low buffer gas pressures between 0 Pa and 1.2 Pa, a plateau-like structure is observable, where the transmission remains relatively constant. For buffer gas pressures that exceed 1.2 Pa, the transmission starts decreasing significantly. The picture is taken from [87]

He was used at 1.0 Pa, and the highest transmissions were achieved for q values between 0.2 and 0.5. According to the Mathieu equations, the ion motion inside the ion cooler is not stable for $q \geq 0.908$ [85]. However, as illustrated in Fig. 2.4 (b), at q values above 0.908, a small amount of a few hundred pA were still measured in the FC. The ion motion according to the Mathieu equations is only valid for singular particles in vacuum. However, during the operation of the ion cooler for AMS purposes, intense ion beams are injected into a buffer gas-filled RFQ section. Under these circumstances, it appears that there are scattering events, or trajectories, stable long enough for some anions to exit the ion cooler with q values slightly higher than 0.908.

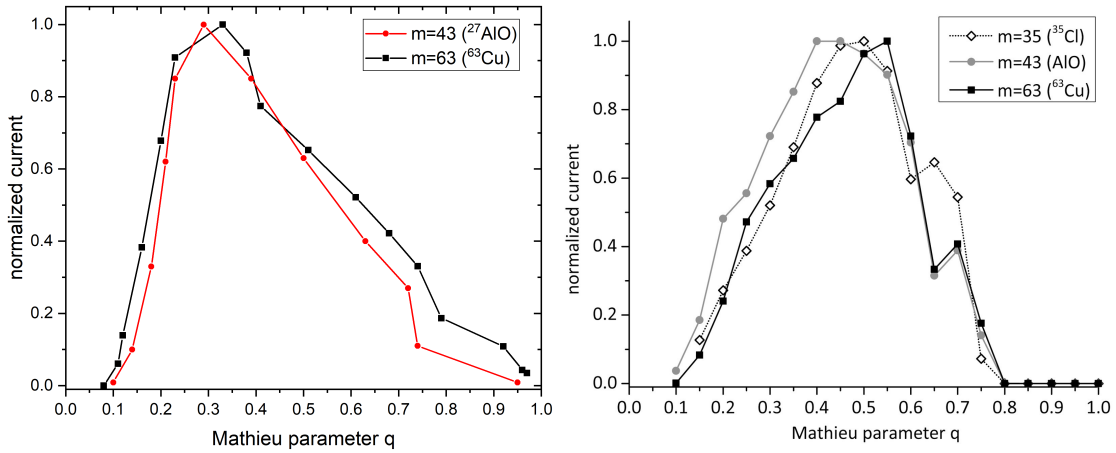

(a) ALIS ion cooler [87]

(b) ILIAMS ion cooler [28]

Figure 2.4.: Comparison of the normalized transmission through the ion cooler as a function of the Mathieu parameter q for the new ALIS ion cooler and the established ILIAMS ion cooler. (a) Normalized transmission of the ALIS ion cooler at a pressure of 1.0 Pa of He as buffer gas. $^{27}AlO^-$ (red) was measured at a RF frequency of 2.4 MHz with an injection current of 150 nA. $^{63}Cu^-$ (black) was measured at a RF frequency of 2.1 MHz with an injection current of 450 nA. The highest transmissions were observed at q values between 0.2 and 0.5. (b) Normalized transmission of the ILIAMS ion cooler at a pressure of 20 Pa (0.2 mbar) of He as buffer gas. Here, the RF frequency was subject to variation. The injected currents were 35 nA for $^{35}Cl^-$, 150 nA for $^{63}Cu^-$ and 360 nA for $^{27}AlO^-$. The highest transmissions were observed at q values between 0.4 and 0.5 [28]. The pictures were taken from [28, 87], respectively.

2.4. Injection into the RFQ ion cooler

To achieve high transmission through the ion cooler, it is essential to efficiently focus the decelerated anions efficiently and without significant beam losses into the ion cooler through the 3 mm apertures of the deceleration and focusing electrodes. Simulations of the injection into the RFQ section with Simion 8.1 [96] yielded promising results of 94% for an ion beam with beam parameters of $x_{1\sigma} = 1.59$ mm, $x'_{1\sigma} = 2.44$ mrad starting 115 mm in front of the ion cooler [91]. However, the results of the conducted performance tests demonstrated that the maximum achievable transmission through the ion cooler was around 30%. This is significantly lower than expected, as described in section 2.3. Thus, an initial investigation was conducted to determine whether losses already occurred during the deceleration or injection of the ion beam into the RFQ.

As illustrated in Fig. 2.5, two distinct measurement setups were employed: Setup A using only the elliptically shaped deceleration electrode and Setup B using both, the decelerating as well as the focusing electrode. For the measurements, the RFQ part had to be removed so that a custom-made FC with 1 cm diameter and two permanent magnets for secondary electron suppression could be used directly after the electrodes. The cup itself was mounted in a cylindrical non-conductive holder that was placed on the linear rail, where typically the RFQ resides. To ensure an undisturbed buffer gas flow, the cylindrical holder was perforated several times in the axial direction. All measurements were conducted using an $^{27}AlO^-$ ($m = 43$ amu) ion beam in the range of 10 nA to 60 nA. The injection into the ion cooler was defined as the ratio of the measured ion current in the custom-made FC positioned directly after the injection electrodes and the measured current in the FC in front of the ion cooler. The results are summarized in Tab. 2.1. In the absence of buffer gas, almost 100% of the ion beam can be focused through the injection lenses into the custom-made FC. However, when buffer gas is present, the injection into the ion cooler drastically decreases. This shows that under standard operating conditions, i.e., with buffer gas present, a majority of transmission losses through the ion cooler occur at the injection part. Using buffer gas and both injection electrodes (setup B), no measurable ion current is observed on the

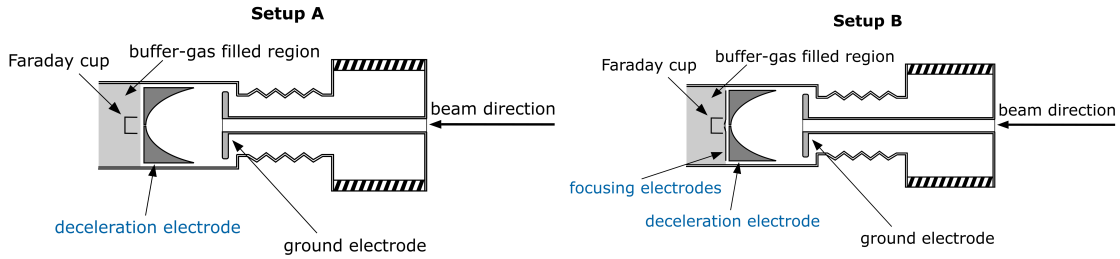

Figure 2.5.: Schematic drawings of the injection part of the RFQ ion cooler for the two setups used to investigate potential losses during the injection process. For the injection measurements, the RFQ rods were removed, leaving only the two highlighted injection electrodes and a custom-made FC right behind the electrodes to measure the ion current. The measurements were performed using two setups: (a) only the deceleration electrode and (b) the combination of focusing and deceleration electrodes. Note that these pictures are adapted versions from [91] and were taken from [87].

focusing electrode, indicating that the beam losses already occur at the decelerating electrode. This is most likely due to the interaction of the anions with the buffer gas that leaks through the aperture. Hence, a significant difference between setup A and setup B under gas-filled conditions is unlikely, even though no measurement was performed for setup A specifically. If the injected ions have not been sufficiently decelerated prior to their collision with the buffer gas, the ions can be neutralized via collisional detachment or might undergo some chemical reactions, resulting in transmission losses. A pressure increase in the deceleration region by approximately one order of magnitude from $2.3 \cdot 10^{-3}$ Pa up to $3.1 \cdot 10^{-2}$ Pa when buffer gas is used strongly hints at that possibility. It has to be noted that no differential pumping was not employed in any of these measurements because the vacuum deteriorated further when the differential pumping valve was opened. This can be explained by the ultimate total pressure of $3.0 \cdot 10^{-2}$ Pa for the dry compressing vacuum pump ECODRY 65 plus used for differential pumping. For this reason, improving the vacuum in the deceleration region of the injection will be the primary measure to improve the transmission.
The transmission measurements conducted without the presence of buffer gas did not improve the overall transmission through the ion cooler (see Fig.,2.3 (a)). However, it can be assumed that around 94% of the ion beam has been injected into the RFQ section, indicating losses in the RFQ section or extraction section. As buffer gas is used under standard operating conditions, it is of no further interest to explore the reasons for these losses or potential remedies.

Table 2.1.: Measured injection into the ion cooler for two different setups, with and without the use of buffer gas in the RFQ section. Setup A only uses the deceleration electrode and Setup B uses both injection electrodes (see Fig. 2.5). For these measurements, the buffer gas pressure was set to 1.2 Pa. In the absence of buffer gas, the majority of the ion beam can be focused through the injection lenses into the RFQ section. Conversely, with buffer gas present, the injection into the ion cooler drastically decreases. Note that no measurement was performed for setup A with buffer gas present. The table values were taken from [87].

setup	**no buffer gas**	**with buffer gas**
A	100%	not measured
B	94%	30% - 50%

2.5. Ion residence time

The primary objective of the ion cooler is to maximize interaction time between the laser beam and the ion beam. For the ILIAMS ion cooler, it was observed that the residence time of ions depends, among other parameters, on the injected ion current. The residence time can range from hundreds of µs (when injecting 460 nA) up into the ms range (when injecting ≤ 3.2 nA) [28]. Since the ALIS guiding electrode structure differs significantly from the inclined guiding electrode rods of the ILIAMS ion cooler, the functionality of the hybrid guiding electrode structure of the ALIS ion cooler, with diagonally split cylindrical guiding electrodes on top of RF rods [91], was tested by evaluating the ion residence time (IRT) for different guiding electrode voltages.
The IRTs were measured via leak out measurements using a $^{63}Cu^-$ beam with 23.5 keV of energy, under different guiding field strengths and buffer gas pressures. The investigated leak out of the ions from the ion cooler by the fast stopping of a continuously injected ion beam resulted in a micro channel plate (MCP) signal that changes from a plateau down to zero (see Fig. 2.6 (c)). The slope of the current signal contains the IRT information and the residence time distribution can be obtained by differentiating the current signal [28]. Due to the presence of a humming noise, it was not feasible to collect multiple data sets for signal smoothing by ensemble averaging. Hence, the MCP current signals were fitted with a sigmoidal function, and the fit was subsequently differentiated. Therefore, the residence time distributions look much smoother and on average appear to be slightly more asymmetric due to a more pronounced tails towards high residence times compared to Martschini et al. 2017 [28]. A partial explanation for these longer tails is that the sigmoidal fitting function does converge slower down to zero than the measurement signal. However, it might also be an unexpected feature of this ion cooler design. The experimental results are displayed in Fig. 2.6 (a) and (b). The origin of the residence time in Fig. 2.6 is defined as the time when the onset of the steerer plate is triggered. The residence time plotted in these figures is the time-of-flight of the ions from the steerer plate until the detection in the MCP. This includes 26 µs time-of-flight of the ions outside of the ion cooler.

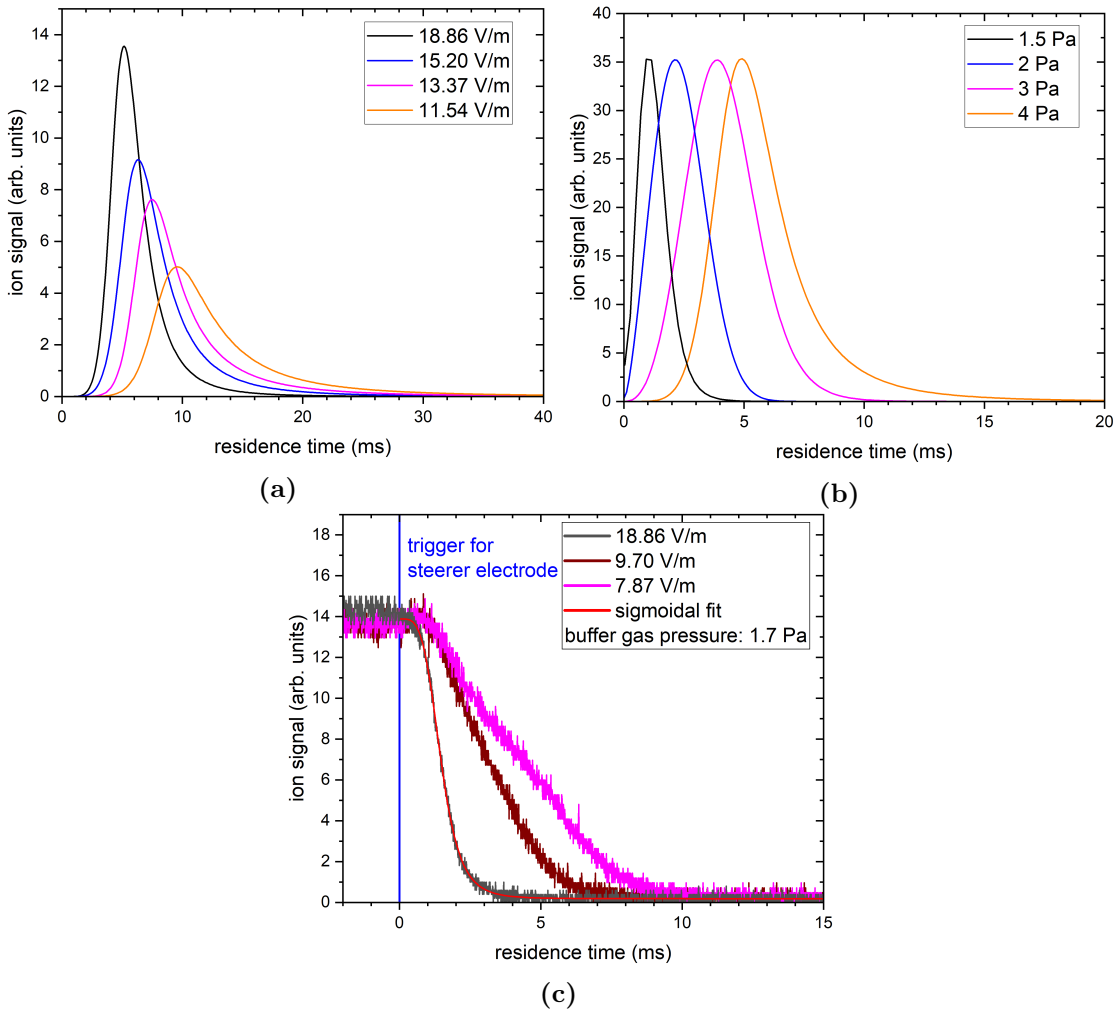

Figure 2.6.: IRT distributions and an exemplary ion signal of the MCP detector for a $^{63}Cu^-$ ion beam when injecting approximately 250 nA. (a) Dependence of the IRT for different guiding field strength at 4 Pa He buffer gas. The guiding field strength has a visible effect on the IRT distribution. As the magnitude of the field strength increases, the ions are pulled towards the cooler exit at a faster rate, leading to shorter IRTs. (b) Dependence of the normalized IRT distribution at different buffer gas pressures with a constant guiding field strength of 18.86 V/m. The increase of the IRT with rising buffer gas pressure is attributed to an increased number of collisions with the buffer gas. (c) Dependence of the falling ion signal of the MCP detector prior to fitting and differentiating for different guiding field strengths at 1.7 Pa of He buffer gas. To enhacne the visualization of the shift of the IRTs, the falling ion signals are normalized to the highest measured signal at a guiding field strength of 18.86 V/m. A sigmoidal fit, which is differentiated to obtain the IRT distribution, is also shown for the 18.86 V/m MCP signal (black). Note that the time-of-flight outside of the ion cooler of around 26 µs is included in all plots. The pictures (a) and (b) were taken from [87].

The setup utilized the same fast high voltage transistor switch (HTS 51 from Behlke Power Electronics) used in Martschini et al. 2017 [28] to apply a voltage of 200 V to one of the y steerer plate pairs in front of the 90° bending magnet. With this configuration, the ion beam was injected continuously as long as no voltage was applied to the steerer plate, and the injection was abruptly stopped when a voltage was applied to the y steerer plate by deflecting the ion beam (see Fig. 2.1). A rectangular signal from a function generator (Tektronix AWG2021) was used to trigger the high voltage transistor. A MCP operated at 1700 V was used as a detector for the detection of the transmitted ion beam because the direct measurement of the time structure signal in the pA range would not have been possible with a FC. This resulted in anode currents of a few hundred nA, which was a reasonable current to resolve the time structure signal. Further details on the measurement setup can be found in [87].
The guiding field strength was calculated using the formula $E = \frac{0.65 \cdot \Delta U_{DC}}{l}$ [91], and its effect on the residence time was visible. The magnitude of the field strength directly correlates with the rate at which the ions are pulled towards the cooler exit, resulting in shorter residence times. This observation indicates that the new guiding electrode structure and the produced guiding field work as intended, as illustrated in Fig. 2.6 (a). Furthermore, the impact of the buffer gas pressure on the residence time is consistent with the expectation that higher pressure will result in longer residence times due to an increased number of collisions with the buffer gas. This effect is depicted in Fig. 2.6 (b), where the measured ion signals are normalized to the highest measured signal to better visualize the shift in the residence time.
A more thorough examination of the residence times allows for the extraction of certain parameters, e.g., the most probable residence time, the median and the FWHM of the IRT distribution. For this, only the buffer gas pressure or the guiding field strength was varied, while all other ion cooler parameters were kept constant. The results are summarized in Tab. 2.2. The most probable residence time and the median residence time do differ considerably due to the broadening of the IRT distribution, which is reflected in a pronounced long tail towards higher IRTs and a less steep increase in the beginning (see Fig. 2.6). However, the broadening of the distribution is less distinct in the case of varying buffer gas pressures. As expected,

the full width at half maximum (FWHM) of the IRT distributions follows the same trend (see Tab. 2.2). For the sake of reference, the shortest IRT required by an ion with thermal kinetic energy of 12.6 meV to pass through the 720 mm long ion cooler by axial directional flight is 3.66 ms.
While the measurement results appear to be plausible and are within the expected range of IRTs, a direct comparison with results from the ILIAMS setup [28] is difficult due to the unknown injected ion current. This is due to the fact that, during the measurements, injection losses must assumed with the use of buffer gas, as previously discussed in section 2.4.

Table 2.2.: Results of the data evaluation of the residence time distributions when all cooler parameters are kept constant and only either the buffer gas pressure or the guiding field strength is varied. The table provides the most probable IRT, the median of the IRT, and the FWHM of the IRT. Note that the guiding field strength was held constant at 18.86 V/m when changing the gas pressure. The buffer gas pressure was held constant at 4 Pa when changing the guiding field strength. The values of the table were taken from [87].

field strength (V/m)	**most probable (ms)**	**median (ms)**	**FWHM (ms)**
11.54	9.4	15.0	6.1
13.37	7.3	12.1	4.6
15.20	6.1	9.3	4.3
18.86	5.0	7.0	3.2
pressure (Pa)			
1.5	1.1	2.0	1.4
2.0	2.1	2.9	2.6
3.0	4.0	4.6	3.3
4.0	5.0	7.0	3.2

3. Development and validation of a new sample preparation protocol for AMS measurements of ^{90}Sr in concrete and soil at VERA

This chapter presents an overview of the development, validation, and use of a new protocol for the chemical sample preparation of ^{90}Sr in soil and concrete samples. The sample preparation for all samples mentioned in this work was carried out in the laboratories in Vienna. It is a largely modified version of the protocol by Honda et al. 2022 [97], which will be referred to as the Honda protocol for the remainder of this work. All AMS measurements in this chapter were performed using the established Ion-Laser InterAction Mass Spectrometry (ILIAMS) setup at the Vienna Environmental Research Accelerator (VERA). Major parts of this section are based on data that is planned to be published later this year. A complete list of all samples that were processed for this work can be found in Appendix C. To avoid confusion, all mentioned dates of this chapter are in the format of DD.MM.YYYY.

3.1. AMS measurement routine at VERA

The AMS measurements for all samples that were processed at Vienna (see Appendix C.1) were carried out at VERA using the ILIAMS setup. A schematic drawing of the VERA facility for ^{90}Sr measurements is shown in Fig. 3.1.
Anions are produced using a MC-SNICS type ion source. The ILIAMS ion source allows to mount sample wheels with up to 40 samples. The anions are extracted

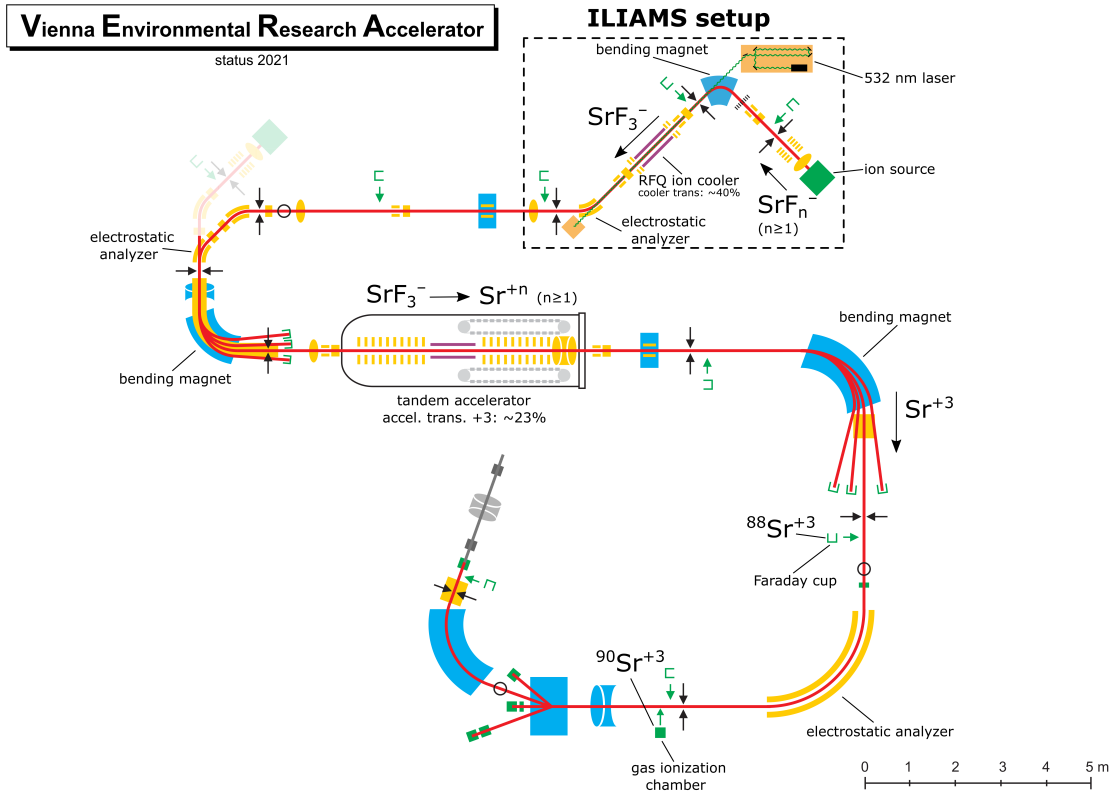

Figure 3.1.: Schematic drawing of VERA illustrating the ILIAMS setup, the most important components of the facility and the path of the Sr from the ion source until detection. The ion cooler transmission for SrF_3^- is around 40%, and the accelerator transmission for the 3+ charge state is around 23% at a terminal voltage of approximately 2.9 MV.

out of the ion source with 30 keV of energy. The extracted anions are initially mass filtered for SrF_3^- using a 90° bending magnet and subsequently injected into a gas-filled radiofrequency quadrupole (RFQ) ion cooler. In the case of Sr, the ion cooler is filled with a He:O_2 (30:1) mixture that suppresses the isobaric anion $^{90}ZrF_3^-$ by ion-gas reactions [25, 31, 32]. In addition, the ion beam is collinearly overlapped with a green laser (532 nm, 10 W) to detach the weakly bound electron of the isobar $^{90}ZrF_3^-$ via laser photodetachment, while leaving the isotope of interest, $^{90}SrF_3^-$, unaffected. The combination of the two methods effectively suppresses the isobar $^{90}ZrF_3^-$ vs. $^{90}SrF_3^-$ by $> 10^7$ [31]. This outcome is attributable to the energy of the photons of the green laser, which have 2.33 eV of energy. This photon energy

is above the energy required to neutralize $^{90}ZrF_3^-$, yet it is lower than the energy required to neutralize $^{90}SrF_3^-$. Therefore, the $^{90}ZrF_3^-$ molecules are suppressed, while the $^{90}SrF_3^-$ molecules remain unaffected by the laser. After the ion beam is extracted from the ion cooler, the ions pass the low-energy mass spectrometer and are injected into a tandem accelerator operated at around 2.9 MV. In the accelerator, the injected molecules undergo charge exchange in the stripper canal, using He as the stripper gas, and molecular break up takes place [11, 12, 97]. Upon exiting the accelerator, the ion beam is filtered for the 3+ charge state, and the intense beam of the stable $^{88}Sr^{3+}$ is measured in a FC. Meanwhile, the radionuclide $^{90}Sr^{3+}$ is measured in a split-anode gas ionization chamber. The extraction of SrF_3^- from the ion source, in combination with the suppression of ZrF_3^- in the ion cooler and the separation of $^{90}Sr^{3+}$ and $^{90}Zr^{3+}$ in the gas ionization chamber due to different energy loss, results in a total suppression of ^{90}Zr of $> 10^{12}$ [97]. The overall measurement efficiency for ^{90} Sr at VERA is 0.4‰ [31, 97].
During AMS measurements, samples of unknown ^{90}Sr concentration are always measured in conjunction with blank and standard material. Blanks are samples to check the machine background (machine blank) and unwanted contamination during sample preparation (processing blank). Standards consist of material with known ^{90}Sr/Sr ratios and are used for normalization of the measurement. The used standards were on the order of 10^{-11} (Sr-11J) and 10^{-12} (Sr-12J) [98] from dilution of an LSC activity standard provided by the Japanese Atomic Energy Agency (JAEA). The samples, standards, and blanks are measured sequentially. Subsequently, the samples are normalized to the standards and blank corrected. Afterwards, the measured ^{90}Sr/Sr ratio in conjunction with the processed sample size and the added Sr carrier, is used to calculate the specific activity of the samples. The calculated activities are eventually compared to literature values or results from other techniques. All samples are measured in Cu cathodes closed with Cu pins.

3.2. Analyzed samples

All processed and analyzed samples used for the development and validation of the newly developed sample preparation protocol were soil and concrete samples.

The analyzed soil samples were two reference materials from the International Atomic Energy Agency (IAEA): IAEA-375 & IAEA-447. Although the specific activities of ^{90}Sr have been determined for these two materials, neither of the IAEA materials has a certified value for ^{90}Sr. Instead, only have a recommended and an information value, respectively [99, 100]. In Tab. 3.1 the specific activities for ^{90}Sr of the two IAEA materials are listed.

Table 3.1.: List of the specific activities for ^{90}Sr and the reference dates of the two IAEA reference materials used for the development and validation of a new and fast sample preparation protocol. Note that for the IAEA-375 material only the 95% confidence interval and not a 1σ uncertainty is published [99].

sample name	**specific activity (Bq/kg)**	**reference date**
IAEA-375	108, 101 - 114 (95% confidence interval)	31.12.1991
IAEA-447	5.0 ± 0.3	15.11.2009

The concrete samples are from the AVR, a nuclear high-temperature gas reactor in the decommissioning phase, which got partially contaminated with ^{3}H and ^{90}Sr among other radionuclides, as described in more detail in section 1.2.4. More precisely, two drill cores were taken at different locations (330° & 340°) from the +5 m layer of the reactor that was contaminated with ^{90}Sr. Both drill cores were divided into sections of 2 cm thickness each, starting from the reactor inside to the outside. Prior to the acquisition of the samples, the samples have been analyzed via LSC to determine the specific activity for ^{90}Sr. One sample has been found to have a relatively high activity level of (90 ± 13) mBq/g (reference date: 01.01.2022), while the remaining samples have activity levels below or close to the LSC detection limit (< 5 mBq). Since the majority of the samples are below the LSC detection limit, only upper limits of the activities are known [101]. Pictures of the bottles containing the analyzed samples are shown in Fig. 3.2.

Furthermore, blank (machine and processing blanks) and standard sample were also measured in the AMS measurements. The machine blank material is commercially available SrF_2 (Alfa Aesar, 99.99%, puratronic, Lot No.: 23050). For each batch of samples, one processing blank was also processed. The processing blank consists of only stable Sr carrier (LGC standard, Product No.: VHG-TSRN-500, Lot No.: 1123421-12, (10 000±50) µg Sr/ml in 5% HNO_3) that undergoes the same chemical treatment as the samples of unknown concentrations of the same

batch. It should contain no ^{90}Sr. An elevated ^{90}Sr signal in the processing blank, but not in the machine blank, might indicate a contamination during the sample preparation andt can be assumed that all samples of the same batch have been contaminated by the same amount. The standards Sr-11J and Sr-12J were used for normalization. All samples are mixed with commercially available PbF_2 (Alfa Aesar, 99.997%, puratronic, Lot No.: 10190514) 1:8 (SrF_2:PbF_2) by weight to optimize the ionization efficiency of SrF_3^- [31], and finally pressed in Cu cathodes sealed with Cu pins.

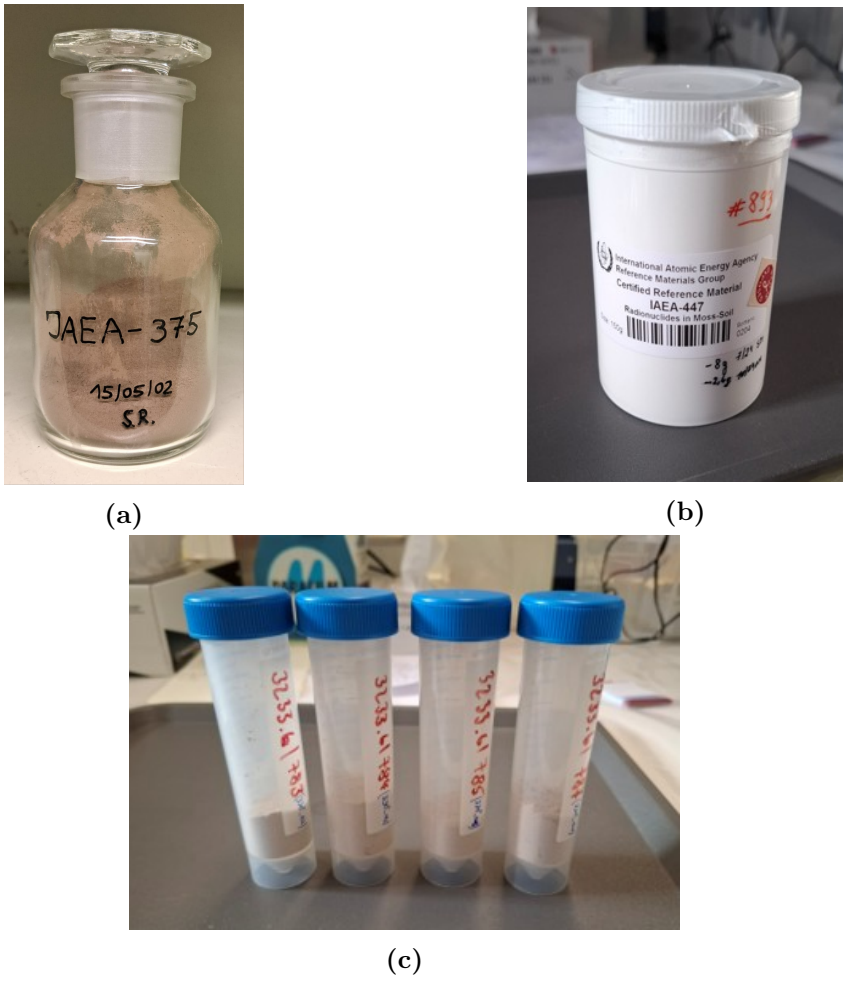

(a) **(b)**

(c)

Figure 3.2.: Pictures of the two IAEA-reference materials containers (a) IAEA-375 [99], (b) IAEA-447 [100] and (c) centrifuge tubes filled with concrete samples from the AVR reactor in Jülich. Note that more than the four shown concrete samples have been processed and analyzed.

3.3. Aim of the AMS sample preparation

The goal of every sample preparation is to produce good targets. A good AMS target is characterized by the fact that it provides a stable and high ion current output that remains steady over several hours. In addition to producing high-performing AMS targets, reducing the cost and time of the sample preparation is crucial for projects where large numbers of samples need to be analyzed, e.g., decommissioning of nuclear facilities. Overall, it is always beneficial to strive for the development of a cost-efficient and rapid method with short analyzing time that can also handle a high sample throughput.

To check the chemical recovery of Sr during the sample preparation, the chemical yield is determined after the last drying step via gravimetric analysis (see eq. 3.1). Gravimetric chemical yields are based on the Sr carrier added and the amount of intrinsic Sr, which can be measured by inductively-coupled plasma (ICP) techniques, e.g., optical emission spectroscopy (ICP-OES), ICP mass spectrometry (ICP-MS), or X-ray fluorescence (XRF). In our case, the intrinsic Sr content for the IAEA-447 reference material was measured via ICP-OES at the University of Natural Resources and Life Sciences (BOKU) and a published value exists for this matrix as well, which was measured by ICP-MS $(0.94 \pm 0.03) \cdot 10^{-4}\,\mathrm{g\,Sr/g\,dry}$ weight [97]. The intrinsic Sr of the analyzed concrete samples was measured by XRF and provided by the Jülicher Entsorgungsgesellschaft für Nuklearanlagen (JEN) mbH together with the samples. One disadvantage of the gravimetric determination of the chemical yield is a possible overestimation, originating from unwanted contaminants, e.g., CaF_2. The gravimetric chemical yield is calculated by the formula

$$\text{chemical yield} = \frac{\mathrm{m_{sample}}}{\mathrm{m_{expected}}} \tag{3.1}$$

where $\mathrm{m_{sample}}$ denotes the dry mass of the sample after the sample preparation and $\mathrm{m_{expected}}$ denotes the expected mass originating from the added Sr carrier and the intrinsic Sr measured by other techniques, e.g., ICP-MS, ICP-OES.

Another method to validate the success of the Sr recovery is to compare the $^{88}Sr^{3+}$ ion current, measured after the analyzing magnet, of each individual sample with

the average $^{88}Sr^{3+}$ current of the standards used in the same AMS measurement, the ratio of these two ion currents is referred as quality factor [102] and can be calculated as follows

$$\text{quality factor} = \frac{\bar{I}_{\text{sample}}}{\bar{I}_{\text{standard}}} \tag{3.2}$$

here $\bar{I}_{\text{sample}}$ denotes the average ion beam current of $^{88}Sr^{3+}$ of the sample, measured in a FC on the high-energy side after the accelerator, and $\bar{I}_{\text{standard}}$ denotes the average ion beam current of $^{88}Sr^{3+}$ of the used AMS standards.

One advantage of the quality factor is that it accounts for variable performance, i.e., overall efficiency and fractionation, of the AMS system and especially the ion source [102]. Samples with high contamination (chemical yield $>100\%$) tend to yield low quality factors. This can be attributed to the dilution of the Sr present in the sample by unwanted contaminants, resulting in low $^{88}SrF_3^-$ ion currents over the whole measurement time. For samples in which the majority of the Sr is lost during the processing (low chemical yield), the quality factor is also low. This typically results in sample material that only produces a reasonable $^{88}SrF_3^-$ current for a short time, which may not generate trustworthy data. In the case of ^{90}Sr, there is in most cases ample sample material available, so that the quality factor is not significantly affected by the measurement time, as the AMS measurement is finished before the ion current drops significantly. However, in instances where the availability of material is limited, it might be necessary to allocate additional measurement time at lower $^{88}SrF_3^-$ output to ensure sufficient precision, albeit at the expense of a reduced quality factor.

In summary, both methods, i.e., gravimetric chemical yield and quality factor, have advantages and disadvantages. Hence, a combination of both methods leads to a more accurate picture, because high chemical yields and quality factors correlate with high Sr recovery. Plotting the quality factor against the chemical yield is a useful method to visualize the success of the sample preparation [102].

3.4. Investigated modifications for potential improvements of the sample preparation

The sample preparation is a largely modified version of the Honda protocol for soil samples [97]. A few implemented changes are based on the work of Landstetter and Wallner (2006) who have extracted ^{90}Sr from deer bones for LSC measurements [103]. The processed and analyzed samples are described in section 3.2. The modifications to the Honda protocol were investigated not only with the objective to optimize the time and cost of the sample preparation but also to improve efficiency and laboratory safety. For the purpose of these investigations, the IAEA-447 (moss-soil) reference material was processed several times. The name of the samples indicates the applied treatment. For instance, the molar concentration of the used acids is indicated by either "15 M" or "8 M", while ashed samples have "_ash" added to the sample name.

1. **Ashing of samples:** It was investigated whether the ashing of the sample prior to the acid leaching does affect the chemical yield or the sample performance during AMS measurements. Four 1 g samples were processed for each individual approach, i.e., 15 M, 15 M_ash, 8 M, and 8 M_ash.

2. **Leaching conditions:** The Honda protocol used 15 M HNO_3 (p.A.) for the acid leaching [97]. However, for the next step, the Sr resin column (TRISKEM, Resin SR, Grade: A, Lot No.: FSRA230710, 100-150 µm), the sample should be in more dilute acid, e.g., 8 M HNO_3. Thus, it seemed worthwhile to test whether the concentration of the nitric acid affects the success of the leaching. Besides the changes of the concentration, the leaching efficiency with lower temperature and in no pressurized (but closed) containers, e.g., in disposable centrifuge tubes or 20 ml PFA vessels, instead of the 230°C on the hot plate in PFA vessels [97] was tested. Hence, acid leaching with a sandbath was investigated, starting at 60°C and slowly increasing the temperature to 70°C for a total leaching time of 3 h compared to the leaching at the hot plate in accordance with the Honda protocol.

3. **Omission of filtration:** In an effort to reduce, costs, and to further simplify the sample preparation, the omission of filtration prior to passing the sample solution through the Sr resin column (see below) was investigated as well. Despite the fact that the concrete and soil samples are not completely dissolved in the nitric acid during the acid leaching, it would be convenient to omit the filtration step using a 0.45 µm PTFE filter, as suggested in the Honda protocol [97]. Instead of filtering the sample, the new approach centrifuges the sample solution for 5 minutes at 4000 rpm prior to directly loading it onto the Sr resin column.

4. **Sr resin column:** The Honda protocol uses rather large volumes, e.g., 40 ml of 0.01 M HNO_3 to elute Sr from the resin column [97]. Here, passing through only 10 ml for each concentration of HNO_3 and adapting the used concentrations was investigated. Following the conditioning of the Sr resin column, the sample (without filtration) was passed through the column. Subsequently, 3 M HNO_3 was passed through the column to remove Earth alkaline elements, mainly Ca, as reported in Landstetter and Wallner (2006) [103]. This removal step is not applied in the Honda protocol [97]. To elute Sr, 10 ml of 0.05 M HNO_3 were passed through the Sr resin column [104, 105]. Following the conditioning of the Sr resin column, a total volume of 60 ml HNO_3 are used in the Honda protocol [97] compared to 30 ml now, which includes the new Ca removal step.

5. **Omission of dedicated Zr removal:** The Honda protocol applied an anion exchange following the Sr resin column to further reduce the Zr content of the sample [97]. It was tested if whether the Sr resin column alone would already reduces the Zr content from soil and concrete samples to a sufficiently low concentration. Since the ^{90}Zr suppression for ion-laser-interaction assisted AMS measurements at VERA is $> 10^{12}$ [31], the Zr content of fauna and flora samples without any anion exchange has never been a limiting factor. Therefore, it was decided to investigate the omission of a dedicated Zr removal step in favor of a faster, simpler, and more cost-efficient sample preparation.

6. **Reduction of HF for SrF_2 precipitation:** By calculating the required HF amount for the precipitation of SrF_2 stoichiometrically, assuming about 1 mg

of Sr, mainly from carrier addition, inside the sample, it was concluded that the previously used amount is much more than actually needed. The Honda protocol uses 1 ml of 48% HF for 1 mg of Sr in the sample [97], which is approximately a factor of 1000 more HF than needed. Hence, the reduction by approximately a factor of eight, using only 130 µl of 40% HF (suprapur®) was tested. This change should not only improve the laboratory safety, but also the chemical yield.

The results and the outcomes of these investigations are summarized in the following subsection, which ultimately led to the finalized sample preparation protocol described in section 3.5.

3.4.1. AMS results of the investigated modifications

In total, four samples with 1 g each were processed for this test batch. The results are shown in Fig. 3.4. With the exception of the omission of filtration, all other modification of section 3.4 were implemented and investigated in this batch. For the leaching temperatures specifically, it was investigated whether the low temperature leaching at 60 - 70°C using a sand bath vs. 230°C on a hot plate yields observable differences in the results. Hence, samples 15 M and 15 M_ash were leached on the hot plate in accordance the Honda protocol [97], while samples 8 M and 8 M_ash were leached in the sand bath. One data point that stands out is the outlier 15 M_ash. During the preparation of this sample, some of the acid was spilling out of the "closed" PFA vessel on the hot plate during the acid leaching. We interpret the significantly higher ^{90}Sr activity as losses of Sr from the carrier before ^{90}Sr from the sample dissolved and equilibrium between isotopes has been reached, thus, resulting in an apparently higher ^{90}Sr/^{88}Sr. For comparison, a sample of the same material (IAEA-447), which was measured at VERA using the Honda protocol for the sample preparation [97], marked with a blue triangle, is also shown in Fig. 3.4.
With the exception of the outlier, no significant difference is observed between the AMS results of the test batch samples, the information value of the IAEA-447 within 1σ or the AMS result of the sample processed with the Honda protocol. Therefore, all approaches, with the exception of the outlier sample 15 M_ash, yield

accurate results. However, the Honda protocol ashes the samples and leaches with 15 M HNO_3 [97] and the AMS result is accurate (see Fig. 3.4). This strongly supports the hypothesis that the 15 M_ash approach, without the spilling on the hot plate, would have also yielded accurate results. Hence, it was decided that the preferred sample preparation method to be ashing of soil samples, leaching with 8 M HNO_3 in a sand bath at low temperatures combined with the res of the tested modifications, e.g., reduced amount of nitric acid and HF, and omission of anion exhchange after the Sr esin column. This represents a safe, fast, and simple sample preparation.

Figure 3.3.: Picture showing the PFA vessel of sample "15 M_ash" shortly after the partial spillage of sample solution from the "closed" PFA vessel onto the hot plate. The blue circle highlights the dried residue of the spilled sample solution on the hot plate. This resulted in a measured ^{90}Sr/Sr ratio that was significantly higher than the information value of the IAEA-447 sample material [100].

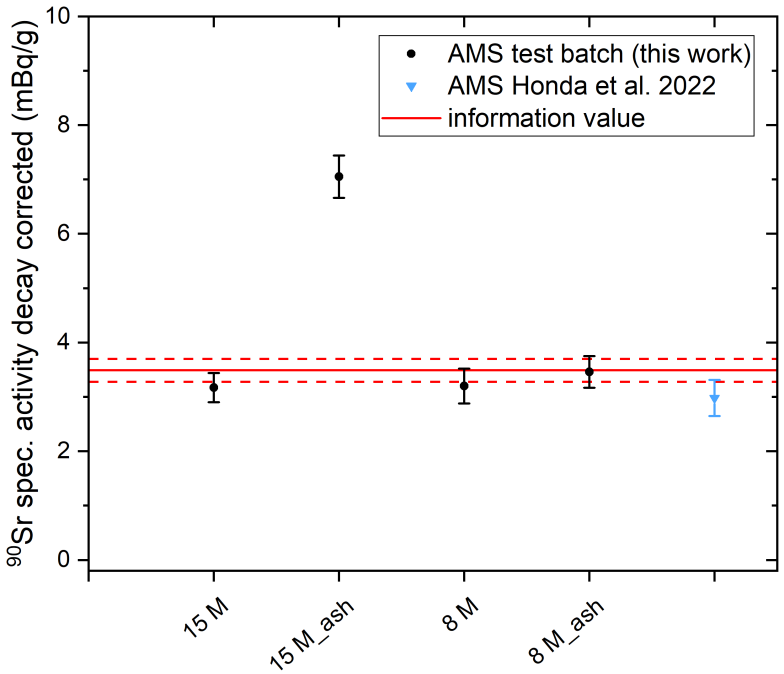

Figure 3.4.: Specific activity of ^{90}Sr, calculated from the ^{90}Sr/Sr AMS results, for different sample preparation approaches of the IAEA-447 reference material [97, 100]. Samples using 15 M or 8 M HNO_3 (p.A.) are labeled accordingly, samples which are ashed prior to processing are indicated by "_ash". Besides one outlier (15 M_ash), most probably due to losses of Sr carrier before full equilibration with ^{90}Sr during the leaching, there are no significant differences in the results for the different approaches. The continuous red line is the information value from the IAEA-447 certificate [100] and the dashed lines indicate its 1σ uncertainty. Note that shown values are decay corrected to the 08.10.2024.

3.5. New sample preparation protocol for ^{90}Sr in concrete and soil

Following the thorough investigation of the proposed modifications to the sample preparation of the Honda protocol and observing no drawbacks (see section 3.4.1 and section 3.6) the modifications were adopted to obtain the new fast, simple, and cost-efficient sample preparation for ^{90}Sr in soil and concrete. A flow chart of the new sample preparation protocol is shown in Fig. 3.5. For the rest of this work the new sample preparation will be referred to as the newly developed protocol. There is only a small difference between soil and concrete samples, i.e., in the

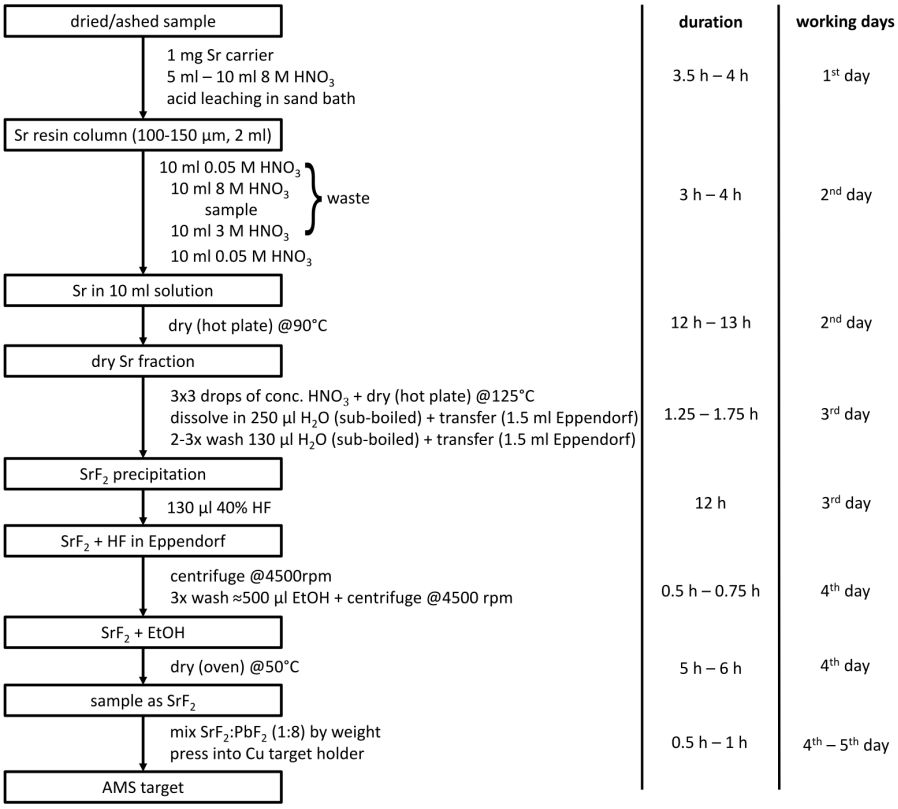

Figure 3.5.: Schematic flow chart for the newly developed sample preparation protocol for AMS measurements of ^{90}Sr in soil and concrete. The estimated duration of the individual preparation steps is also specified, together with the typical distribution over the working days. Note that the specified working hours can vary due to experience.

pre-treatment prior to the acid leaching. While the soil samples have been dried for 12 h at 105°C, as recommended in the IAEA certificate/reference sheet, and were subsequently ashed for 4 h at 550°C mainly to destroy any organic matter, the concrete samples were crushed and sieved to fine powder and then dried for 12 h at 90°C.

Following pre-treatment, about 1 mg of Sr carrier (LGC standard, Product No.: VHG-TSRN-500, Lot No.: 1123421-12, $(10\,000 \pm 50)$ µg Sr/ml in 5% HNO_3) is added into either 50 ml centrifuge tube or a closed PFA beaker. Subsequently, subsamples between 100 mg and 1 g of dry weight are added for concrete and soil, respectively. Afterwards, up to 10 ml of 8 M HNO_3 (p.A.) is added and then mixed with the samples. The samples are placed into a sandbath for acid leaching. The

initial temperature is 60°C for 50 min, followed by another 50 min at 65°C, and a final increase to 70°C for 80 min, resulting in a total leaching duration of 3 h (see Fig. 3.6 (a)). Following the leaching step, the leachate is centrifuged (5 min at 4000 rpm) and loaded directly on a conditioned 2 ml Sr resin (TRISKEM, Resin SR, Grade: A, Lot No.: FSRA230710, 100-150 µm) column [106]. For conditioning, the Sr resin column is cleaned from any Sr with 10 ml of 0.05 M HNO_3, followed by 10 ml of 8 M HNO_3 to condition the column. After loading the sample leachate, 10 ml of 3 M HNO_3 is used to remove alkaline earth metals, especially Ca [103], and finally Sr is eluted using 10 ml of 0.05 M HNO_3 [103, 104] (see Fig. 3.6 (b)). One might need to filtrate the leachate through a 0.45 µm PTFE filter if it is not possible to load the leachate without blocking the Sr column with sample residue. However, this was not needed in any of the treated samples and therefore omitted. Other elements present in the sample matrix, especially Ca, could lead to reduced retention of Sr within the Sr resin column. It is reported that a 2 ml resin volume can handle up to 300 mg of Ca [97, 103, 105]. In our case, the IAEA-447 contains about 172 mg Ca/g and the concrete samples contain about 85 mg Ca/g. Despite the absence of published data concerning the Ca content of the IAEA-375 material, it would require the material to consist of 60% of Ca to exceed the 300 mg threshold, since sample sizes of $\leq$ 500 mg have been processed. Hence, the potential limit of the Sr resin was never reached and it was not necessary to adapt the size of the Sr resin. The eluate is evaporated to dryness at 90°C in a PFA beaker on a hot plate ($\approx$ 12 h). A total of three times, three drops of concentrated HNO_3 (70%, p.A.) are added to the $Sr(NO_3)_2$ residue and evaporated at 125°C on the hotplate to dryness (see Fig. 3.6 (c) and (d)). Subsequently, the residue is dissolved in 250 µl H_2O (sub-boiled) and transferred into a 1.5 ml Eppendorf microtube. The PFA beaker is rinsed between two to three times with 130 µl H_2O (sub-boiled) to ensure a quantitative transfer to the tube.

About 130 µl HF (suprapur, 40%) is added for precipitation of SrF_2 (see Fig. 3.6 (e)). After resting for at least 12 h, the precipitate is separated from the solution by centrifugation (5 min at 4000 rpm) and washed three times using $\approx$ 500 µl of ethanol. At last, the sample is dried in an oven for approximately 5 - 6 h at 50°C (see Fig. 3.6 (f)) and subsequently the SrF_2 is mixed 1:8 by weight with PbF_2 and pressed into AMS target holder made from Cu.

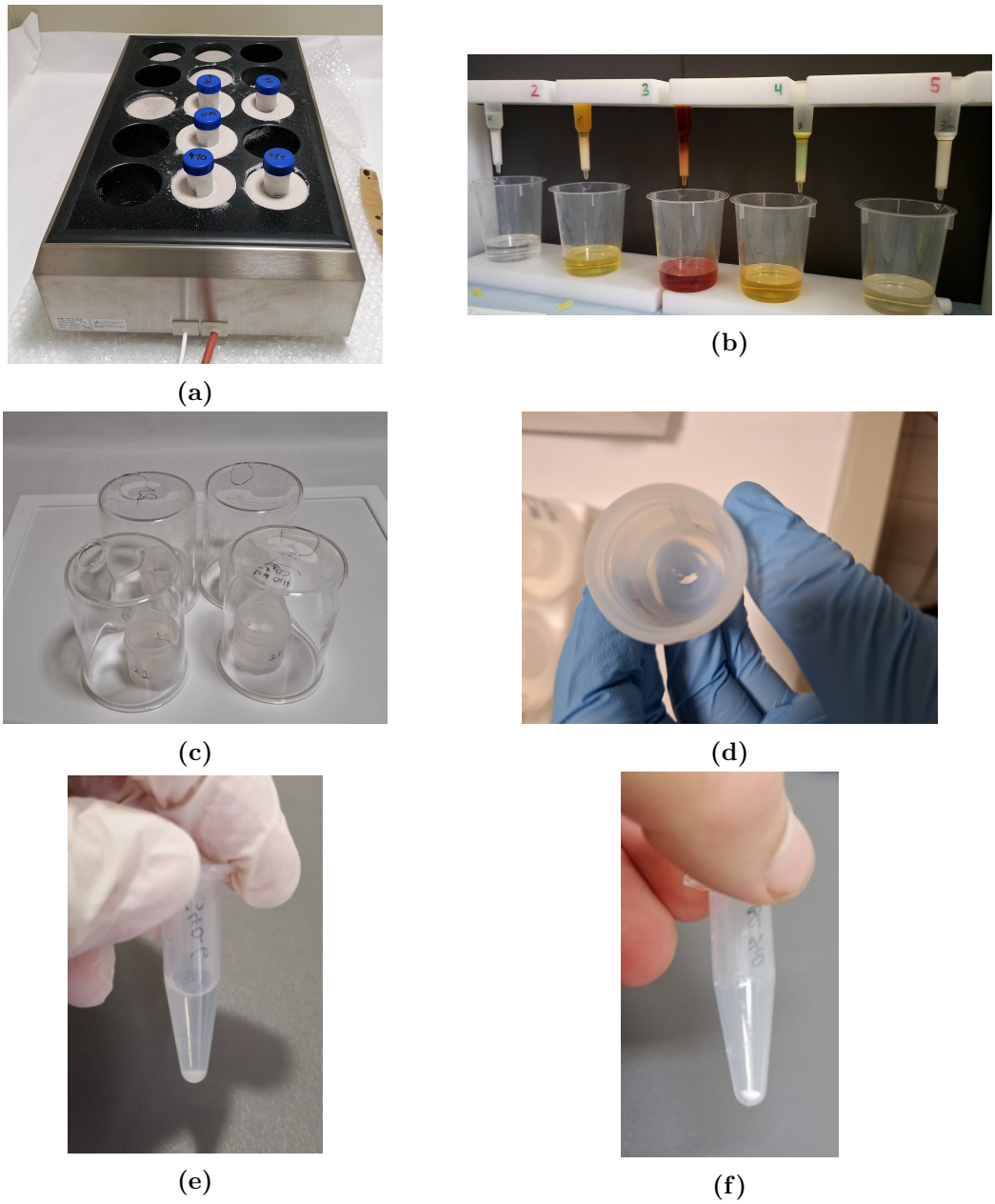

Figure 3.6.: Pictures showcasing different steps of the samples preparation. The pictures depict (a) acid leaching in the sandbath, (b) ion exchange using a Sr resin column, (c) drying of the sample solution on a hot plate, (d) dried $Sr(NO_3)_2$ residue after drying, (e) precipitation of SrF_2 using 40% HF, and (f) the dried and final SrF_2 powder prior to the mixing with commercial PbF_2 powder. Note that the pictures are not necessarily taken during the preparation of the same batch, but can be from different batches.

The combination of the implemented modifications of the newly developed sample preparation protocol combined reduce the working time per sample batch compared Honda protocol [97]. Despite the total amount of working hours being < 2 days (≈ 40 h after drying/ashing), the sample preparation of one sample batch will realistically take 4 - 5 working days to complete. This is due the fact that between some steps there are significant down times, e.g., SrF_2 precipitation (see Fig. 3.5), where other work can be done in parallel. The most labor-intensive step, without significant down time, is the Sr resin column step, which lasts until the drying of the Sr fraction on the hot plate begins. However, the newly developed protocol saves time here as well, since only a total of 30 ml of acids at different concentrations are used after conditioning of the column compared to the 60 ml used in the Honda protocol [97]. This shortens the time, as less acid volume has to pass through the Sr resin column and only 10 ml instead of 40 ml of Sr-containing eluate is to be evaporated on the hot plate after the Sr column.

3.6. Validation of the sample preparation

To validate that the newly developed protocol produces accurate results, AMS measurements were conducted on the soil reference materials IAEA-375 and IAEA-447 and on contaminated reactor concrete samples from Jülich (Germany), which were provided by the JEN mbH. The AMS measurements have also further validated the low detection limit of ion-laser-interaction assisted AMS measurements at VERA.

3.6.1. AMS results of the soil samples

Three samples of the IAEA-375 material and two additional samples of the IAEA-447 material were processed using the newly developed protocol described in section 3.5. The number of processed samples and their dry mass for both IAEA reference materials are summarized in Tab. 3.2.
Since the ^{90}Sr activity of the IAEA-375 material is approximately one order of magnitude higher than for the IAEA-447, the processed mass was adapted in order to yield similar ^{90}Sr/Sr ratios during the AMS measurement, and thus reduce the

Table 3.2.: Summary of the total number of processed soil samples used for the validation of the newly developed protocol. Note that one of the three IAEA-447 samples was already processed in the test batch in which the modifications to the Honda protocol were investigated.

sample material	number of processed samples	dry mass (g)
IAEA-375	1	0.100
	1	0.250
	1	0.500
IAEA-447	3	1.000

risk of potential cross-contamination in the ion source. Three distinct sample masses were processed as a homogeneity test of the material, i.e., to determine whether a significant difference in the AMS results for the IAEA-375 is observable. According to the IAEA-375 reference sheet, the use of a minimum of at least 6 g of sample material is recommended for radionuclide analysis in order to ensure homogeneity of the radionuclides within the sample [99].

The IAEA-447 reference material had also been processed and measured using ion-laser-interaction assisted AMS for the validation of the Honda protocol [97]. This already published result, together with the AMS results of the newly developed protocol are shown in Fig. 3.7. The newly developed protocol reproduces the nominal value well and is consistent with the result from Honda et al. [97].

For the IAEA-375 samples, no previously measured results are available for a comparison with samples processed with the newly developed protocol. The results of the AMS measurements are shown in Fig. 3.8. The average of the three samples reproduces the nominal value well within 1.65σ (95%). Within 1σ, the recommended value of the material [99] is barely outside the uncertainty of the average of the AMS samples. No significant trend in specific activity has been identified for the different sample masses that were processed. However, it could be the case that the AMS results are marginally shifted towards higher specific activities due to a slight inhomogeneities of the material at the level of a few hundred mg. Nonetheless, the AMS results of the IAEA-375 and IAEA-447 materials clearly indicate that the newly developed sample preparation protocol works for soil and yields accurate AMS results, even for lower sample masses than recommended by the IAEA.

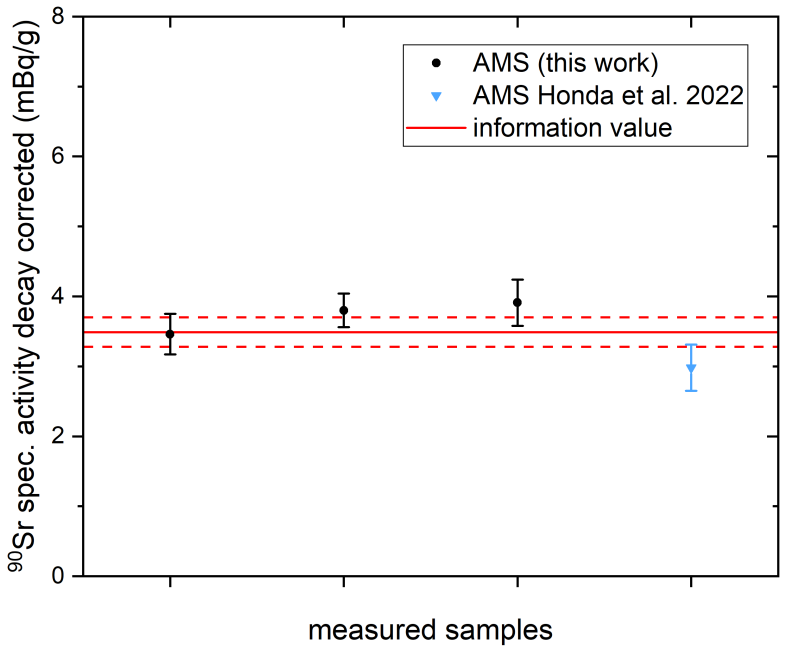

Figure 3.7.: Comparison of the specific activity of ^{90}Sr, calculated from the AMS results, between IAEA-447 samples prepared with the newly developed protocol and the Honda protocol [97]. The data point of the Honda protocol (light blue) is from an AMS measurement of 2022 performed at VERA. The newly developed protocol developed within this work reproduces the nominal value and shows that it works for this soil matrix. The continuous red line is the information value from the IAEA-447 certificate [100] and the dashed lines indicate the 1σ uncertainty. Note that all shown values are decay corrected to the 11.11.2024.

3.6.2. AMS results of the concrete samples

For the validation of the developed protocol for concrete samples, samples from two drill cores (see section 3.2) were processed, using the newly developed protocol described in section 3.5. For the AMS measurements, 1 g of sample material was used, with the exception of the sample with 90 mBq/g, for which only 100 mg were used. This was done to ensure a similar ^{90}Sr/Sr ratio across the processed batch. A total of ten concrete samples were analyzed, of which six samples were from the 330° angle drill core and four samples were from the 340° angle drill core. When calculating the specific activity of ^{90}Sr from the ^{90}Sr/Sr ratios from the AMS measurement, the intrinsic Sr content is taken into account. The intrinsic Sr content was was measured via XRF and was provided by the JEN mbH. The

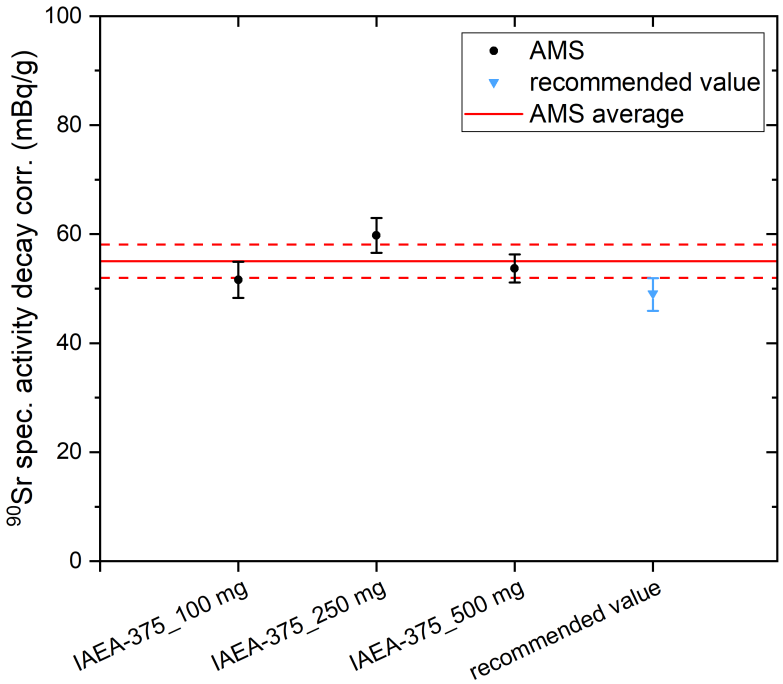

Figure 3.8.: Specific activity of ^{90}Sr, calculated from the AMS results, for different processed masses of the IAEA-375 reference material [99]. The blue data point represents the recommended value from the IAEA-375 reference sheet and the shown uncertainty is the given 95% confidence. Three samples were processed and the average of the AMS result reproduces the nominal value well within 1.65σ, while the nominal value lies barely outside the 1σ uncertainty of the measured samples. No significant difference in the specific activity is observable between the different processed sample masses. The continuous red line is the average AMS activity and the dashed lines indicate the 1σ uncertainty. Note that all shown values are decay corrected to the 11.11.2024.

comparison of the AMS results and the LSC results is shown in Fig. 3.9, where ideally all data points should align with the dashed 1:1 line. Within 1σ, the results of the AMS and LSC measurements are consistent, except for one sample, where the AMS measurement result yields a significantly lower ^{90}Sr activity compared to the LSC measurement (marked in Fig. 3.9 with red dashed lines). This sample was from the 340° drill core, specifically from the section 2 - 4 cm away from the surface. Notably, this sample yielded the lowest measured activity of ^{90}Sr at (0.068 ± 0.036) mBq/g. In comparison, the 0 - 2 cm section of the same drill core had a significantly higher ^{90}Sr activity at (3.05 ± 0.25) mBq/g. Inspection of the reported LSC values shows that the data would fit nicely if the LSC or AMS results were be reversed for these two samples. One potential explanation for this

discrepancy is an unintentional mix up of the samples during sample preparation. While this is not impossible, it is quite unlikely, as great attention was paid to avoid a mix up between these samples specifically. Another potential explanation is that the processed sample material was not homogeneous on a 1 g level, given that only 1 g out of a total mass of around 150 g was processed. Hence, these small aliquots could result in different activities for ^{90}Sr depending on the homogeneity of the sample material. To verify this, further analysis of additional samples would be required. However, even with this one discrepancy, the data clearly shows that the sample size reduction from 1 g down to 100 mg is working and produces accurate results using ion-laser-interaction assisted AMS. Additionally, the results demonstrate that ion-laser-interaction assisted AMS has a significantly lower detection limit (LoD) than LSC and is capable of measuring samples below the LoD of LSC with high precision ($< 10\%$).
In cases where the homogeneity of the sample material cannot be guaranteed at 1 g or less, the development of a method for processing larger samples, i.e., up to 10 g of sample material, was investigated. Once more, the aim was to minimize the preparation time and cost for the sample preparation of large samples, while also obtaining accurate results representative of the entire sample mass. Hence, the newly developed protocol was scaled up for the acid leaching from 1 g up to 10 g, i.e., that the processed sample material, the added Sr carrier, and the 8 M HNO_3 for the leaching were increased by a factor of 10. However, following the acid leaching, only a small liquid aliquot of the leachate, equivalent to a 1 g sample, was further processed with the newly developed protocol as described in section 3.5. With this approach, two 10 g samples of the 330° drill core sample with a ^{90}Sr activity of 90 mBq/g were leached using 100 ml of 8 M HNO_3. From each 10 g leachate, two subsamples of 10 ml were taken and further processed and analyzed. The results of the AMS measurement of the four "10 g samples" are shown in Fig. 3.10, along with the result of the 100 mg sample from the previous batch for comparison. Within the 1σ uncertainty, all four "10 g samples" match the LSC results. This shows that the approach of leaching a large sample and subsequently taking a small liquid aliquot of the leachate for further processing yields accurate and representative results for the entire sample that was leached. Concurrent, the time and costs are considerably reduced, as the amount of Sr resin, the most ex-

pensive chemical product used in the newly developed protocol, and acids required for processing are significantly decreased. The comparison of the results obtained from the "10 g sample" approach and the 100 mg sample strongly indicate that this sample material is homogeneous on a 100 mg level, in accordance with the expectations derived from the preceding measurement (see Fig. 3.9). However, if the homogeneity of any future material is uncertain, the "leachate aliquot" approach will produce SrF_2 that can be readily measured by ion-laser-interaction assisted AMS.

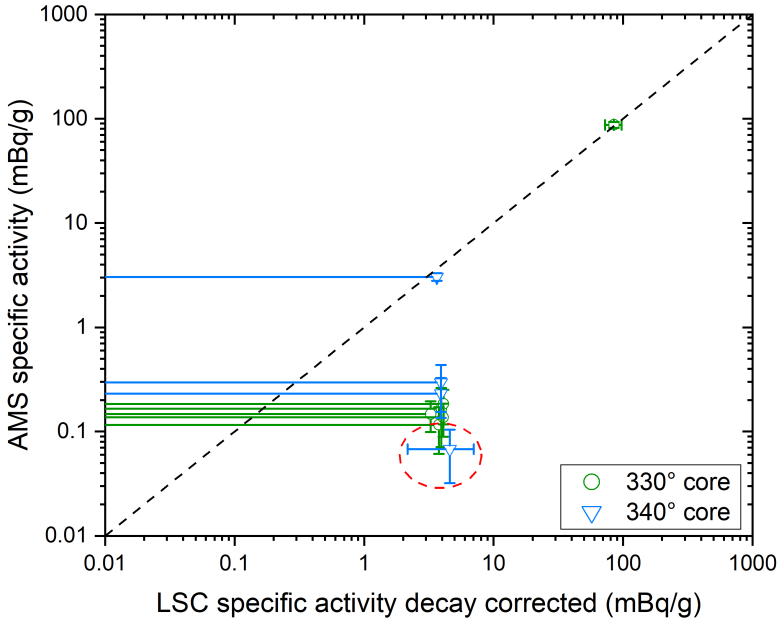

Figure 3.9.: Specific activity of ^{90}Sr, calculated from the AMS measurements, plotted against the specific activity from LSC measurements of contaminated concrete samples. Two drill cores from different angles 330° (green, circle) and 340° (blue, triangle) were investigated. The only discrepancy between the results of the two techniques is highlighted by a red dashed ellipse. The dashed black line represents the 1:1 line. For the majority of LSC measurements, only upper limits are available, as the activity was below the LoD. This is indicated by error bars going in one direction for those samples. Note that the shown LSC values are decay corrected to the 08.10.2024, which represents the date of the AMS measurement.

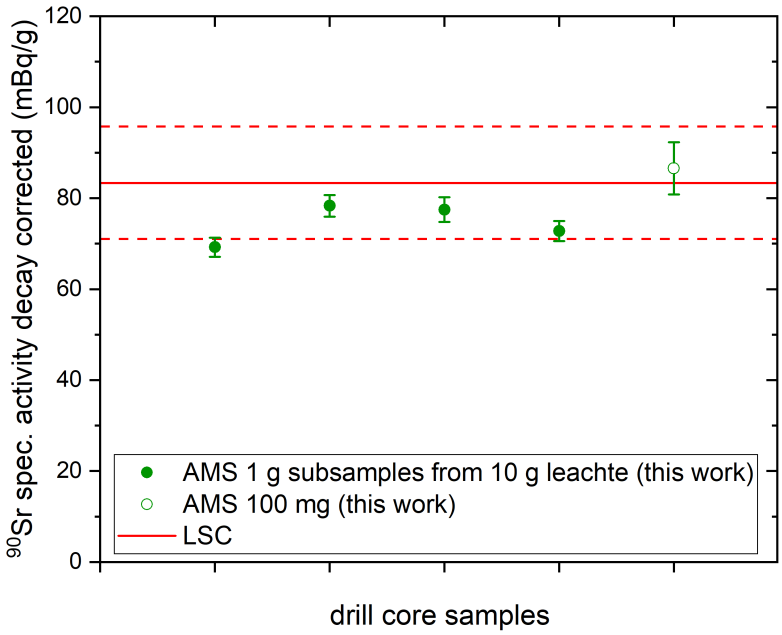

Figure 3.10.: Specific activity of ^{90}Sr, calculated from the AMS measurements, of the concrete drill core for the "leachate aliquot" approach. The green and filled data points are the processed samples of the "10 g sample" approach. The open circle data point corresponds to the processed 100 mg sample from Fig. 3.9. Processing a small liquid aliquot from a larger sample produces accurate results within 1σ. No significant difference between the 10 g and the 100 mg sample can be observed, which indicates homogeneity on a 100 mg level. Note that all shown values are decay corrected to the 28.02.2025.

3.7. Target performance of processed samples

The target qualities are visualized in Fig. 3.11 by plotting quality factors of the processed samples against their chemical yields (defined in section 3.3). The shown data includes the modification approaches with the IAEA-447 material, as described in section 3.4.1.

All samples that have been processed using the newly developed protocol described in section 3.5, yield high quality factors and chemical yields. More specifically, the average quality factor was determined to be $(93 \pm 2)\%$ for concrete samples, $(90 \pm 3)\%$ for the IAEA-375 samples, and $(97 \pm 2)\%$ for the IAEA-447 samples. Furthermore, comparing the IAEA-447 quality factor of samples processed with the Honda protocol at 57% with the average quality factor of the IAEA-447 samples

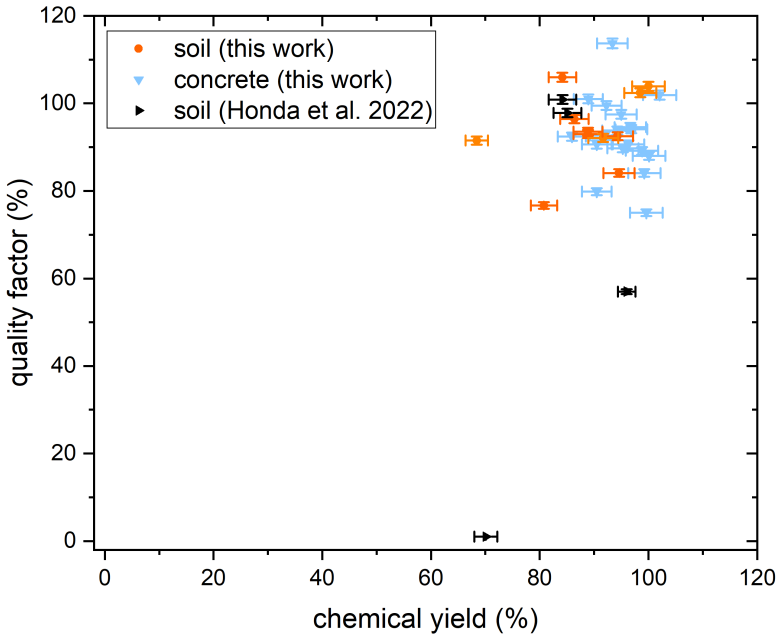

Figure 3.11.: Gravimetric chemical yield against the quality factor for all processed samples, including the modification test approaches. All samples processed with the newly developed protocol provided high chemical yields and quality factors around 90%, respectively. For comparison, soil samples processed with the Honda protocol (black) were taken from Honda et al. 2022 and are shown as well [97].

processed with the newly developed protocol at $(97 \pm 2)\%$, one can deduce that this corresponds to an improvement of the quality factor by roughly 70%. This means that on average the samples processed with the newly developed protocol yield about a factor of 1.7 higher ion currents compared to the average ion current from samples processed with the Honda protocol [97], which directly translates to higher counting rates of ^{90}Sr during the AMS measurements. In this specific study, the improvement of the quality factor translated to a count rate improvement of roughly 89%, nearly doubling the ^{90}Sr counts in the same measurement time. Assuming that there are no significant differences between two AMS measurements, e.g., ion cooler or accelerator transmission, other than the sample performances due to the used sample preparation protocol, this correlates to an improved AMS measurement efficiency by 70% for this data set. In other words, the predominant factor influencing the uncertainty of ion-laser-interaction assisted AMS measurements at present is the counting statistic,which now has been improved with the

newly developed protocol. To obtain an overall value for the improvement of measurement efficiency by the newly developed protocol, more samples must be processed with both sample preparation protocols, as the improvement could vary depending on the sample matrix.
Taking a closer look at the chemical yields separately for each material, the calculated average chemical yield for concrete samples is $(95 \pm 1)\%$, $(89 \pm 5)\%$ for the IAEA-447 samples, and $(93 \pm 2)\%$ for the IAEA-375 samples. In a previous study of ^{90}Sr, AMS measurements using ILIAMS at VERA have been performed for the IAEA-447 reference material as well [97]. By comparing the chemical yield of the Honda protocol of $(96.2 \pm 1.6)\%$ [97] with that of the newly developed protocol of $(91 \pm 4)\%$, no statistically significant difference in chemical yield was observed between the two methods. However, the additional comparison of the quality factors for the same samples shows that the quality factor of samples processed with the Honda protocol is 57% [97], while the newly developed protocol yields an average quality factor of $(97 \pm 2)\%$. Since the chemical yield is determined by gravimetry, the potential presence of other contaminants in the SrF_2 weight is not taken into account. The absence of SrF_2 in a target may ultimately result in an acceptable "chemical yield", provided that an equivalent amount of CaF_2 has been precipitated. Hence, this significant difference in ion source output is interpreted as a reduction in CaF_2 and other contaminants in the SrF_2, for samples processed with the newly developed protocol. This hypothesis is reinforced by the observation that the Honda protocol [97] does not utilize a step with 3 M HNO_3 when using the Sr resin column, which is usually used to remove Ca and other Earth alkaline metals [103].

4. Investigations and AMS measurements of environmental samples after validation of the newly developed protocol

Following the validation of the newly developed protocol, it was used to process and analyze additional soil and concrete samples from various locations. Furthermore, an additional modification to the newly developed protocol was investigated with the objective of further reducing the costs of the sample preparation. All AMS measurements in this chapter were conducted using the established ILIAMS setup at VERA. The measurement routine for ^{90}Sr at VERA is described in detail in section 3.1. A complete list of all samples that were processed for this work can be found in Appendix C. To avoid confusion, all mentioned dates of this chapter are in the format of DD.MM.YYYY.

4.1. Modification of the newly developed protocol for potential cost reduction

The most expensive chemical product of the sample preparation is the Sr resin itself [107]. The cost of a 2 ml Sr resin column is approximately 50 €. This means that the total cost of per sample with the newly developed protocol is > 50 €, even if the Ca content is below the critical threshold of around 300 mg/2 ml of Sr resin material [97, 103]. Should a sample exceed this Ca content, the used Sr resin material would require adaptation. However, this would result in a significant

increase in cost and would contradict the objective of the newly developed protocol. Thus, the reduction of Ca for samples with unknown or high Ca content was investigated in order to maintain or even further reduce the processing costs per sample. Due to the additional processing step, the required time for the sample preparation will increase by a total of $8-12$ h. This modification to the sample preparation of the newly developed protocol will be referred to as the modified protocol. Additionally, for samples with low intrinsic Ca content, the Sr recovery using reduced amounts of Sr resin is also something that should be investigated in the future. In such cases, this approach has the potential of further reducing processing time and costs of the sample preparation.

The general concept for the removal of Ca is to precipitate it as CaF_2, while Sr remains dissolved in the sample solution. The precipitation process is initiated by the addition of HF. The HF addition corresponds to approximately 1% of the total volume of the sample solution, given the use of 40% HF. This step is carried out subsequent to the acid leaching step of the newly developed protocol (see Fig. 3.5). Hence, the sample preparation was done in accordance with the newly developed protocol described in section 3.5, up to the Sr resin column step. Subsequent to the acid leaching, 1% of HF was added to the sample solution, i.e., 1 ml of 40% HF is required for 10 ml of sample solution. The precipitate can be separated from the sample solution by centrifuging at 4000 rpm for 10-15 minutes. Ideally, the sample solution would now contain no or at least significantly less Ca, such that no further modifications to the newly developed protocol are required.

The test was conducted on a 1 g concrete sample with approximately 1 mg of stable Sr in it. For this purpose, 10 ml of the remaining sample solution from the "10 g sample" leaching tests was used (see section 3.6.2). Following the addition of the Hf, the formed precipitate was separated from the sample solution. The remaining of the sample solution was used to process the sample normally using the newly developed protocol (see Fig. 3.5). Subsequent to the completion of the sample preparation, white powder remained in the Eppendorf tube, which was comparable to the expected amount of SrF_2 in the absence of the additional Ca removal step. The fully processed sample and the precipitate that was separated prior to the Sr resin column were both analyzed performing mass scans. The samples were also measured for one run (18 minutes) by AMS. The results are summarized in the following subsection.

4.1.1. AMS results of the cost reduction tests

The cost reduction tests that were the subject of the investigation refer to the modified sample preparation of the newly developed protocol, as described in the previous section (section 4.1). As a reminder, the modified sample preparation will referred to as the modified protocol. The modified protocol includes an additional Ca removal step prior to the Sr resin column.

The two samples, the fully processed one and the precipitate before the Sr resin column (residue sample), were both mixed with PbF_2 in a ratio of 1:8 by weight and pressed into Cu targets. Initially, a preliminary test was conducted to determine whether the samples would yield significant ion currents of CaF_3^- and SrF_3^-. For this purpose, the most abundant nuclides of Sr and Ca, i.e., ^{88}Sr and ^{40}Ca, were selected. Therefore, $^{88}SrF_3^-$ and $^{40}CaF_3^-$ were extracted from the ILIAMS ion source and measured in the Faraday Cup (FC) after the 90° bending magnet (see Fig. 3.1). Subsequent to this, mass scans with narrow slits ($\pm$ 1 mm) in the range from 75 amu to 200 amu were conducted. A processing blank that had been measured in a previous measurement was used for tuning. The results of the mass scans of the relevant mass ranges, i.e., around 97 amu and 145 amu, are shown in Fig. 4.1. The fully processed sample produced measurable ion currents for SrF^-, SrF_2^-, and SrF_3^-. As expected, the most prolific formed molecule was SrF_3^-, which had around 300 nA with the used ion source settings. In comparison, the residue sample produced only negligible SrF_3^- ion current around 6 nA. A significant portion of this current could also stem from the molecular interference of $^{63}Cu_2F^-$. At mass 97 amu ($^{40}CaF_3^-$), the residue sample produced approximately 300 nA, while no ion current was measured in the processed sample, corresponding to less than 100 pA in the FC. With the same ion source settings, the processing blank used for tuning produced around 455 nA of $^{88}SrF_3^-$. During an AMS measurement, this would correspond to a quality factor of approximately 66%.

Since the remaining sample solution from the 10 g leaching tests (see section 3.6.2) was used for this test, a direct comparison of the chemical yields of the sample processed with the modified protocol and the newly developed protocol is possible. The average chemical yield of the concrete samples processed with the newly developed protocol is (93 ± 3)%, compared to a chemical yield of (63 ± 2)% for

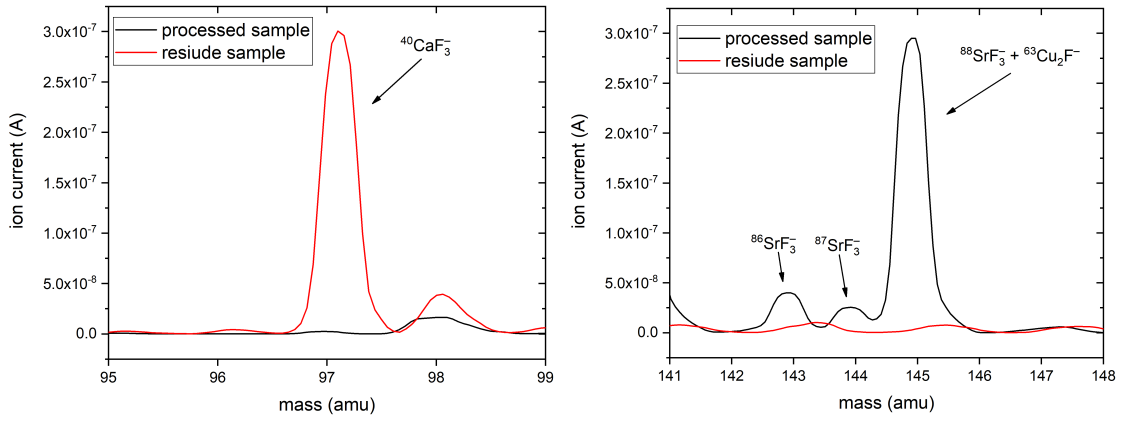

Figure 4.1.: Mass scans conducted with the fully processed (black) and the residue sample (red) to determine ion current output for $^{40}CaF_3^-$ and $^{88}SrF_3^-$. The images depict (a) the mass scans around mass 97 amu ($^{40}CaF_3^-$) and (b) the mass scan around mass 145 amu ($^{88}SrF_3^-$). The residue sample yields high ion currents around of 300 nA of $^{40}CaF_3^-$ and negligible ion currents of $^{88}SrF_3^-$. Conversely, the fully processed sample has the exact opposite properties and reproduces the natural abundance of the stable Sr isotopes.

the sample fully processed with the modified protocol. This corresponds to a 32% reduction in chemical yield when introducing the Ca removal step, strongly indicating that part of the Sr is lost using the modified protocol in comparison to the newly developed protocol. Therefore, the modified protocol would only be of interest in cases where a significant amount of Ca is present, with the aim of saving significant costs at the expense reduced chemical yield.

In addition to these tests, both samples were measured for one AMS run (18 minutes) to check the $^{90}Sr/Sr$ ratio and the quality factor. The result of this measurement is shown in Fig. 4.2. As expected from the previous tests, the quality factor of the fully processed sample was high at $(84 \pm 1)\%$ and the residue sample was extremely low at $< 1\%$, which is essentially equivalent to no Sr output. The $^{90}Sr/Sr$ ratios of the fully processed sample and the residue sample were (1.92 ± 0.10) and (1.66 ± 1.02), respectively. Compared to the average $^{90}Sr/Sr$ ratio of samples processed with the newly developed protocol, the fully processed sample is approximately two times higher. However, to verify whether this result is statistically significant further investigations are required. A comparison of the

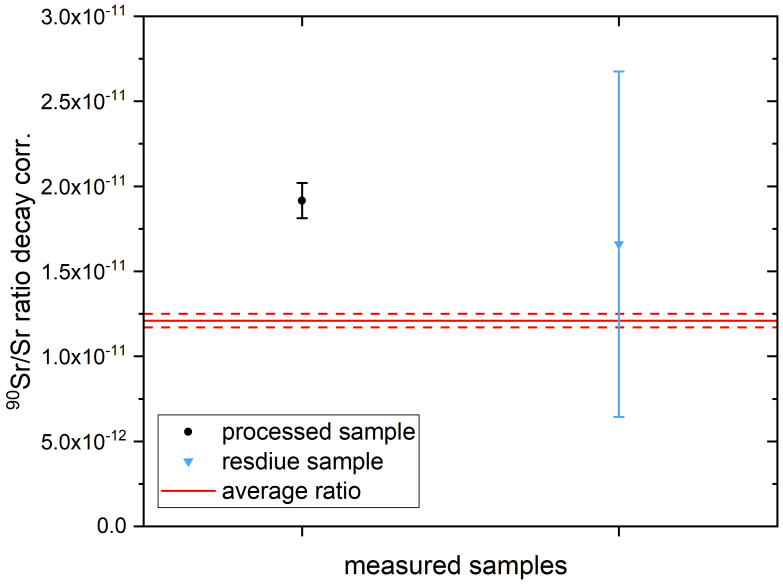

Figure 4.2.: Measured ^{90}Sr/Sr ratio of a sample processed with the modified protocol compared to the average ratio of the same sample material processed with the newly developed protocol. The continuous red line depicts the average ratio of samples processed with the newly developed protocol and the dashed lines indicate the 1σ uncertainty. It appears that samples processed with the modified protocol tend to yield slightly higher ^{90}Sr/Sr ratios. However, whether this is statistically significant requires further investigation. Due to the very low quality factor of $< 1\%$ of the residue sample the accuracy of the result can not be guaranteed and should be treated with caution. Note that the shown data was decay corrected to the 20.06.2025.

residue is difficult due to the poor target performance, which directly correlates to the low counting statistics and the large 1σ uncertainty. Nevertheless, this was anticipated, given that the residue sample is expected to be free of any Sr. For this reason, the result of the residue sample should be treated with caution. In general, measured isotopic ratios of samples with very low quality factors, especially below 1%, should be treated with caution, since the accuracy of the measurement can not be guaranteed for samples with no significant ion source output compared to the standards used in the same beamtime.

Overall, the tests of the modified sample preparation were successful. The processed sample performed well during the AMS measurement, as indicated by the high quality factor. Moreover, the results demonstrate that Ca can be removed by a dedicated removal step using HF. In contrast, the results also indicate that some

of the Sr is lost, which results in a worse chemical yield. Furthermore, the accuracy of the measured ^{90}Sr/Sr ratios might be effected. In order too validate these results, it is necessary to process additional samples with both sample preparation protocols. This will allow for direct comparison of the chemical yields, quality factors, and measured isotopic ratios. Additionally, the introduction of HF prior to the Sr resin column step significantly increases the risk of the sample preparation. Hence, the cost-risk factor, prolonged preparation time, and potential reduction of the target performance resulting from the modified protocol must be carefully evaluated for each sample batch individually.

4.2. Analyzed samples

The analyzed samples can be divided into three different batches: The Rur river batch, the contaminated soil batch and the concrete batch. The Rur river batch consists of soil samples and one singular sediment sample. The samples were collected at and near the Rur river, approximately 4 km away from the Research center in Jülich, using a 1 m long soil sampler and a hand shovel. Two soil samplers were used to collect the soil samples, one from an island on a small branch directly in the Rur (see Fig. 4.3 (a)) and the other one near a tree on the meadow close to the Rur (see Fig. 4.3 (b)). Following the collection of the soil samples, they were divided into sections according to the optical layers of the extracted soil (see Fig. 4.3 (d)). The sediment sample was collected directly from the Rur using a hand shovel (see Fig. 4.3 (c)). A table summarizing all samples taken from the different sites, along with additional information, e.g., precise location of the sampling sites, is provided in Appendix B

The second analyzed soil batch consists of two contaminated soil samples that were provided by the Research Center Jülich (11-1248 & 11-1375). Since these two samples have been measured by LSC, the specific activities of ^{90}Sr are known. Both samples have a high contamination level on the order of a few Bq/g. The precise ^{90}Sr activities and the corresponding reference dates are listed in Tab. 4.1.

The final batch consists of concrete samples, more specifically from three concrete samples from various shut down research reactors in Germany. Two samples are from reactors located in Karlsruhe, the "Kompakte Natriumgekühlte Kernreak-

Table 4.1.: List of the specific activities of ^{90}Sr measured by LSC, along with the corresponding reference dates for the two contaminated soil samples 11-1248 and 11-1375. Note that the 1σ relative uncertainty of the LSC measurements is quite large with 30%.

sample name	specific activity (Bq/kg)	reference date
11-1248	5485 ± 1645	22.04.2022
11-1375	2690 ± 826	31.03.2022

(a)

(b)

(c)

(d)

Figure 4.3.: Pictures of the sampling sites of the Rur river samples and of one of the soil samplers. The pictures show (a) the island site, (b) the meadow site, (c) the sediment site and (d) the different colored optical soil layers of a filled soil sampler. Note that the red circles of (a) and (b) show the location of the soil samplers and that the sediment sample was directly collected using a hand shovel.

toranlage Karlsruhe" (KNK) and the "Mehrzweckforschungsreaktor Karlsruhe" (MZFR). The third sample is from the "Rossendorfer Forschungsreaktor" (RFR) located in Dresden-Rossendorf. All three samples are samples from the biological shields of the reactor cores. In contrast to the samples from the AVR reactor (see section 1.2.4), no contamination with ^{90}Sr is known. Thus, only low ^{90}Sr concentration close to the blank level are to be expected from these samples. Pictures of the bottles containing some of the analyzed samples from the different batches are shown in Fig. 4.4.

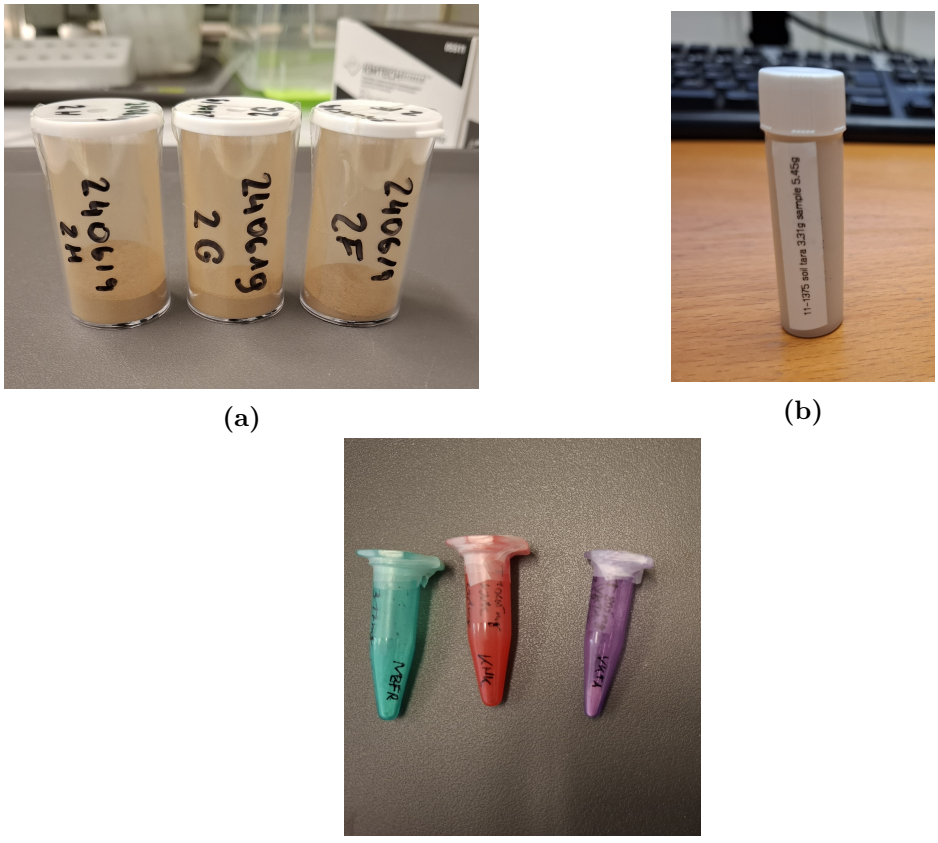

Figure 4.4.: Pictures of containers storing some of the sample material that was analyzed subsequent to the validation of the newly developed sample preparation protocol. The images depict (a) Rur river samples, (b) the soil sample 11-1375, and (c) Eppendorf tubes with the reactor concrete. Note that the 11-1248 soil sample and numerous Rur river samples are not shown in the pictures.

4.3. Sample preparation of the Rur river samples

The sample preparation of this batch is noteworthy as the modified protocol was used instead of the newly developed protocol. Since no information regarding the Ca content of these samples was known and the promising results of the Ca removal tests using the modified protocol (see sections 4.1 and subsection 4.1.1), it was decided to process the samples with the modified protocol, despite the risk of lower chemical yields. This was done because the processed sample material ranged from 2.5 g to 10 g, which would have resulted in significantly higher costs per sample, as it would have required conservative estimates of the Ca content. The ^{90}Sr content in the samples was also unknown, but was estimated to be rather low. Consequently, more sample material was processed while maintaining the addition of 1 mg of stable Sr carrier. This ensures that the measured ^{90}Sr/Sr ratio will be higher compared to 1 g samples, resulting in higher counting statistics and thus improving the precision.

Overall, the sample preparation with the modified protocol proved to be successful, with the majority of samples yielding reasonable chemical yields. However, one outlier was identified, with an extremely high chemical yield of $> 1000\%$. Excluding the outlier, the chemical yields ranged from 48% to 78%, resulting in an average chemical yield of $(69 \pm 5)\%$. This corresponds to a 26% reduction of the average chemical yield compared to the newly developed protocol for soil samples. However, the comparison does not account for differences in the sample matrices. From the experience gained during the initial test with the modified protocol (see section 4.1.1), it appears that the reduction in chemical yield stems from the variations in sample preparation, as both are of comparable magnitude.

In the case of the outlier sample (2I), it was the largest sample that was processed in this batch, with 10 g of sample material. Following the drying on the hotplate after the Sr resin column, first deviations from normal sample behavior became apparent. The $Sr(NO_3)_2$ in the PFA beaker, normally just white, contained a significantly higher amount of material than expected. additionally, the material had an orange tint (see Fig. 4.5 (a)). In contrast to $Sr(NO_3)_2$, this orange material was insoluble in the sub-boiled H_2O and remained as a residue in the Eppendorf tube upon transfer (see Fig. 4.5 (b)). Since it was clearly not Sr, the sample was

centrifuged for 10 minutes at 400 rpm and the residue was separated from the sample solution prior to the HF precipitation. As indicated by the chemical yield, the amount of material that precipitated far exceeds the amount of Sr carrier added to the sample (see Fig. 4.5 (c)). Consequently, the final sample material does not only contain SrF_2 but also other contaminants.

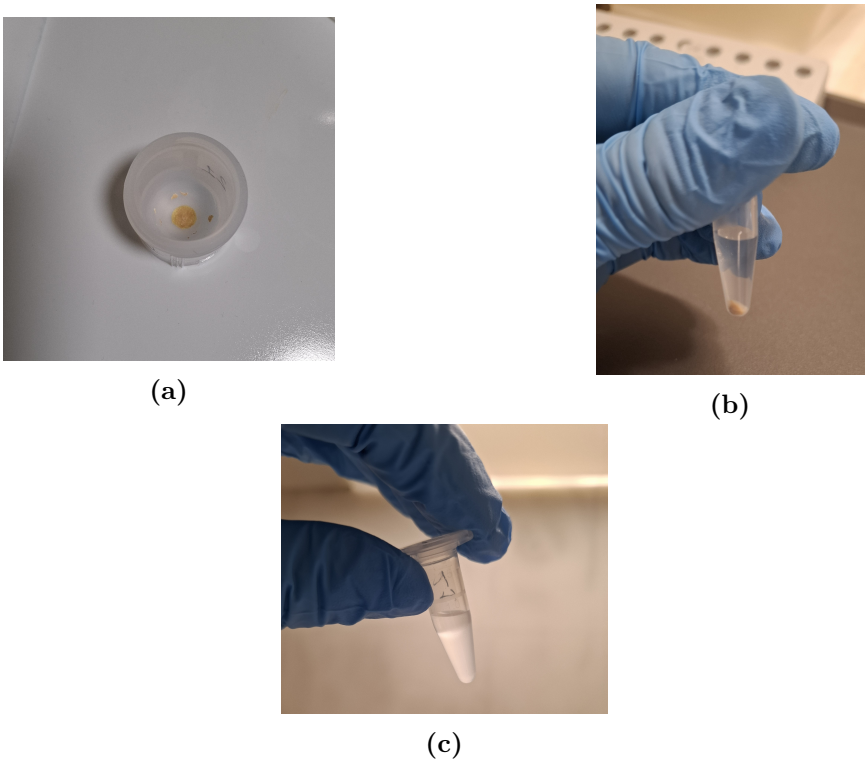

(a) **(b)** **(c)**

Figure 4.5.: Images of abnormal behavior of a sample during sample preparation, which indicates that the sample preparation did not work properly. The pictures depicts (a) the sample after drying on the hot plate containing a slight orange tint, (b) the sample after the addition of sub-boiled H_2O, containing an insoluble part and (c) the sample after the HF precipitation, where far too much material precipitated. Note that this is the only sample of the batch where the sample preparation did not work properly, resulting in a chemical yield of $> 1000\%$.

4.3.1. AMS results of the Rur river samples

A total of seven samples were processed and measured from the Rur river batch. More precisely, three samples from the soil sampler of the island site, three samples from the soil sampler of the meadow site, and one sediment sample (see section 4.2).

For both soil samplers, the top layer, a middle layer, and the bottom layer were processed and analyzed. The most important information of the analyzed samples from the island and meadow site is given in Tab. 4.2. More detailed information on the samples taken from the sampling sites of the Rur river batch can be found in Appendix B.

The results obtained from the AMS measurements of the Rur river samples are shown in Fig. 4.6. The specific activities of ^{90}Sr obtained from the island site display an increasing trend with depth. The top layer (1A, 0 - 21 cm) has the lowest activity of (0.325 ± 0.043) mBq/g, while the bottom layer (1J, 95 - 101 cm) has an activity of (3.23 ± 0.17) mBq/g. The samples from the meadow site show no trend correlating with the depth. All samples yield similar results of < 0.45 mBq/g. However, as mentioned in section 4.3, the sample preparation for the sample of the bottom layer failed (2I, 56 - 92 cm), thus the result should be treated with caution. Since only one sample was available from the sediment site, no depth trend can be discerned. Nevertheless, it is evident that the Sr concentration at this sampling site is the highest at (8.27 ± 0.34) mBq/g.

Prior to the measurement, it was expected that only low Sr concentrations around the global fallout of ^{90}Sr would be present in collected samples. Hence, only three samples from the island and meadow site were processed. A detailed and complete interpretation of the measurement data is complicated because several biomass layers are visually superimposed, which makes it difficult as a lot of factors need

Table 4.2.: Table summarizing the analyzed samples of the Rur river batch. One sample each from the top, middle, and bottom layer were processed and analyzed. The middle of the meadow site refers to the middle of the optical layers into which the sample was divided, and does not necessarily correspond to the middle of the soil sampler. More detailed information on the samples can be found in Appendix B.

sampling site	**sample ID**	**depth (cm)**	**layer**
island	1A	0 - 21	top
	1E	58 - 62	middle
	1J	95 - 101	bottom
meadow	2A	0 - 6	top
	2E	12 - 14	middle
	2I	56 - 92	bottom

to be considered, e.g., potential migration behavior between the layers. Nevertheless, the activities of ^{90}Sr obtained in some of the samples, e.g., the sediment sample and sample 1J (95 - 101 cm), exceed the expected values prior to the AMS measurement. It is evident that the sampling sites, with the exception of the meadow sampling site, are of interest for further study regarding ^{90}Sr. In order to obtain a more sophisticated interpretation of the presented data, a more thorough investigation is required. This could include the measurement of the remaining samples of the optical layers and the gathering of more samples in the vicinity of the measured sampling sites.

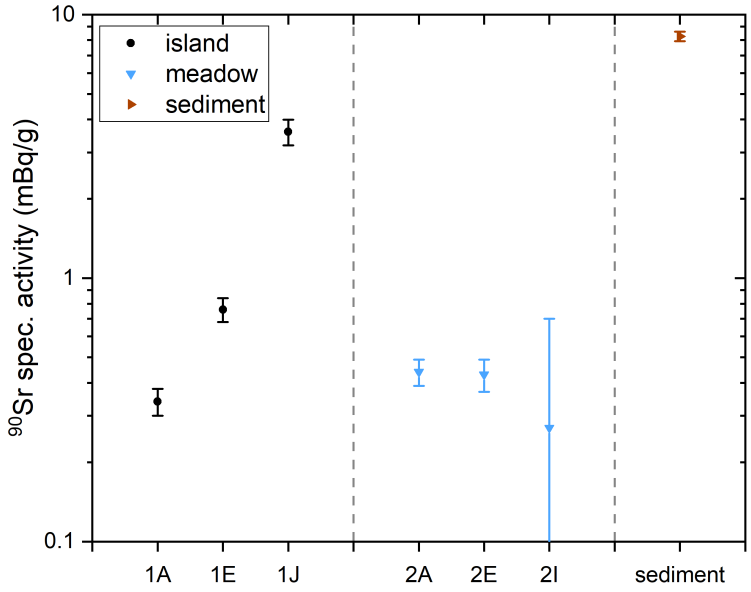

Figure 4.6.: Specific activity of ^{90}Sr calculated from the ^{90}Sr/Sr AMS results for the seven samples from the Rur river batch. The samples were collected from three distinct sampling sites, the island site (black), the meadow site (light blue), and the sediment site (brown). The specific activity of the island site is increasing with depth, while the activity of the meadow site remains constant. For sample 2I, the sample preparation was unsuccessful, resulting in a large uncertainty. A more thorough interpretation of the data is not straightforward and requires further investigations. Note that the results are not decay corrected, as all samples were measured in the same beamtime and the results refer to the AMS measurement date on the 20.06.2025.

4.4. AMS results of the contaminated soil samples

The two soil samples, 11-1248 and 11-1375, provided by the Jülich Research Center, are contaminated with ^{90}Sr, which was determined via LSC measurements. They were processed with the newly developed protocol (no dedicated Ca removal), described in section 3.5. Due to their high specific activities of a few Bq/g (see Tab. 4.1), only 100 mg of sample material was processed per sample. More specifically, for sample 11-1375, 100 mg of sample material together with 1 mg of Sr carrier was processed. For sample 11-1248, 100 mg of sample material together with 2 mg of Sr carrier was processed. This ensures that the ^{90}Sr/Sr ratios obtained during the AMS measurement of both samples are around $6{\cdot}10^{-11}$ and are on the same order of magnitude than the highest standard available at VERA (see Tab. 5.2).

The first sample material that was analyzed was 11-1375, since it is the less active sample. Two samples of 100 mg each were processed from the sample material. The AMS results of the two samples are shown in Fig. 4.7. The average activity of ^{90}Sr of the material is (38.18 ± 0.05) mBq/g. This is approximately 66 times lower than the 2508 mBq/g expected from the LSC measurement. Prior to the analysis of this sample material, all AMS measurement results were in good agreement with the LSC values, with the exception of one concrete drill core sample (see Fig. 3.9). Hence, this significant discrepancy between the results is unexpected and raises concerns about the accuracy of the two methods. A more thorough examination of the AMS data for ^{90}Sr in this measurement reveals no obvious indications that the AMS data is inaccurate. During the sample preparation, nothing noteworthy occurred, and both samples had reasonable chemical yields of approximately 80% and quality factors of 77% and 106%, respectively. Thus, neither the sample preparation nor the target performance hint at a faulty AMS measurement. Furthermore, during the same beamtime, four concrete samples from the 10 g leaching tests (see Fig. 3.10) and one sample from each of the CologneAMS reference materials (see Tab. 5.2) all yielded AMS results consistent with the expected values. Therefore, further supporting the accuracy of the AMS measurement during this beamtime. In the case of the concrete samples, the activity was known from a LSC measurement, and the activity for the reference materials was derived from calculations of a dilution series.

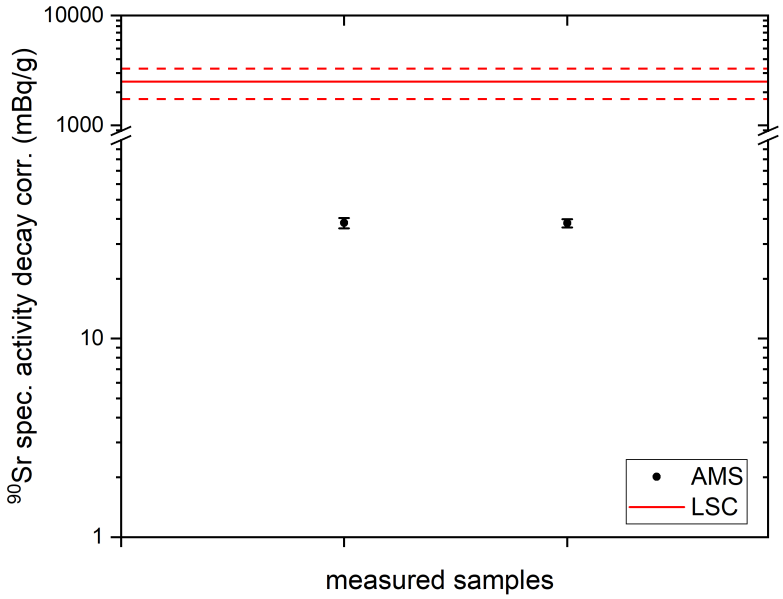

Figure 4.7.: Specific activity of ^{90}Sr for the two processed samples of the 11-1375 soil material. The AMS results are a factor of 66 times lower than expected from the LSC measurements. The large discrepancy of the AMS and LSC results hints at inaccurate results for at least one of the measurement methods. Note that there is a line break on the y-axis. The shown data was decay corrected to the 28.02.2025.

The second sample material that was sample 11-1248, and it was measured in a different beamtime than the two 11-1375 samples. Consequently, the material was processed in a separate batch. One 100 mg sample together with 2 mg of Sr carrier was processed. The result is shown in Fig. 4.8. The specific activity of ^{90}Sr, measured with AMS, is (86.00 ± 7.38) mBq/g. This result is approximately a factor of 58 times lower than the 5029 mBq/g from the LSC measurement. The quality factor and the chemical yield are in expected ranges of $(74 \pm 1)\%$ and $(65 \pm 2)\%$, respectively. From the 10 g leaching test, one quality control sample, corresponding to a 1 g sample with 1 mg of Sr carrier, was processed and measured as well. The measured ^{90}Sr/Sr ratio is in agreement with the average ratio of this sample material, which indicates good accuracy of the AMS measurement during this beamtime. However, it is evident that the AMS result is approximately 60 times lower than the LSC results for both soil samples, i.e., 11-1248 and 11-1375. This further supports the hypothesis that either AMS or LSC might not have produced accurate data for these samples.

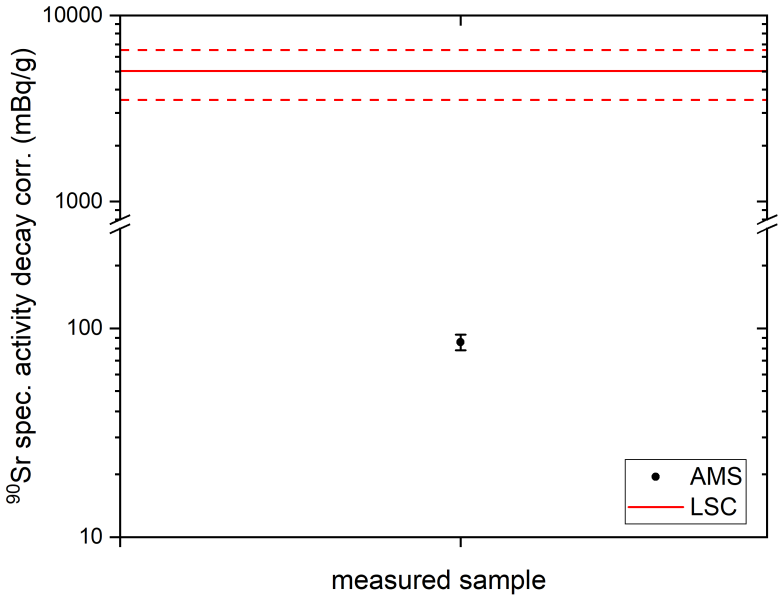

Figure 4.8.: Specific activity of ^{90}Sr calculated from the ^{90}Sr/Sr AMS results for the processed sample of the 11-1248 soil material. The AMS results are a factor of 66 times lower than expected from the LSC measurements. The large discrepancy of the AMS and LSC results hints at inaccurate results for at least one of the measurement methods. Note that there is a line break on the y-axis. Note that this data point was not included in Fig. 4.7 for visual clarity of the LSC values. The shown data was decay corrected to the 20.06.2025.

To conclude, there is no clear indication of problems during the AMS measurement or the sample preparation. However, two scenarios have been identified as potential sources of inaccurate AMS data. One explanation is that there might be a problem during the sample preparation that does not affect the calculated chemical yields or the quality factors of the processed samples. The most probable sample preparation step that could have such an effect is the acid leaching step, which extracts the intrinsic stable Sr and the ^{90}Sr in the sample material. In the event of incomplete extraction of the ^{90}Sr contained within the sample material, the measured ^{90}Sr/Sr ratio, and by extension the specific activity, will be lower than expected. This is due to the fact that the majority of the stable Sr is added separately and is not extracted from the sample itself. This would explain the lower ^{90}Sr activities measured by AMS and, concurrently, yield high chemical yields and quality factors. However, it remains unclear why the extraction of

^{90}Sr via the leaching would be incomplete for this sample matrix specifically. This would be perplexing, as it worked well with every other matrix investigated so far. An alternative explanation might be the inhomogeneity of the sample material on a 100 mg level. Due to the successful inhomogeneity test with the 10 g leaching approach (see section 3.6.2), it would be possible to leach a bigger sample mass and subsequently process smaller liquid aliquots. This approach would allow for investigation of the potential inhomogeneity of the two sample materials up to a 10 g level.
Overall, the unexpected discrepancy between the two measurement methods represents an interesting case that requires further investigations in order to resolve it.

4.5. AMS results of the nuclear reactor concrete samples

The last sample batch that was investigated were concrete samples from three different shut down research reactors (KNK, MZFR & RFR), described in section 4.2. The results are shown in Fig. 4.9. The results show that the samples from MZFR and KNK both have low activities for ^{90}Sr of ≤ 1.2 mBq/g. In the case of MZFR, it is even indistinguishable from the measured processing blank, which clearly indicates no ^{90}Sr contamination in the biological shield of the reactor cores. However, the RFR sample has an elevated ^{90}Sr signal of (73.21 ± 6.00) mBq/g. Despite no known ^{90}Sr contamination, the result indicates a contamination with ^{90}Sr for this research reactor. The results of the first investigation with concrete samples from the AVR reactor show that, even with known contamination, there can be significant differences in the ^{90}Sr content between angles of 10° (see section 3.6.2). Therefore, it would be of interest to analyze additional samples from this reactor to investigate whether the contamination of the biological shield is only local or distributed more evenly. Furthermore, these measurements once again highlight that the sample preparation works well and undermines the high abundance sensitivity for ^{90}Sr of ion-laser-interaction assisted AMS measurements.

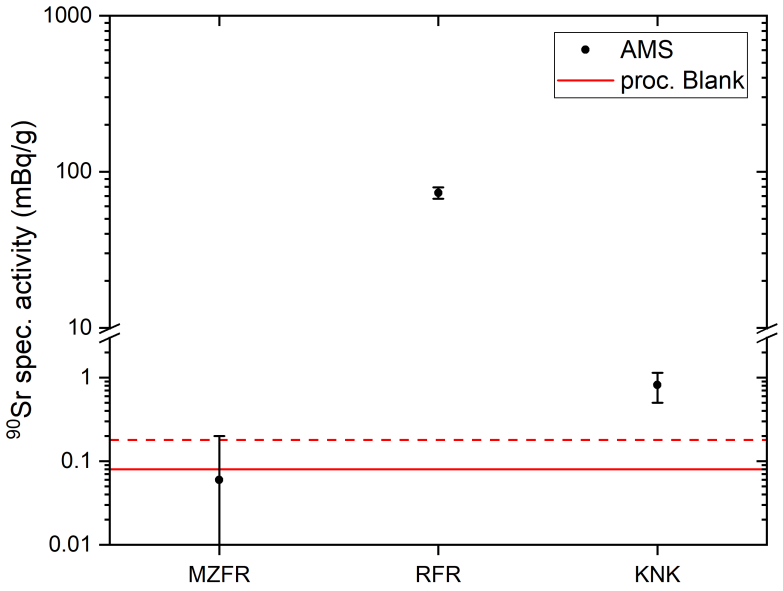

Figure 4.9.: Specific activity of ^{90}Sr calculated from the ^{90}Sr/Sr AMS results for three different nuclear research reactor samples. The continuous red line is activity of the processing blank and the dashed line indicate the 1σ uncertainty. The activity of the KNK sample is very low, while the activity of the MZFR sample is indistinguishable from the processing blank. Conversely, the RFR sample has a rather high ^{90}Sr activity of (73.21 ± 6.00) mBq/g, especially since there is no known contamination for this reactor. Note that the results are not blank corrected so that the data point of the MZFR sample could be shown.

4.6. Target performance of processed samples

As described in section 3.3, the quality factor (eq. 3.2) and the chemical yield (eq. 3.1) can be used to investigate the overall AMS performance of a processed sample. The quality factor, as a function of the chemical yield, for the three analyzed batches and the initial tests of the modified protocol are plotted in Fig. 4.10. All samples, with the exception of the two outliers, had reasonably high chemical yields and high quality factors. Excluding the outliers, the average chemical yields are $(69 \pm 5)\%$ and $(88 \pm 10)\%$ for the Rur river and concrete samples, respectively. Since the Rur river samples were processed using the modified protocol (see section 4.1), it is reasonable that the average chemical yield of these samples is lower than for soil samples processed with the newly developed protocol. The average quality factors for Rur river and concrete samples are high at $(90 \pm 5)\%$

and $(87 \pm 10)\%$, respectively. Therefore, the processed samples are performing very well during the AMS measurements, showing that the sample preparation, even the modified protocol, is working nicely.
One of the outliers is the residue sample from the initial tests of the modified protocol (pink data in Fig. 4.10), which is good because this sample should not contain any or only small amounts of Sr. The target performance of the test samples combined with the performance of the Rur river samples further indicate that the dedicated Ca removal does work and that only negligible amounts of Sr are lost using the modified protocol. The second outlier (black data in Fig. 4.10) is from the Rur river batch (2I, 56 - 92 cm). The lack of performance is attributable to the failed sample preparation and was discussed in detail in section 4.3 and subsection 4.3.1.

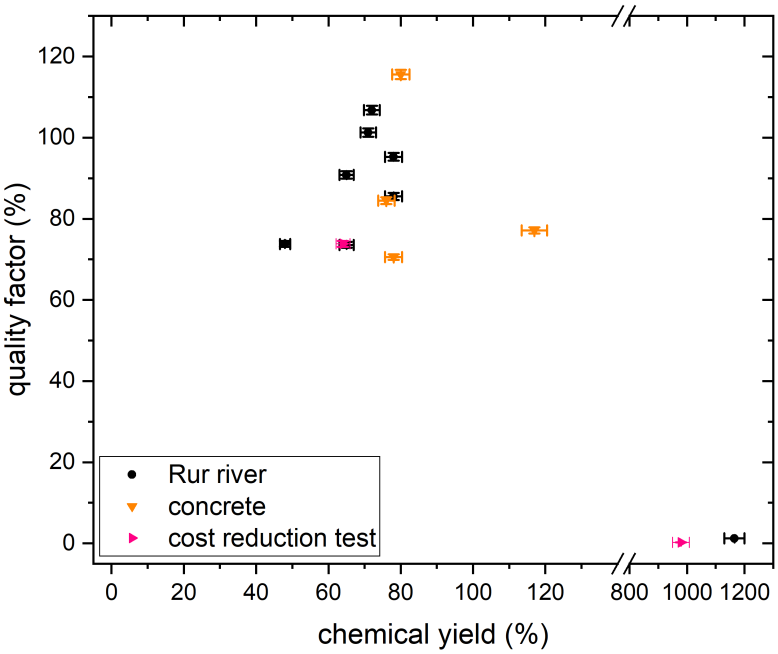

Figure 4.10.: Gravimetric chemical yield against the quality factor by AMS for all analyzed samples, including the initial tests of the modified protocol. Excluding the two outliers, all samples provided reasonably high average chemical yields around 69% and 88% for the Rur river and concrete samples, respectively. Their average quality factors are $> 85\%$. This highlights that the sample preparation does work well and produces good quality AMS targets. Note that the there is a linebreak on the x-axis to show the two outliers.

5. Development of an ion-laser assisted AMS measurement routine for ^{90}Sr at CologneAMS

For the development of the ion-laser-interaction assisted accelerator mass spectrometry (AMS) measurement routine at the 6 MV accelerator of CologneAMS, a lot of infrastructure had to be built and tested. This chapter discusses various processes involved in the development of a ^{90}Sr measurement routine, as well as the first conducted full AMS measurements with blank, standard and, Zr-spiked blank samples to determine the current status of the setup, e.g., blank level, isobar suppression and detection efficiency. To avoid confusion, all mentioned dates of this chapter are in the format of DD.MM.YYYY.

5.1. Setting up the ion source and ion source performance

This section contains a summary of all simulations and measurements that were performed with the Anion Laser Isobar Separator (ALIS) ion source at the 6 MV accelerator of CologneAMS.

5.1.1. Positioning of the ion source

To position the ion source of the ALIS setup (see Fig. 1.7), simulations of the ion beam were carried out using the ion source geometry. The software of choice for these simulations was Simion [96]. After drawing the ion source with Fusion 360

[108], a CAD (computer aided design) software, the drawing can be imported into Simion. When importing 3D drawings into Simion, the grid size, i.e., the size of the cubes used to divide the drawing, must be selected before solving the Laplace equations for every imported object. The grid size is measured in units of mm/grid unit (gu). By selecting large grid sizes, round objects will become angular, i.e, that the imported geometry is no longer faithfully representing the original design. As a consequence, the calculated electric fields will deviate from the expected field, based on the original geometry. Thus, particles will have erroneous trajectories within the simulation. However, selecting an extremely small grid size is not optimal either, as it significantly increases the computing time required for the simulations. To determine a grid size that will produce credible results a few test simulations have been performed with different grid sizes. Three grid sizes were tested: 1 mm/gu, 0.5 mm/gu, and 0.25 mm/gu. These sizes were selected to simulate 2000 particles of mass 145 amu with singular negative charge, generated in a gaussian distribution. The simulated beam positions in x and y direction can are shown in Fig. 5.1. Using a grid size of 1 mm/gu (see Fig. 5.1a) results in a distorted ion beam, especially in the y direction. This observation indicates that the grid size is too large and the generated electric fields are not radially-symmetric as they should be. Therefore, a smaller grid size of 0.5 mm/gu was tested, which can be seen in Fig. 5.1b. The beam position appears to be reasonable given the selected settings, and there is no observable difference in the trajectories of the particles in x or y direction. The same simulation was repeated with an even smaller grid size of 0.25 mm/gu. However, there is no significant difference between the simulation results using a grid size of 0.5 mm/gu or 0.25 mm/gu. Hence, the grid size of 0.5 mm/gu was chosen for further simulations to reduce computing time.

Two different options were available to position the ion source in front of the double focusing 90° bending magnet. One option is to have a beam waist in front of the bending magnet, allowing for waist to waist mapping of the magnet. For the symmetric 1:1 (point to point) mapping at precisely twice the bending radius (ρ) in front and behind the magnet, the condition $\beta_{\text{eff}} = \beta$ must be met, where β is the magnetic edge angle, i.e., angle between the ion path and the magnet field edge [94, 109]. A sketch showing this relation is shown in Fig. 5.2. The second option is to have no beam waist in front of the magnet. In this case, the ion source is closer

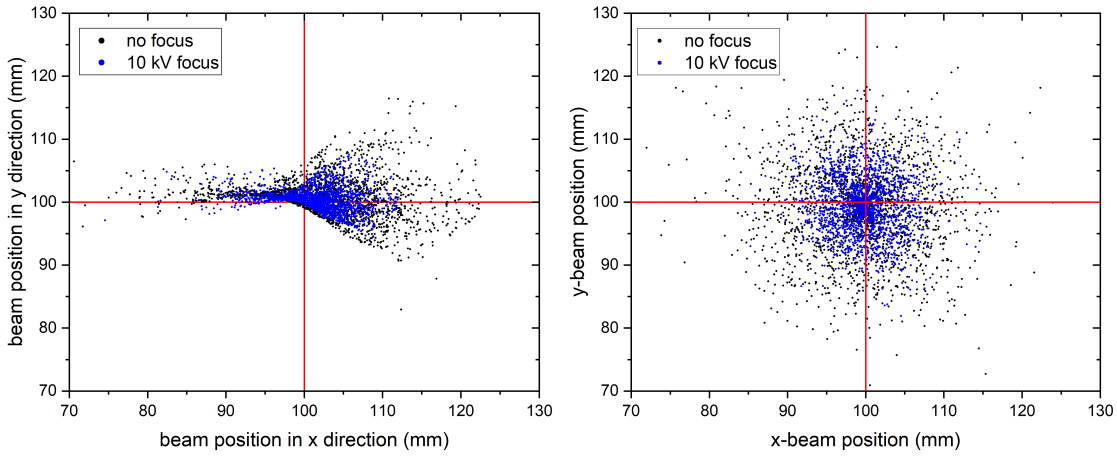

(a) 1mm/gu **(b)** 0.5mm/gu

Figure 5.1.: Comparison of the simulated ion beam position in x and y direction shortly after the ion source extraction using Simion [96] for two different grid sizes, with and without applied potential to the einzel lens of the ion source to focus the ion beam. (a) Simulated ion beam position using a grid size of 1 mm/gu. The ion beam is strongly distorted, especially in the y direction, showing that this grid size will not produce credible results. (b) Simulated ion beam position using a grid size of 0.5 mm/gu. Decreasing the grid size resulted in a reasonable and radially-symmetric distribution of the beam position. Note that the red lines indicate the middle position of the used coordinate system.

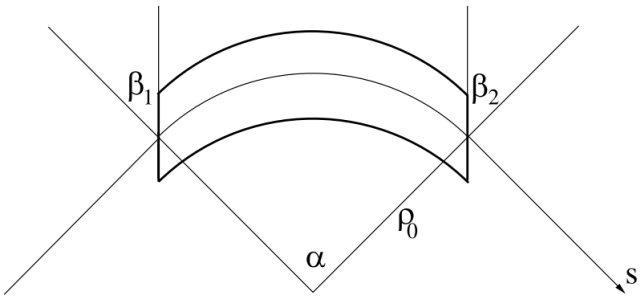

Figure 5.2.: Sketch showing a bending magnet with deflection angle α, bending radius ρ_0, ion trajectory s, and the magnetic edge angle and the ion path β. Picture was taken from [109].

to the magnet, thus rendering waist to waist mapping impossible. However, this can be corrected with the einzel lens of the ion source. Following the extraction of the ion beam from the ion source, the beam drifts in vacuum. By measuring the

phase space ellipse at a selected distance after the extraction, e.g., 900 mm after the extraction, one can calculate the virtual beam waist, i.e., the waist position assuming a constant drift in vacuum. By adjusting the beam focus with the einzel lens, the position of the virtual beam waist changes and can be recalculated. Therefore, it is possible to identify an ion source position in conjunction with the einzel lens potential such that the virtual waist is at the required position to allow for waist to waist mapping. A sketch of the ion source and selected components of the subsequent beam line with known distances are shown in Fig. 5.3. The ion beam is generated in the middle of the target holder, which corresponds to a position of 1.5 mm in z direction of the simulations coordinate system. The known parameters of the magnet are the bending radius (ρ = 500 mm), the magnetic edge angle (β = 30.6°), and the pole shoe gap (g = 70 mm) of the magnet. The distances l_1 and l_2 (see Fig. 5.3) are unknown and must be calculated.

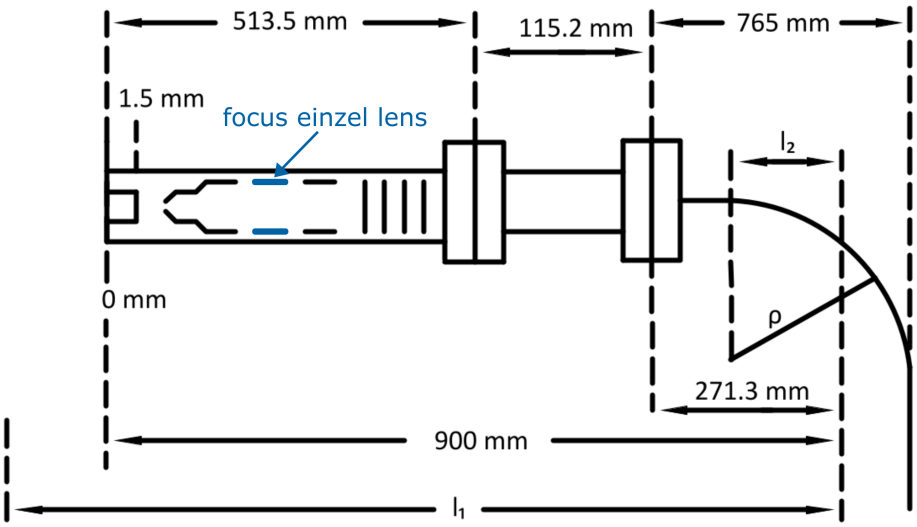

Figure 5.3.: Sketch of the ion source and selected components of the subsequent beam line with the corresponding distances in the simulations coordinate system. These values in conjunction with the simulations of the virtual beam waist are used to ensure waist to waist mapping of the bending magnet. Note that the 900 mm was the distance at which the phase space ellipse of the ion source simulations was obtained.

The required drift length (L) for waist to waist mapping of the magnet in x direction can be calculated with the formula [94, 109, 110]

$$L = \frac{\rho}{1 - tan(\beta)} = 1.022\,\mathrm{m} \tag{5.1}$$

Therefore, l_1 and l_2 must satisfy the relation

$$L = l_1 - l_2 \tag{5.2}$$

to achieve waist to waist mapping for the x direction. The parameter l_2 can be calculated by

$$l_2 = \rho - (765\,\mathrm{mm} - 271.3\,\mathrm{mm}) = 6.3\,\mathrm{mm} \tag{5.3}$$

By substitution of the obtained value of l_2 into eq. 5.2, one arrives at $l_1 = 1028.3\,\mathrm{mm}$. Repeating the simulation with different voltages of the einzel lens and calculating the position of the virtual waist allows for the data to be represented in a plot of the waist position as a function of the voltage of the einzel lens. This method can be used to estimate the required voltage of the power supply. The results of these simulations are shown in Fig. 5.4. A slight but visible difference in the x and y direction is observable, which is most likely still an artifact stemming from the selected grid size. However, the small differences are negligible. The requirements of the power supply for the x direction is approximately $-7\,\mathrm{kV}$ to fulfill the condition of equation 5.2. Hence, the ion source was positioned accordingly to the magnet to allow for waist to waist mapping without the necessity of a beam waist in front of it.

The y direction has the parameter β_{eff} and for the special case of $\beta_{\mathrm{eff}} = \beta$ the drift drift length is identical in both directions. It can be calculated by the formula

$$tan(\beta_{\mathrm{eff}}) = tan(\beta) - \frac{g}{\rho}\,\frac{1 + sin^2(\beta)}{cos^3(\beta)}\,K \tag{5.4}$$

where g is the pole shoe gap, K is the form of the pole shoe, β is the magnet edge angle, and ρ is the bending radius [109]. The pole shoe form of the bending magnet have a Rogowski form, resulting in a K value of $K, \approx 0.7$ [109]. From eq. 5.4, it can be deduced that $\beta_{\mathrm{eff}} < \beta$. Consequently the beam waist position in the y direction is closer to the magnet exit than the x direction.

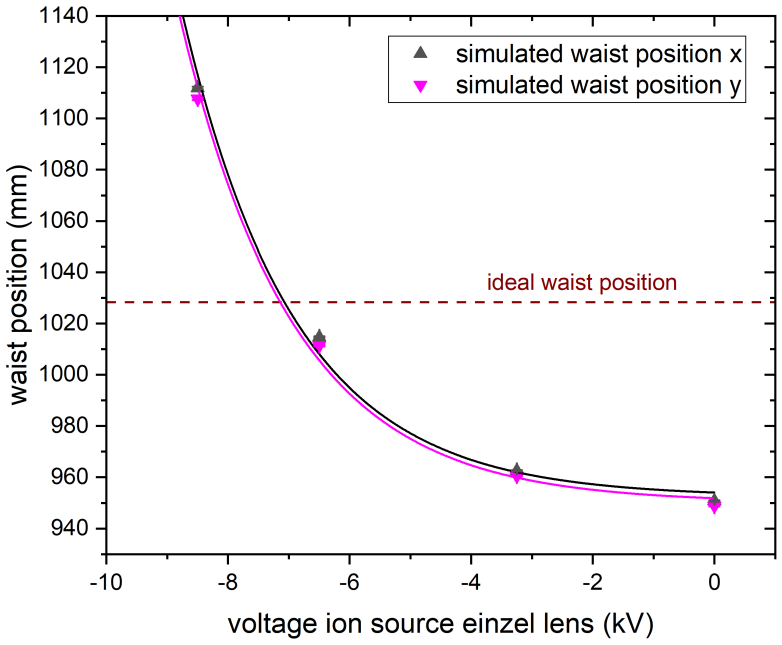

Figure 5.4.: Simulated waist position plotted against the applied voltage of the focusing einzel lens of the ion source for x and y direction. The waist to voltage behavior was fitted for both spatial directions. At $l_1 = 1028.3\,\text{mm}$ the intersection of the horizontal line (brown) with the fit of the x direction (black) indicates the required einzel lens voltage for a waist to waist mapping of the bending magnet. Note that the simulated x and y data points shown do have uncertainties which are not visible.

5.1.2. SrF_3^- and ZrF_3^- molecule formation in the ion source

According to the existing literature, the most effective method for AMS measurements of ^{90}Sr involves the extraction of the prolific anion molecule SrF_3^- [31, 53, 92, 97, 111]. Since every SNICS ion source performs slightly differently in terms of molecule formation, the SrF_3^- and ZrF_3^- molecule formation with the 134-MC-SNICS ion source was investigated as well. For this purpose, the samples were mixed with commercially available SrF_2 powder (Alfa Aesar) and PbF_2 powder (Alfa Aesar) in a ratio of SrF_2:PbF_2 (1:8) and ZrF_4:PbF_2 (1:1) by weight. As the stable isotopes ^{88}Sr and ^{90}Zr are by far the most abundant isotopes with natural abundances of 82.58% and 51.45%, respectively, the molecule formation of the fluoride molecules was determined via these two isotopes.

A large mass scan ranging from 30 A to 60 A, corresponding to approximately 50 amu to 210 amu, was performed to examine the formation of Sr^- and all poten-

tial SrF_x^- molecules up to SrF_6^- (202 amu). The ion current of the mass scan was measured in a Faraday Cup (FC) just behind the bending magnet after the ion source (see Fig. 1.7). To ensure adequate mass resolution for the mass scan, the slits in front of the FC were set to ± 1 mm, which corresponds to an aperture of 2 mm. Prior to the determination of the molecule formation, the mass scan was calibrated via easily identifiable and abundantly produced molecules, e.g., $^{88}SrF_x^-$, $^{x}Cu_x^-$, $^{x}CuF_x^-$ and $^{133}CsF_2^-$. An excerpt of the significant mass region, ranging from 80 amu to 200 amu, as determined by a calibrated mass scan, is shown in Fig. 5.5.

Subsequent to the calibration of the mass scan, the molecule formation for $^{88}Sr^-$ and $^{88}SrF_x^-$ molecules was determined with respect to the sum of the ion current output of all produced molecules and the atomic ion current. In other words, it is given as a percentage of the integrated ion current of the atomic anion and the fluoride molecules of that element and isotope. Since the targets are pressed in Cu cathodes (see section 3.5), potential mass interferences may occur at masses 126 amu ($^{88}SrF_2^-$) and 145 amu ($^{88}SrF_3^-$). These interferences originate from the molecules $^{63}Cu_2^-$ and $^{63}Cu_2F^-$, respectively. Hence, the measured ion currents

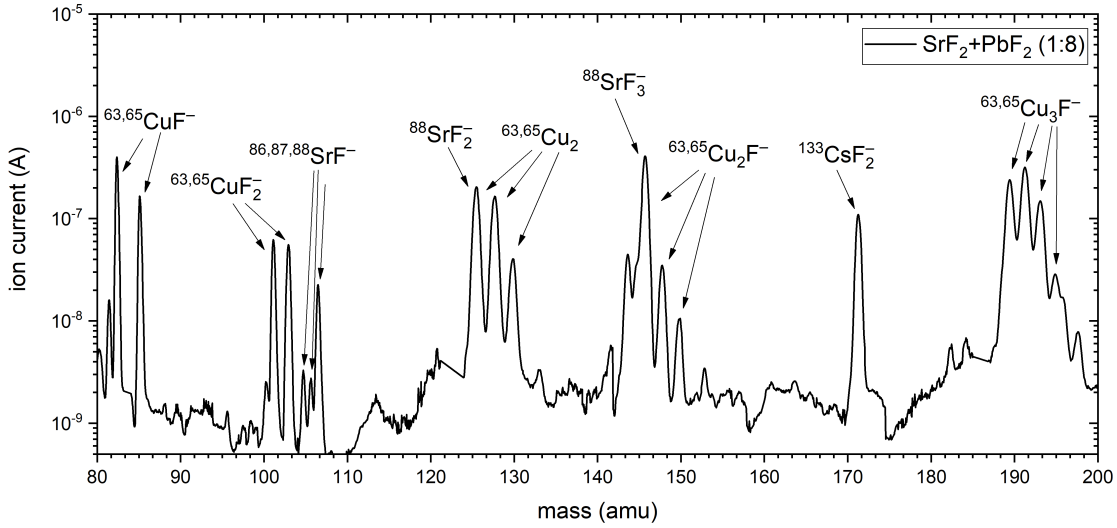

Figure 5.5.: Example of a calibrated mass scan from 80 amu to 200 amu of a Sr target mixed with a 1:8 (SrF_2:PbF_2) ratio by weight. The measurement was performed with narrow slits at ± 1 mm. All important molecules that were produced in the shown range are labeled accordingly.

must undergo a correction. The ion current of the interfering Cu molecules can be calculated via the natural occurring ratio of the other Cu molecules with different isotopes, i.e., $^{63}Cu^{65}Cu$ and $^{65}Cu_2$ for $^{63}Cu_2^-$. Therefore, the surplus of the measured ion current originating from Cu interferences can be subtracted to obtain the correct ion current of $^{88}SrF_x^-$. The molecule formation results for $^{88}SrF_x^-$ are shown in Fig.5.6 (a). They demonstrate that $^{88}SrF_3^-$ is indeed the most prolific anion produced in the sputter source, accounting for 90% of the total ion current. The remaining two molecules, $^{88}SrF^-$ and $^{88}SrF_2^-$, each account for approximately 5% of the ion current. The atomic anion $^{88}Sr^-$ does not form negative ions above 500 pA, below which the reading of the FC becomes unreliable due to the used current amplifier (Keithley Picoammeter 6485). Nonetheless, even formation at a few hundred pA, the impact on the results would be negligible. The result is consistent with the literature for fluoride formation in SNICS ion sources when mixing sample material with PbF_2 powder [111].
An identical evaluation was conducted for the isobar ^{90}Zr on a ZrF_2:PbF_2 (1:1) target, and the results are shown in Fig. 5.6 (b). In contrast to $^{88}SrF_3^-$, the formation of $^{90}ZrF_3^-$ is below 500 pA, thus only an upper limit of the molecule formation of $^{90}ZrF_3^-$ can be given with $< 0{,}25\%$. Other fluoride molecules, e.g., $^{90}ZrF_5^-$ and $^{90}ZrF_2^-$, are produced at significantly higher rates, reaching 56% and 18%, respectively. The measured ZrF_x^- molecule formation deviates significantly from the published values by Zhao et al. 2010 [111], where ZrF_5^- should be produced almost exclusively. However, the observed trend that ZrF_5^- is the most prolific molecule is consistent with the results of this study. Furthermore, the molecule formations of SrF_x^- and ZrF_x^- are both also comparable to the measurements performed at VERA [92].

5.1.3. Ionization yield of SrF_3^-

The ionization yield of a specific anion is an important parameter of an ion source. It is defined as the fraction of an anion of a specific mass that is formed and can be extracted from the ion source, compared to the losses due to no anion formation or anion formation of different masses. In the case of Sr, the extracted anionic molecule is SrF_3^-. However, as demonstrated by the mass scans, SrF^- and SrF_2^-

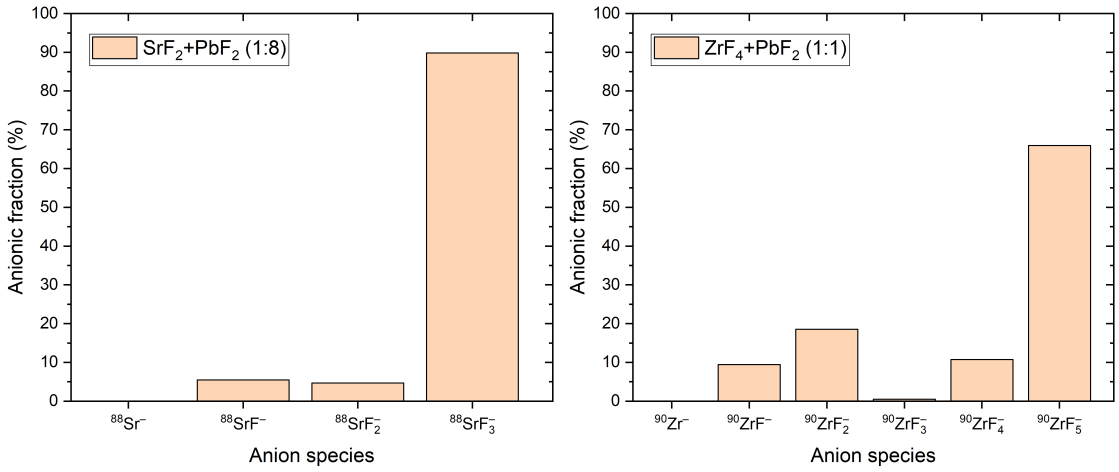

Figure 5.6.: Anion formation in the ion source for (a) $^{88}Sr^-$ and $^{88}SrF_x^-$ and (b) $^{90}Zr^-$ and $^{90}ZrF_x^-$. Empty columns correspond to either no molecule formation or production below 500 pA, for which the reading of the FC becomes unreliable due to the used current amplifier. The diagrams are normalized to the total current output of all detected anions represented in the diagrams, i.e., they are given as a percentage of the integrated ion current from the atomic anion and the fluoride molecules of that element and isotope. Note that the shown results are mass interference corrected, i.e., that the ion current of interfering copper molecules have been subtracted.

(see Fig. 5.6 (a)), are also produced. Consequently, Sr atoms that do not form SrF_3^- are lost during a measurement.

To measure the ionization yield of SrF_3^-, two parameters must be determined. These are the precise SrF_2:PbF_2 mixture ratio used for the targets and the mass of the sample material inside the target holder. With these two parameters, the number of Sr atoms ($N_{^{88}Sr}$) in the target can be calculated and subsequently compared with the measured $^{88}SrF_3^-$ ion current ($I_{SrF_3^-}$) after extraction from the ion source and measured behind the 90° magnet acting as a p/q-filter. Subsequent to sputtering the target to exhaustion, the ratio of the ^{88}Sr atoms that produce the measured $^{88}SrF_3^-$ ion current divided by the theoretical maximum number of $^{88}SrF_3^-$ that could be measured due to the number of Sr atoms in the target yields the ionization yield ($Y_{SrF_3^-}$).

This relation is also illustrated in the following equation

$$Y_{^{88}SrF_3^-} = \frac{I_{SrF_3^-}}{e \cdot N_{^{88}Sr}} \tag{5.5}$$

where e denotes the elementary charge. Unfortunately, the ionization yield measurements for $^{88}SrF_3^-$ could not be conducted at the ALIS setup yet. This is attributable to the fact that installation of such a large addition to the beamline of the 6 MV accelerator of CologneAMS took significantly more time than initially anticipated. Hence, the priority of measuring the ionization yield was shifted in favor of more important measurements, such as the first full AMS measurements (see section5.2 and 5.3). This measurement will be conducted in the near future and the samples for the ionization yield measurement have already been pressed. Nonetheless, the $^{88}SrF_3^-$ ionization yield with a similar ion source, a 40-MC-SNICS compared to the 134-MC-SNICS, was measured with the ILIAMS setup at VERA and yielded an ionization efficiency of approximately 1% [92]. Since both ion sources are produced by NEC and are of a similar type, it is expected that the ionization yield should be similar. However, without a measurement this can not be guaranteed, as ionization yields can differ significantly at different facilities, even if they are of the same type. Since the ionization yield is necessary to calculate the overall ^{90}Sr measurement efficiency (see section 5.2.6), the ionization yield at ALIS has to be estimated for the time being. Thus, the $^{88}SrF_3^-$ ionization yield at the ALIS setup is estimated conservatively with 0.5%. This estimate seems to be a realistic one, given the experience that was gained throughout the experiments conducted at ALIS so far.

5.2. AMS measurements and performances

This section contains the most important results regarding the performance during AMS measurements of ^{90}Sr at CologneAMS, such as the different transmission through the facility, e.g., ion cooler and accelerator, isobar suppression of ^{90}Zr and an estimation of the current detection efficiency.

5.2.1. AMS measurement routine at CologneAMS

The measurement routine for ^{90}Sr at the 6 MV accelerator of CologneAMS is very similar to the measurement routine at VERA using ILIAMS, as described in section 3.1. Therefore, only the most essential aspects of the measurement routine will be addressed. A schematic drawing illustrating the current measurement routine is shown in Fig. 5.7. It includes the selected molecules injected into the ion cooler and accelerator, the selected charge state on the high-energy side, the location of the offset FC (OFC) for the $^{88}Sr^{3+}$ ion current measurement on the high-energy side, and the location of the detector that was used for the $^{90}Sr^{3+}$ detection.

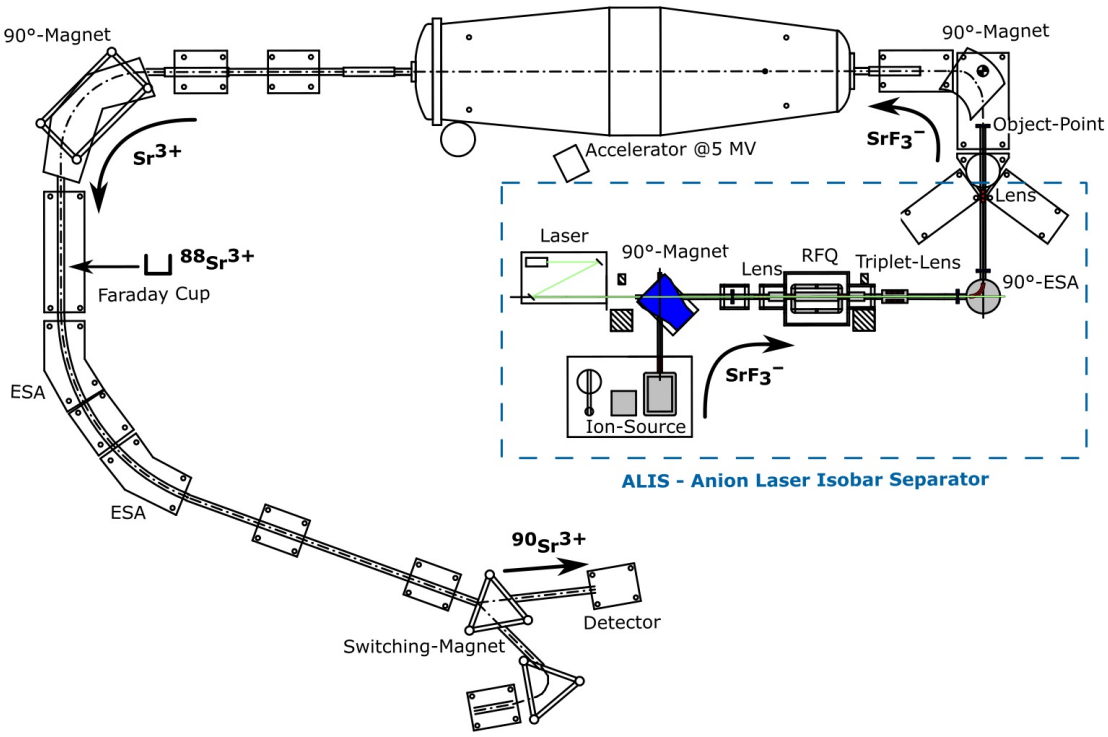

Figure 5.7.: Schematic drawing of the 6 MV AMS facility of CologneAMS, including the new ALIS setup. It illustrates the ^{90}Sr measurement routine by showing the molecules injected into the ion cooler and accelerator, the selected charge state on the high-energy side, the location of the offset FC for the $^{88}Sr^{3+}$ measurement, and the detector position for the $^{90}Sr^{3+}$ detection. Note that this is a modified version of the 6 MV facility at CologneAMS, which was provided by Markus Schiffer.

The the most prolific fluoride molecule, SrF_3^- (see section 5.1.3), is extracted from a 134 sample MC-SNICS ion source with 23.5 keV of energy. Following the ion source, a 90° bending magnet is used as a first p/q filter before the ion cooler. The anions are electrostatically decelerated prior to the injection into the gas-filled RFQ ion cooler. The used buffer gas within the ion cooler is pure He. Inside the RFQ ion cooler, the ion beam is collinearly overlapped with a 532 nm (2.33 eV, 18 W) laser beam to neutralize the isobaric molecule ZrF_3^- via element-selective laser photodetachment. Depending on the buffer gas pressure, the current $^{90}ZrF_3^-$ suppression ranges from a factor of 80 - 300 (see section 5.2.2.2). At the extraction of the ion cooler, the anions are reaccelerated to 23.5 keV. Subsequently, a 90° ESA filters them based on their E/q ratio. Following the ESA, a 90° bending magnet injects a selected m/q ratio into the accelerator operated at 5 MV and using Ar as a stripper gas. Despite the potential enhancement in accelerator transmission with He as the stripper gas when injecting SrF_3^- [31, 97], Ar is used. This is due to the fact that currently, the stripper gas can not be changed at the 6 MV accelerator of CologneAMS. On the high-energy side, the 3+ charge state is selected, and the Sr^{3+} ions exit the accelerator with an energy of approximately 18 MeV. Following the a 90° bending magnet on the high-energy side, the stable $^{88}Sr^{3+}$ is measured in an OFC. Subsequently, the m/q ratio for $^{90}Sr^{3+}$ is filtered by an ESA, which is split into two short ESA segments (see Fig. 5.7). Finally, a switcher magnet deflects the $^{90}Sr^{3+}$ by around 30° into the detector, which is a four-anode gas ionization chamber (GIC). The 3+ charge state was chosen for the measurements, despite its lower charge state yield compared to the 2+ charge state (see section 5.2.4). This is due to the inability to deflect the $^{90}Sr^{2+}$ ions, which exit the accelerator with an energy of 13.1 MeV, into the detector using the switching magnet. Events are only registered if incoming ions deposit energy on all four anodes of the GIC, otherwise they are discarded. Potential modifications to the described measurement routine, such as adjustments to the terminal voltage, selected charge state, or buffer gas pressure, might be applied in the future to further improve the measurement efficiency.

5.2.2. Isobar suppression

5.2.2.1. Isobar suppression in the ion source

The extraction of the molecule SrF_3^- already results in the suppression of the abundant isobar ^{90}Zr in the ion source due to the low formation of ZrF_3^- molecules compared to SrF_3^- (see also subsection 5.1.2). In our case, SrF_3^- is produced almost exclusively in the ion source at 90%, in comparison to the fluoride molecules SrF_2^- and SrF^-. Furthermore, the ZrF_3^- formation is very poor compared to the formation of the most prolific anion ZrF_5^- at 65%. The production of ZrF_3^- is less than 500 pA, at which the FC reading becomes unreliable. Consequently, only an upper limit of $< 0.25\%$ for the formation of ZrF_3^- with respect to the integrated ion current of all ZrF_x^- molecules can be determined. Therefore, the formation of ZrF_3^- with respect to SrF_3^- in the ion source yields an isobar suppression of $< 2.8 \cdot 10^{-3}$. This is consistent with the published value of $3 \cdot 10^{-5}$ for the same molecules at the AMS facility in Ottawa [32] and is compatible with measurements performed at VERA of $< 10^{-3}$ [92, 97].

5.2.2.2. Isobar suppression with ALIS

At VERA, the isobar suppression capabilities for ^{90}Zr inside a gas-filled RFQ ion cooler have already been investigated. It was demonstrated that suppression factors on the order of $> 10^7$ are achievable with a 532 nm laser [31, 97]. Since the ALIS setup presently experiences significant ion beam losses during the injection into the ion cooler at higher buffer gas pressures of > 1.5 Pa (see section 2.4), the extent of isobar suppression achievable under optimal conditions of $^{90}ZrF_3^-$ in the ion cooler remains undetermined. In addition, the isobar suppression with a $He+O_2$ mixture (30:1) as buffer gas, instead of pure He, has also not been studied yet. However, this will be investigated as soon as the challenge of the injection has been solved. For the time being, only the ^{90}Zr suppression with He as a buffer gas at 1.06 Pa and 1.7 Pa were investigated and measured, respectively. A picture of the current laser table setup, which is still very minmalistic setup and is used for the suppression tests and the first AMS measurements, is shown in Fig. 5.8. At present, there is no dedicated lens system in place to change the focus of the laser beam. The implementation of such a lens system in the future could potentially maximize the overlap of the ion beam and the laser beam.

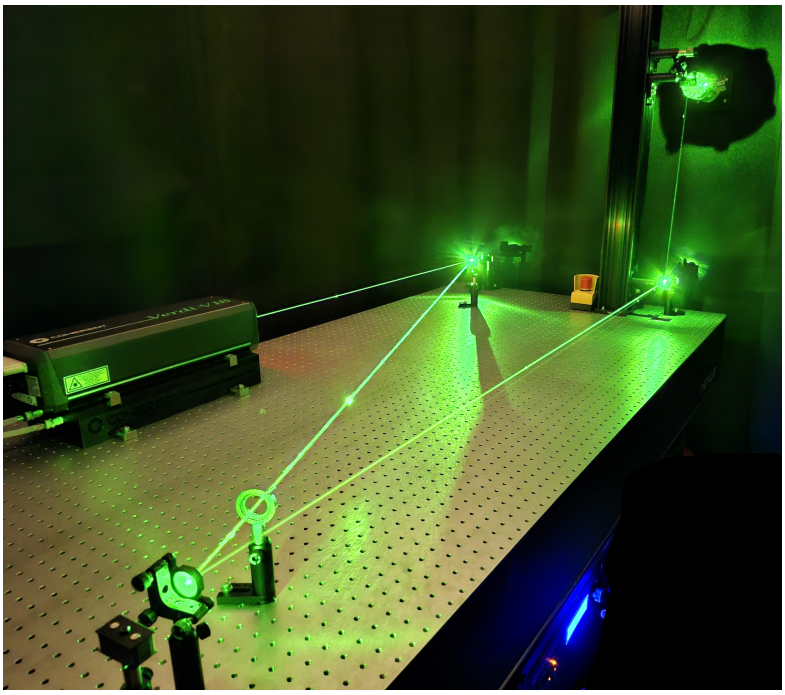

Figure 5.8.: The minimalistic laser setup for the 532 nm laser at the ALIS setup of CologneAMS. It shows the first setup, with only 4 mirrors used to guide the laser beam into the beamline and through the ion cooler for the first suppression tests and AMS measurements of ^{90}Sr. As of now no lens system for focusing is implemented. Nonetheless, the implementation of a dedicated lens system might be added in the future to maximize the overlap between the ion beam and the laser beam. The laser output in this picture is around 1 W.

To determine the isobar suppression of the ALIS ion cooler, the ion beam is guided through the facility into a split-anode GIC at the end of the high-energy beam line. For this measurement, the four-anodes GIC detector was used (see Fig. 5.7), where signals are only registered when ions deposit a signal on all four of the anodes, respectively. Afterwards, the count rate of $^{90}Zr^{3+}$ is measured in the detector, once with the 532 nm laser and once without the laser. This setup allows for the measurement and calculation of the suppression factor. The detector signal of a Zr-spiked AMS target with the laser switched on and off at a buffer gas pressure of 1.06 Pa is shown in Fig. 5.9.

At low buffer gas pressures around 1.06 Pa and approximately 6 W of laser power through the ion cooler, the suppression of $^{90}Zr^{3+}$ is rather low at 80, which is shown

in Fig. 5.9. Ion cooler simulations conducted at VERA revealed that the pressure inside the ILIAMS ion cooler has a maximum at the center, where the gas inlet is located, and subsequently declines in magnitude towards both ends. In typical conditions during Sr measurements, an average buffer gas pressure of 3.34 Pa and a peak pressure of 7.10 Pa are present inside the ion cooler[112]. This is at least a factor of 3 larger than the pressure inside the ALIS cooler when optimizing for transmission through the ion cooler (see section 5.2.3) due to the injection losses at higher pressures. From the test bench measurements at Vienna, the median ion residence time at 1.06 Pa can be estimated to be around 1 ms (see Fig. 2.6) with 60 nA in the FC prior the ion cooler injection. It has been established through experimental observations at VERA that the ion residence time varies significantly depending magnitude of the injected ion current [28]. The injection losses at ALIS can only be estimated. However, assuming ion beam losses of at least 50% (see

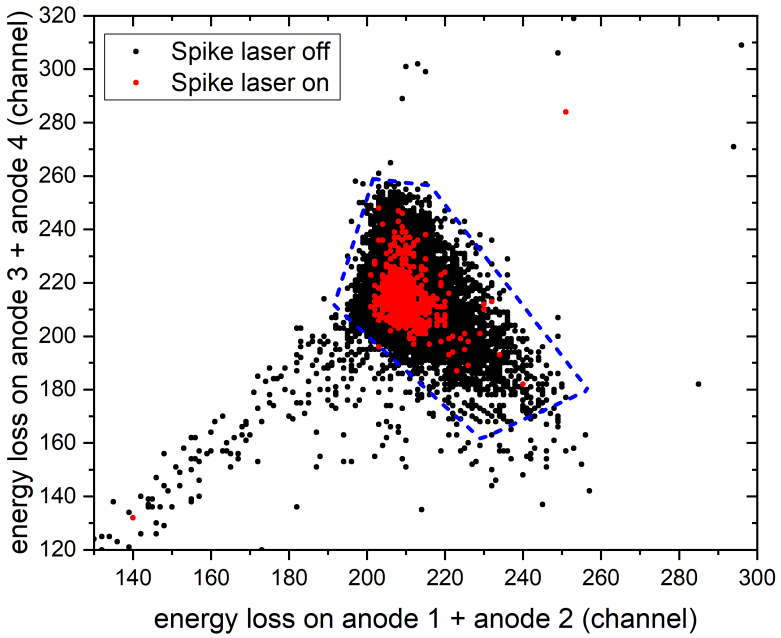

Figure 5.9.: Characteristic energy loss spectrum, displaying the energy loss on the third and fourth anode as a function of the energy loss on the first and second anode of the four-anode GIC, for a Zr-spiked AMS target. As long as the laser is deactivated (black), a significantly higher amount of $^{90}Zr^{3+}$ enters the detector compared to when the laser is activated (red). The He buffer gas pressure in this experiment was at 1.06 Pa and the Zr was suppressed by a factor of 80. Note that the blue box marks the ROI of $^{90}Zr^{3+}$.

section 2.4), when injecting 200 - 400 nA at 1.06 Pa, would result in 100 - 200 nA injected into the RFQ section of the ALIS ion cooler. The median ion residence time of the ILIAMS cooler for a 340 nA has been reported to be around 1.5 ms for an average buffer gas pressure approximately 3.34 Pa [28, 112]. Taking all factors into account, the median ion residence time during the tests under optimal ion cooler transmission settings is most likely < 1.0 ms. Hence, the ion residence time might be inadequate to achieve higher isobar suppression via laser photodetachment due to the short interaction time of the laser beam and the ion beam, combined with a low cross section for laser photodetachment.

In order to test this hypothesis, the buffer gas pressure was increased to 1.7 Pa, and the suppression factor was measured at the expense of an extremely low ion cooler transmission of only 6%. Two sample materials were measured to investigate the Zr suppression. One was a standard sample (Sr-11J), with a ^{90}Sr/Sr ratio on the order of 10^{-11} (see Tab. 5.2), and the other one was a machine blank sample (SrF_2+PbF_2). The results of these measurements are shown in Fig. 5.10. In fact, the isobar suppression increased with the higher buffer gas pressure up to $3.3 \cdot 10^2$. This correspond to an increase in Zr suppression by a factor of four, while simultaneously increasing the buffer gas pressure by 60%. This outcome aligns with the hypothesis that the ion residence time at low buffer gas pressures is inadequate to achieve high suppression factors of $\geq 10^5$ for $^{90}ZrF_3^-$. Since the residence time did not only increase due to the higher buffer gas pressure, but most likely also due to higher injection losses, it remains to be seen whether the suppression of Zr will change significantly at these pressures after solving the injection issues.

At present, the Zr suppression under ion cooler conditions with reasonable transmission is very low at 80. The low suppression factor, in conjunction with the low transmission through the ion cooler at low buffer gas pressures, currently prevents the possibility to efficiently measure ^{90}Sr samples with the ALIS setup. Nevertheless, further investigations to optimize the Zr suppression and thus improve the measurement of ^{90}Sr will be carried out in the future. This includes tests to improve the overlap of the laser beam and ion beam, as well as measurements at higher buffer gas pressures as soon as the challenge of the ion cooler injection is solved.

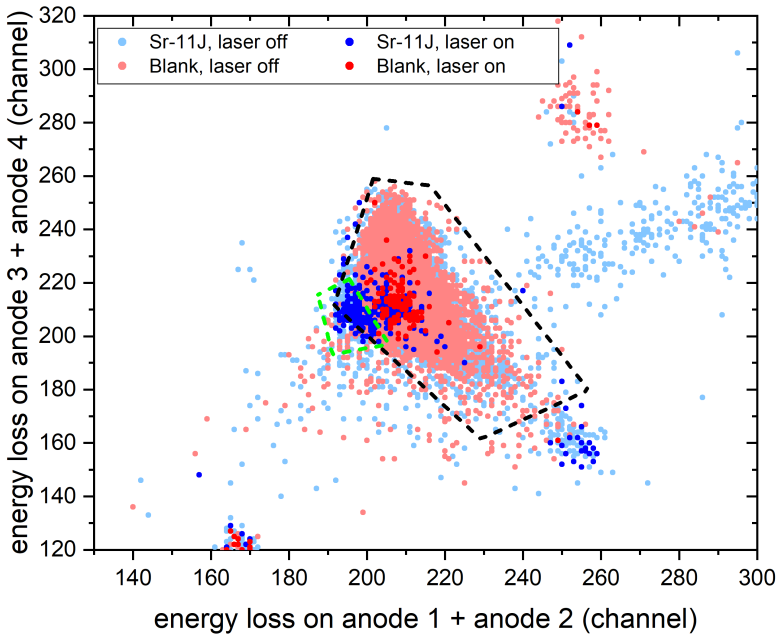

Figure 5.10.: Characteristic energy loss spectrum, displaying the energy loss on the third and fourth anode as a function of the energy loss on the first and second anode of a four-anode GIC, for a standard (blue) and a machine blank (red) sample with the laser switched on and switched off. When the laser is deactivated, the color of the data points is lighter in comparison to when the laser activated. The He buffer gas pressure for this experiment was at 1.7 Pa, and the $^{90}Zr^{3+}$ was suppressed by $3 \cdot 10^2$ for both targets. Note that the black box indicating the ROI for $^{90}Zr^{3+}$ is equivalent to the one in Fig. 5.9, while the light green box marks the ROI for $^{90}Sr^{3+}$.

5.2.2.3. Isobar suppression in the detector

Through the characteristic energy loss of charged particles in matter, additional isobar separation of $^{90}Zr^{3+}$ from $^{90}Sr^{3+}$ can be achieved using a split-anode GIC. The stopping power is proportional to the number of protons (Z), meaning that elements with higher Z have a larger stopping power and lose more energy in the first half of the detector compared to elements with lower Z. Hence, in a two dimensional energy loss spectrum of the four-anode GIC, where the energy loss on the third and fourth anode is plotted as a function of the energy loss on the first and second anode, the center of the $^{90}Sr^{3+}$ events and $^{90}Zr^{3+}$ events will be slightly separated when fully stopped in the detector. An example of such a two dimensional plot for $^{90}Sr^{3+}$ using the current setup and measurement routine is shown in Fig. 5.11.

In the case of Sr, it is particularly fortunate that Sr (Z = 38) is two protons lighter than Zr (Z = 40). Thus, the separation resulting from the different energy loss in the GIC will be larger than for adjacent isobars. Furthermore, compared to Sr, Zr looses more energy in the initial half of the detector than in the latter half. This should result in a slightly lower position on the y-axis in the energy loss spectrum. As illustrated in Fig. 5.11, at present this is not the case. The $^{90}Sr^{3+}$ events on the y-axis are at the same height as the $^{90}Zr^{3+}$, and on the x-axis, they display a slight shift to the left. This indicates that less energy is lost in the first half, but almost the same amount is lost in the second half. This is most likely attributable to the incomplete stoppage of $^{90}Zr^{3+}$ and $^{90}Sr^{3+}$ within the GIC using a detector pressure of only 8 mbar, as was done in these measurements. It would provides a possible explanation for the position of the $^{90}Sr^{3+}$ and $^{90}Zr^{3+}$ events in the energy

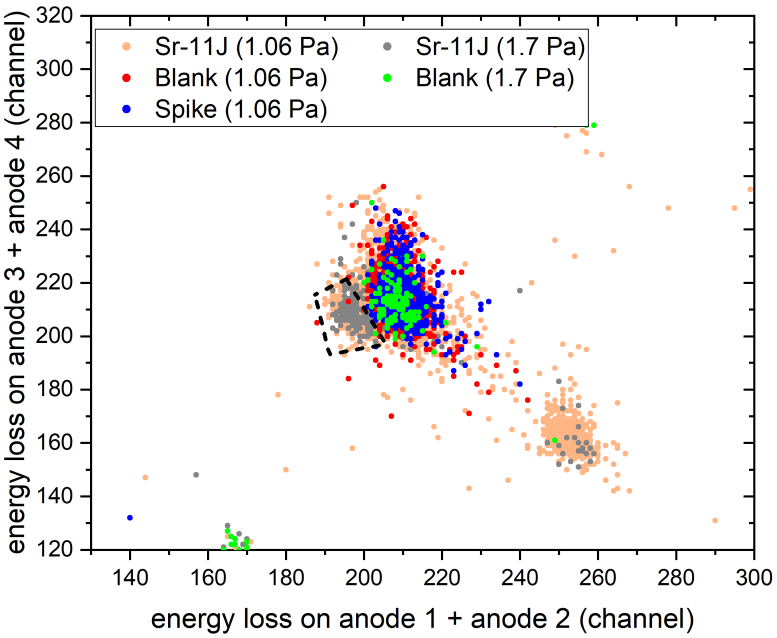

Figure 5.11.: Energy loss spectrum, displaying the energy loss on the third and fourth anode as a function of the energy loss on the first and second anode of the four-anode GIC, for a standard (Sr-11J), a machine blank and a Zr-spiked target at different buffer gas pressures. The ROI of $^{90}Sr^{3+}$ is represented by the a black box. The separation of $^{90}Sr^{3+}$ and $^{90}Zr^{3+}$ in the GIC is not well defined. Consequently, the ROI for $^{90}Sr^{3+}$ must be set very tight. Note that the GIC pressure was < 10 mbar, which might not be sufficient to fully stop $^{90}Sr^{3+}$ and/or $^{90}Zr^{3+}$. This would lead to a less pronounced separation in the GIC, and thus a worse isobar suppression in the detector.

loss spectra and the poorly defined separation in the detector compared to energy loss spectra at VERA, despite the significantly higher ion energies [92]. Under these conditions, the set region of interest (ROI) for $^{90}Sr^{3+}$ includes $>50\%$ of the ^{90}Sr events. Overall, the $^{90}Zr^{3+}$ suppression in the detector reaches up to 10^2.
It was not possible to conduct more AMS measurements using the ALIS setup. Hence, the optimization of the detector gas pressure for an improved $^{90}Sr^{3+}$ and $^{90}Zr^{3+}$ separation will be conducted in the near future. The optimization of the detector gas pressure should also result in an improved ROI for^{90}, thereby reducing the number of $^{90}Sr^{3+}$ events that are discarded due to a tightly set ROI.

5.2.2.4. Overall isobar suppression

The overall isobar suppression of ion-laser-interaction assisted AMS measurements at the 6 MV CologneAMS facility is the sum of all individual Zr suppression factors throughout the AMS facility. Considering the entirety, from the ion source to the GIC, the overall isobar suppression of ^{90}Zr is $>10^6$. This applies to AMS measurements with at He buffer gas pressure of 1.06 Pa, since AMS measurements ion cooler transmissions at higher buffer gas pressures are currently not feasible and buffer gas mixtures, e.g., He+O_2 (30:1), have not been tested yet. In comparison to the ILIAMS setup, which has an isobar suppression of $>10^{12}$, the Zr suppression at CologneAMS is significantly lower, at approximately half of the Zr suppression level. Nevertheless, there are still numerous improvements that can and must to be made to ALIS and the measurement routine. These improvements should significantly improve the overall Zr suppression capabilities of ALIS assisted AMS measurements. Some of these possible improvements include solving the injection losses, improving the laser and ion beam overlap, investigating the Zr suppression using a He+O_2 mixture as buffer gas, and the optimization of the detector gas pressure.

5.2.3. Ion cooler transmission

Based on the performance measurements conducted at the Vienna test bench setup, it has been determined that losses are occurring at the injection part of the ion cooler (see section 2.4). This limits the achievable cooler transmission and

the amount of buffer gas pressure that can be used. Approximately 30% transmission was achieved on the Vienna test bench for both $^{27}AlO^-$ and $^{63}Cu^-$ (see section 2.3). Due to issues with the ion source output, the ion cooler transmission at the test bench setup was only tested once for $^{88}SrF_3^-$. The test yielded an ion cooler transmission of approximately 16% before the sample material was depleted. The transmission through the ion cooler of $^{88}SrF_3^-$ was tested and optimized at the ALIS setup. The optimal cooler transmission was achieved with ion cooler settings at a radiofrequency of 1.5 MHz, a potential difference of 6.9 V on the guiding electrode structure, generating a guiding field strength of 6.23 V/m, a q value of 0.25 , and a low He buffer gas pressure of 1.06 Pa. The most important ion cooler parameters and values, which have been optimized for the ion cooler transmission of $^{88}SrF_3^-$ at ion energies of 23.5 keV, are listed in Tab. 5.1. The values presented in Tab. 5.1 correspond to the values of the power supplies of the respective parameter. In other words, the actual potential of the elliptic lenses and the aperture lenses is the potential difference between the high voltage (HV) of the ion cooler platform and the parameter itself. With these settings, ion cooler transmissions of 20 - 25% were achieved when injecting 50 - 400 nA of $^{88}SrF_3^-$. However, it is very probable that the transmission will be improved once the challenge of the injecting losses at higher buffer gas pressures has been successfully overcome. As a comparison, the transmission of $^{88}SrF_3^-$ at the ILIAMS setup of VERA is between 35 - 40% [31].

5.2.4. Accelerator transmission and charge state yield

The ALIS setup is connected to the beamline of the 6 MV Tandetron accelerator of CologneAMS. Hence, up to 6 MV could be used for the acceleration of Sr. In order to optimize the measurement efficiency, the transmission of the charge states 2+, 3+, 4+, and 5+ through the accelerator were investigated at terminal voltages of 3 - 5 MV, using Ar as the stripper gas. The charge state distribution of the Sr cations after the stripping process determines the transmission through the accelerator for a given charge state. The reason for the exclusion of the charge states 1+ is that the 1+ charge state could not be bend into the OFC with the high-energy analyzing magnet (see Fig. 5.7) and the 6+ charge state yield would be too low to reliably measure it in the OFC for most of the terminal voltages. Since the measurement

Table 5.1.: Table summarizing the important parameters of the ALIS ion cooler, optimized for $^{88}SrF_3^-$ transmission with ion energies of 23.5 keV. The guiding electrode value corresponds to the potential difference between the split surfaces of the electrode structure [91]. In contrast, the actual potential of the aperture lenses and elliptic lenses corresponds to the potential difference between the parameter and the HV of the ion cooler platform.

ion cooler parameter	**parameter/power supply value**
RFQ	1.5 MHz
buffer gas pressure	1.06 Pa
guding electrodes	6.9 V
HV	-23.47 kV
elliptic lens (injection)	689 V
elliptic lens (extraction)	858 V
aperture (injection)	77 V
aperture (extraction)	182 V

of ^{90}Sr at terminal voltages < 3 MV is not planned currently, the charge state yields for those terminal voltages remain to be investigated. Lastly, when the measurements were conducted, there was no time to condition the accelerator up to its maximum voltage of 6 MV. Hence, no charge state yield measurements were performed at 6 MV. The accelerator transmission ($T_{accelerator}$) was calculated as follows

$$T_{accelerator} = \frac{I_{FC,HE}}{q \cdot I_{FC,LE}} \tag{5.6}$$

where $I_{FC,LE}$ is the ion current measured in the FC on the low-energy side in front of the the accelerator, $I_{FC,HE}$ is the ion current measured in the OFC on the high-energy side, and q denotes the charge state of the cation.

The results of the accelerator transmission measurements are shown in Fig 5.12. The most prolific charge state is the 2+ charge state, yielding an accelerator transmission of approximately 30% for all tested terminal voltages. The second highest charge state produced is the 3+ charge state, yielding 11.1% transmission at 3 MV, 17.7% transmission at 4 MV, and 22.1% at 5 MV. The 4+ and 5+ charge states are both very low and increase with higher terminal voltages, reaching up to 7.2% for the 4+ and 2.4% for the 5+ charge state at 5 MV. The obtained results at a terminal voltage of 3 MV are similar to the charge state yield measurements performed

at VERA. At VERA, the charge state yields are 29.5%, 13.5%, and 3.3% and at CologneAMS they are 31.9%, 11.1%, and 2.2% for the charge states 2+, 3+, and 4+, respectively [92]. The measurements performed at VERA demonstrate that He as the stripper gas has the potential to increase the charge state yield for specific charge states, including the 3+ charge state. However, at CologneAMS, the stripper gas of the accelerator can not be changed. Since the 2+ charge state is by far the most prolific one, this would be the optimal charge state to measure ^{90}Sr. Unfortunately, the switcher magnet in front of the detector is not able to bend the Sr^{2+} into the detector (see section 5.2.1). Consequently, AMS measurements will be performed with the 3+ charge state. In the future, there is a possibility to mount a detector on a smaller deflection angle behind the switcher magnet, which could make measurements in the 2+ charge state feasible. It appears that the charge state yield for the 1+ charge state at all tested terminal voltages is very high ($\geq 30\%$), as all produced charge states should integrate to 100% transmission and the charge states $> 5+$ only add a few percent.

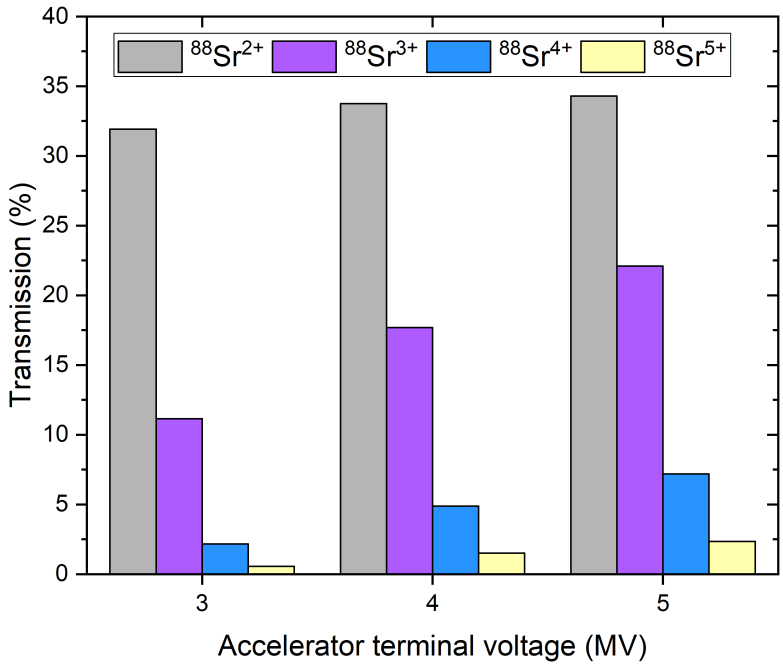

Figure 5.12.: Transmission through the accelerator for $^{88}Sr^{2+,3+,4+,5+}$ as a function of the terminal voltage of the accelerator using Ar as a stripper gas at the optimal pressure of approximately $2.0 \cdot 10^{-3}$ mbar. Note that the 1+ charge state could not be measured due to the analyzing magnet on the high-energy side and charge states of $> 5+$ were not measured due to their low yield.

In addition to the terminal voltage and the used stripper gas, the stripper gas pressure also has a significant effect on the transmission through the accelerator. Since it is currently impossible to change the stripper gas from Ar to He at the 6 Mv accelerator of CologneAMS, the effect of the stripper gas pressure on the transmission was investigated solely with Ar. The results of the transmission of $^{88}Sr^{2+}$ as a function of the stripper gas pressure at a terminal voltage of 3 MV is shown in Fig 5.13. The optimal transmission is at very low stripper gas pressures around $2.0 \cdot 10^{-3}$ mbar and decreases quite linearly towards higher stripper gas pressures. The initial measurement was started at a pressure of $1.5 \cdot 10^{-2}$ mbar. The pressure was then increased, until a significant downward trend was observed. Subsequently, the stripper gas pressure was reduced down to the minimal value of $5.0 \cdot 10^{-4}$ mbar, which is the minimum that can be controlled by the system. Thus, there is a second data point at $1.5 \cdot 10^{-2}$ mbar in Fig. 5.13.

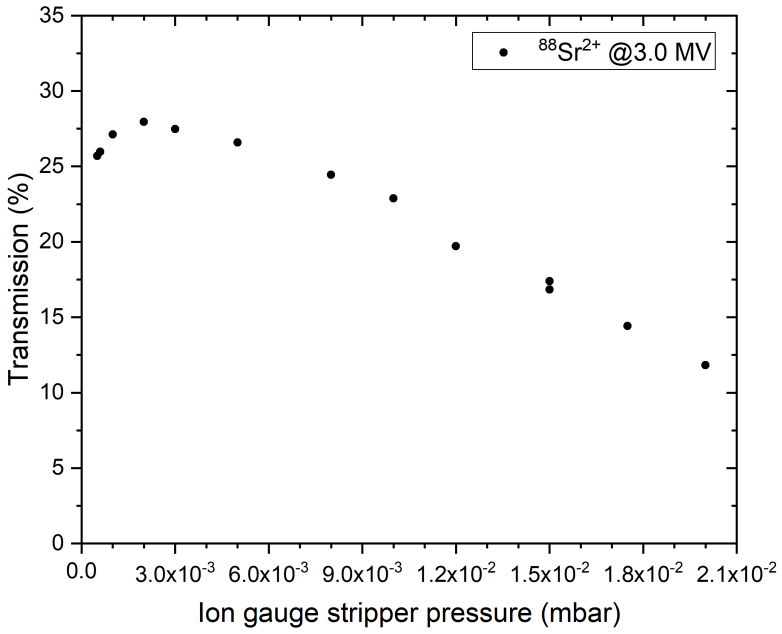

Figure 5.13.: Transmission of $^{88}Sr^{2+}$ through the accelerator at a terminal voltage of 3 MV as a function of the stripper gas pressure, using Ar as the stripper gas. The optimal stripper gas pressure is around $2.0 \cdot 10^{-3}$ mbar. The starting point of the measurement was at a pressure of $1.5 \cdot 10^{-2}$ mbar. Subsequent to an increase in the stripper gas pressure, a second data point is obtained at this pressure when the stripper pressure is reduced.

5.2.5. Transmission throughout the facility

AMS facilities are designed to ensure minimal ion beam losses throughout the beamline, corresponding to a transmission of 100%. However, specific components inherently restrict the transmission by design, e.g., the ion source, the ion cooler of the ALIS setup, and the accelerator in conjunction with the charge state selection. These components and their transmissions were discussed in the sections 5.1.3, 5.2.3, and 5.2.4, respectively. Apart from these three components, were larger losses are expected and minimized as much as possible, no significant losses are expected throughout the rest of the facility up to the detector for is well tuned and aligned system.

Due to limited time for the performed AMS measurements, it was not feasible to dedicate additional time to tuning and optimizing the transmission through the entire facility. Consequently, significant ion beam losses through the facility persist during the AMS measurement, especially on the low-energy side of the system. These low-energy side losses are attributable to the addition of the ALIS setup. The transmissions through the AMS facility between FCs is illustrated in Fig 5.14. The transmission on the high-energy side is satisfactory, as the transmission after the accelerator, excluding the charge state selection, is close to 100%. On the other hand, the low-energy side transmission between the ion cooler exit and the accelerator is rather low with 34%. The inclusion of the ion cooler transmission results in an overall low-energy side transmission of only 8.5%. The transmission through the facility is obtained by excluding both the ion cooler transmission and the accelerator transmission. In this case, the transmission is 33%. The determination of the overall transmission of Sr through the entire 6 MV AMS facility at CologneAMS yields an overall transmission of 1.8%.

In the future, additional time will be allocated towards optimizing the transmissions and investigating the necessity for changes to the recently added ALIS beamline. These modifications may include the addition of new steerers or lenses, with the aim to improve the transmission between the cooler exit and the accelerator.

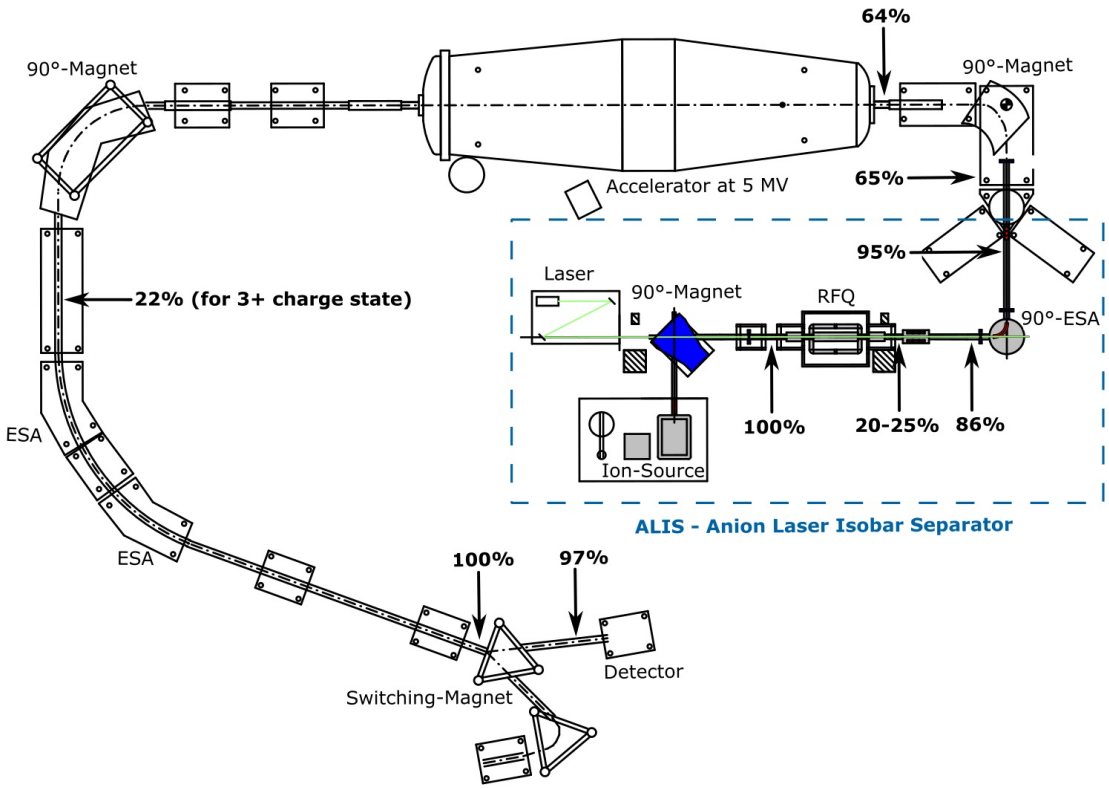

Figure 5.14.: Schematic drawing of the 6 MV AMS facility of CologneAMS, including the new ALIS setup. The transmission of the ion beam through the facility between each FC is indicated by the arrows and percentages in the drawing. In comparison to the nearly 100% transmission on the high-energy side of the system for the 3+ charge state, there is significant potential to improve the low-energy side transmission, as currently ion beam losses of approximately 66% persist. The first arrow shortly after the ion source refers to the transmission between the ion source and the first Faraday Cup. Note that this is a modified version of the 6 MV facility at CologneAMS, which was provided by Markus Schiffer.

5.2.6. Overall detection efficiency

The overall detection efficiency of ^{90}Sr is the number of the detected ^{90}Sr compared to the number of total ^{90}Sr atoms inside the measured target material. From the investigations at the 6 MV facility of CologneAMS, all losses of Sr throughout the AMS facility are known, and thus the overall detection efficiency for ^{90}Sr can be calculated. The estimated ionization yield is 0.5% (see section 5.1.3), the ion cooler transmission at a buffer gas pressure of 1.06 Pa is 20 - 25% (see section 5.2.3), the

accelerator transmission of the 3+ charge state at 5 MV is 22% (see section 5.2.4), the overall transmission through the facility after the ion cooler exit is 33% (see section 5.2.5), and finally the detector efficiency due to the set ROI in the GIC is $>50\%$ (see section 5.2.2.3). The resulting overall detection efficiency of ^{90}Sr is 0.045‰, which is approximately one order of magnitude lower than the detection efficiency at VERA [31].
The two most dominant factors that are limiting the current ^{90}Sr detection efficiency are the ion cooler injection issues and the low-energy side ion beam losses between the ion cooler extraction and the accelerator (see sections 2.4 and 5.2.5). By addressing these challenges, the detection efficiency will be significantly improved. In addition, the measurement of the ionization yield could also improve the detection efficiency, since the value of 0.5% is a conservative estimate (see section 5.1.3.

5.3. AMS results for ^{90}Sr

This section contains all the relevant information regarding the AMS measurement results, i.e., the standards that were used for the AMS measurements and the blank level. Since optimal ion cooler injection remains a challenge to overcome, the presented data reflects the current status and will most likely improve in the future.

5.3.1. Blank level

A very important quantity for AMS measurements is the machine blank level, because high machine blank levels strongly restrict the achievable abundance sensitivity, which is a key strengths of AMS. The conducted AMS measurements yielded an average blank ratio of $^{90}\mathrm{Sr/Sr} = (6.94 \pm 4.29) \cdot 10^{-13}$ for ion-laser-interaction assisted AMS measurements at the 6 MV facility of CologneAMS. The LoD was calculated using the formula

$$\mathrm{LoD} = \overline{\mathrm{x}}_{\mathrm{blank}} + 3\sigma_{\mathrm{blank}} \tag{5.7}$$

where $\overline{\mathrm{x}}_{\mathrm{blank}}$ denotes the average ^{90}Sr/Sr ratio of the blank and σ_{blank} denotes the uncertainty of the blank.

Therefore, the calculated LoD is $^{90}\mathrm{Sr}/\mathrm{Sr} = 1.98 \cdot 10^{-12}$, which corresponds to an activity of 11 mBq (2.19 fg) in a sample of around 1 mg of Sr. A sample containing 1 mg of Sr is equivalent to approximately 10^7 atoms of ^{90}Sr. When the ^{90}Sr detection efficiency of 0.045‰ is taken into account, approximately 66 ^{90}Sr atoms out of the 10^7 atoms would be detected. In comparison to the extremely low LoD of ^{90}Sr at VERA, which is < 0.02 mBq [54], the LoD at CologneAMS is currently about 550 times higher. The present detection efficiency at CologneAMS is nearly four times larger than the radiometric LoD and the LoD of conventional AMS large accelerators (≥ 6 MV) [52, 53]. Consequently, until the measurement routine at CologneAMS is improved, no ^{90}Sr measurements of environmental samples can currently be performed using the ALIS setup.
At present, there are several challenges that require further investigation and time to solve them, e.g., injection losses with the ion cooler, transmission of SrF_3^- on the low-energy side, optimizing the detector pressure for the separation of $^{90}Sr^{3+}$ and $^{90}Zr^{3+}$, and low Zr suppression by laser photodetachment. By addressing these challenges, the LoD and the measurement routine will improve, enabling the measurement of ^{90}Sr in environmental samples.

5.3.2. Reference materials

The reported results of the AMS measurements performed with the ALIS setup used the reference materials Sr-11J and Sr-12J [98] to characterize the current performance of ion-laser-interaction assisted AMS measurements of ^{90}Sr at the 6 MV facility of CologneAMS [54]. These reference materials are routinely used at VERA for measurements of ^{90}Sr and were produced from the Japan Atomic Energy Agency (JAEA) and subsequently provided to VERA. Additionally, in-house made reference material was produced in a dilution series by Dominik Elchine of the Division of Nuclear Chemistry at the University of Cologne. This reference material will serve as the standard material for future measurements of ^{90}Sr at CologneAMS. To elaborate, the reference materials produced at Cologne are on the order of $^{90}\mathrm{Sr}/\mathrm{Sr} = 10^{-10,-11,-12,-13}$. The Cologne reference material, with the exception of the 10^{-10} material, was measured and characterized at VERA using the ILIAMS setup. The Sr-11J standard was used for normalization. The nominal

ratios of the reference materials previously mentioned are listed in Tab. 5.2. The Cologne reference materials were named using the following convention: The initials of the producer (DE), the order of magnitude (E-XX) and the radionuclide (90Sr), e.g., the 10^{-11} material is labeled DE_E-11_90Sr.
A typical energy loss spectrum for $^{90}Sr^{3+}$ in the four-anode GIC, for a reference material (Sr-11J) and a machine blank material at a buffer gas pressure of 1.06 Pa (optimal cooler transmission) using a detector pressure of around 8 mbar (bad separation) is shown in Fig. 5.15. The region of interest (ROI) for $^{90}Sr^{3+}$ is set after checking the position of the $^{90}Zr^{3+}$ events on a Zr-spiked target and a standard target. In order to ensure maximal efficiency, the ROI is set with the utmost precision, such that ideally no $^{90}Zr^{3+}$ is within the ROI during the measurement of non-spiked targets. This proved to be challenging due to the lack of a well defined separation in the detector. In general, quite a few events were detected in the ^{90}Sr ROI for some measurements on the machine blank sample, most likely indicating real $^{90}Sr^{3+}$ ions entering the detector. These events might stem from cross contamination in the ion source. This can be explained by the fact that all performed measurements were approximately 600 s long, which includes the measurements of the Sr-11J and Sr-12J standards. Consequently, the measured ^{90}Sr/Sr ratios on the blank samples may be slightly elevated due to cross contamination in the ion source. The reason for the long measurement times on the standard material was to gather enough ^{90}Sr events, as even on the Sr-11J samples the count rate was only 0.4 counts per second. The suboptimal Zr suppression with the 532 nm laser (see section 5.2.2.2) could also lead to elevated count rates in the $^{90}Sr^{3+}$ ROI. How-

Table 5.2.: Table of the nominal values of the ^{90}Sr reference materials from VERA, provided by the JAEA [98], and in-house made reference materials. Note that the nominal values of the Cologne standards have been characterized by AMS measurements at VERA [54] and will be used for future ^{90}Sr measurements at CologneAMS.

name	**^{90}Sr/Sr**	**reference date**
Sr-11J	$(3.751 \pm 0.045) \cdot 10^{-11}$	18.10.2021
Sr-12J	$(3.751 \pm 0.045) \cdot 10^{-12}$	18.10.2021
DE_E-11_90Sr	$(5.31 \pm 0.16) \cdot 10^{-11}$	28.02.2025
DE_E-12_90Sr	$(5.36 \pm 0.18) \cdot 10^{-12}$	28.02.2025
DE_E-13_90Sr	$(6.24 \pm 0.32) \cdot 10^{-13}$	28.02.2025

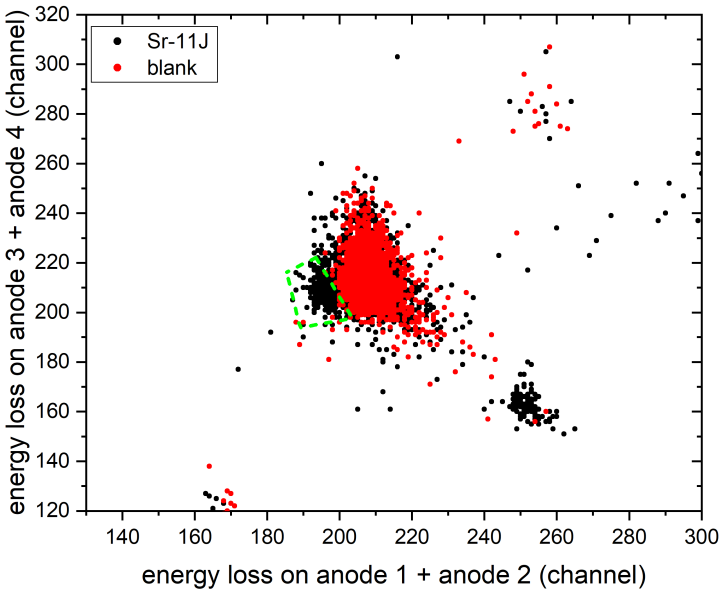

Figure 5.15.: Typical energy loss spectrum, displaying the energy loss on the third and fourth anode as a function of the energy loss on the first and second anode of the four-anode GIC, for a standard sample (Sr-11J, black) and a machine blank sample (red). The detector pressure was set to approximately 8 mbar. Note that the light green box marks the $^{90}Sr^{3+}$ ROI and that the buffer gas pressure was at 1.06 Pa of He.

ever, a Zr correction is used in the measurement evaluation of the measurement to compensate this problem.

The linearity of the the standard materials (Sr-11J and Sr-12J) following the evaluation of the AMS measurement are shown in Fig. 5.16. Prior to the normalization of the data, the measured ^{90}Sr/Sr ratios tend to be higher than the nominal values (Fig. 5.16), i.e., more $^{90}Sr^{3+}$ events are detected compared to the expected amount based on the measured $^{88}Sr^{3+}$ ion current. One potential explanation for is that the OFC used to measure the $^{88}Sr^{3+}$ ion current was not in an accurate position, resulting in an inaccurate measurement of the ion current. This could be the case because the OFC positioning was not checked again after extensive tuning prior to starting the AMS measurement, partly due to time constraints. Nevertheless, upon normalization to the Sr-11J standard, the measured ^{90}Sr/Sr of the Sr-12J does reproduce the nominal value quite nicely within 1σ of uncertainty. However, due to the rather high blank level, the blank correction adds a significant amount of uncertainty, resulting in a large relative uncertainty of 25%.

In summary, the blank level and, consequently, the LoD for ^{90}Sr is still very high (see section 5.3.1). Thus, the capability of the ALIS setup to measure material with $^{90}\mathrm{Sr}/\mathrm{Sr} \leq 10^{-12}$ is currently not feasible. Hence, the Sr-13J standard material was not measured, as it would not be distinguishable from the machine blank. Following the improvement of the measurement routine at CologneAMS, the reproducibility and linearity of standard material with isotopic ratios of $^{90}\mathrm{Sr}/\mathrm{Sr} \leq 10^{-12}$ will be investigated.

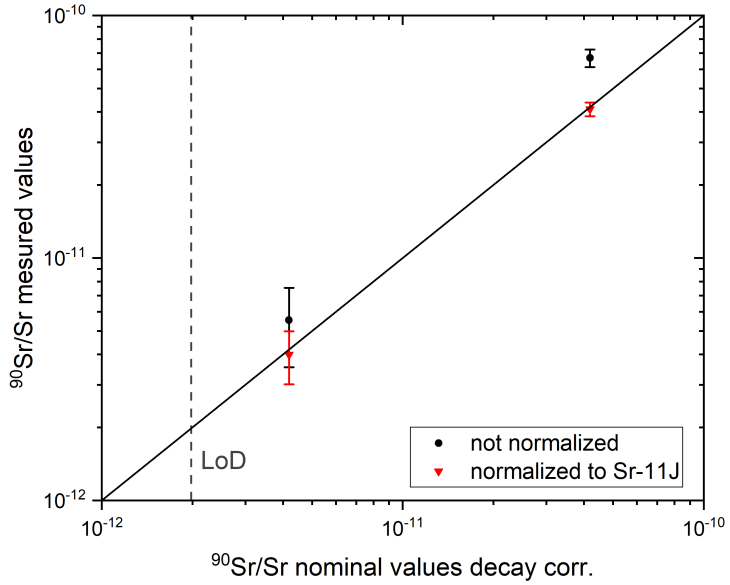

Figure 5.16.: Measured ^{90}Sr/Sr ratio by AMS as a function of the nominal ^{90}Sr/Sr ratio. The measurement was conducted at the 6 MV facility of CologneAMS using the ALIS setup. The solid black line represents a 1:1 agreement between the measured and decay corrected nominal values, while the dashed gray line represents the current LoD for ^{90}Sr. Without normalization (black), the measured ^{90}Sr/Sr ratios tend to be higher than the nominal values, suggesting that more $^{90}\mathrm{Sr}^{3+}$ events are detected than the $^{88}\mathrm{Sr}^{3+}$ ion current would imply. With normalization to Sr-11J (red), the Sr12-J material reproduces the 1:1 line within 1σ. However, the relative uncertainty for a 10^{-12} standard is rather high at 25% due to the high machine blank and subsequent blank correction. Note that the nominal values have been decay corrected to the 04.03.2025.

6. Conclusion and Outlook

In order to achieve the measurement of ^{90}Sr in soil and concrete samples on an industrial scale, i.e., hundreds up to a thousand samples per year, a fast, simple, and cost-efficient sample preparation and a measurement method with high abundance sensitivity and efficiency is required. Accelerator Mass Spectrometry fulfills both of these requirements, especially when using a gas-filled RFQ ion cooler for isobar suppression. Hence, in a collaboration of the University of Cologne and University of Vienna, a new ion cooler was developed and implemented as part of the ALIS setup at the 6 MV AMS facility of CologneAMS.

As a first step, the performance of the new ion cooler design was tested at a test bench setup at Vienna, which was built for this purpose specifically. The performance was characterized using $^{27}AlO^-$ and $^{63}Cu^-$ ion beams extracted with energies of 23.5 keV. The primary conclusions of this study were that, in principle, the new ion cooler does work as intended, i.e., no spark overs at high voltages up to 30 kV, the successful transmission of anions through the ion cooler, and the new guiding electrode structure works. Furthermore, the ion residence time of anions at varying guiding field strengths and buffer gas pressures was measured. The results of these measurements are comparable to the results of the ILIAMS ion cooler measurements, ranging on the order of ms. However, it was discovered that the new ion cooler design also exhibits some deficiencies, primarily the occurrence of significant ion beam losses during the injection into the RFQ, attributed to collisional detachment with buffer gas leaking out of the ion cooler.

In addition to the performance tests, and in a collaborative effort with my colleagues at Cologne, the ALIS setup was constructed from the ground up at CologneAMS. The ALIS setup includes a laser table with a 532 nm cw-laser of up to 18 W of output power, a 134-MC-SNICS ion source (loan from Vienna), a 90° bending magnet, the RFQ ion cooler and the high voltage platform, a 90° ESA, and a few

lenses and magnetic steerers. The total length of the ALIS setup is approximately 10 m and most components are remotely controllable, with the exception of a few ion cooler components.

Following the completion of the ALIS setup, a measurement routine for AMS measurements of ^{90}Sr was developed. The development of the measurement routine entailed the investigation and optimization of the transmission of $^{88}SrF_3^-$ through the ion cooler. The charge state yield distribution at a terminal voltage of 5 MV revealed that the Sr^{2+} charge state is the most populated charge state, with a yield of 34%. However, the inability of the switching magnet to deflect the Sr^{2+} ions with an energy of 13.1 MeV into the detector precludes the possibility of using this charge state. Consequently, the less populated charge state Sr^{3+}, with a yield of 22%, is used for AMS measurements. The transmission on the low-energy side after the ion cooler extraction is currently rather low at 34%. Conversely, the transmission on the high-energy side nearly reaches 100%. Depending on the buffer gas pressure, the isobar ^{90}Zr can be suppressed by a factor of 80 - 300. This suppression is achieved using ALIS and the 532 nm laser with a transmitted laser power of approximately 6 W. At present, the blank level is $^{90}Sr/Sr = (6.94 \pm 4.29) \cdot 10^{-13}$, which corresponds to a LoD for ^{90}Sr of 11 mBq (2.13 fg), with an overall detection efficiency of 0.045‰.

Parallel to the developments of the AMS measurement at CologneAMS, a new fast, simple, and cost-efficient sample preparation protocol for AMS measurements of ^{90}Sr in concrete and soil samples has been successfully developed. It is a largely modified version of the protocol by Honda et al. (2022) [97] with additional improvements from the work of Landstetter and Wallner (2006) [20]. The newly developed sample preparation protocol yields high chemical yields and quality factors, with averages for both parameters of approximately 90%. In comparison to the Honda protocol, the quality factor is improved by a factor of 1.7, which is interpreted as less CaF_2 and other contaminants present in the sample material following the fluoride precipitation. This directly impacts the counting statistics of ^{90}Sr, resulting in an improved AMS measurement efficiency of up to 70%. The newly developed protocol reduces the net working time required for one batch of samples, which generally contains between six to ten samples, down to roughly 40 h and it can be completed within four to five working days. That means, depending

on the experience, one person would be able to process 350 - 520 samples per year. For this work, a total of 55 samples were chemically processed and analyzed. These samples comprised of 22 soil samples, 24 concrete samples, one sediment sample, and eight processing blanks.
The validity of the sample preparation was tested by measuring numerous soil samples (IAEA-375 & IAEA-447) and concrete samples by ion-laser-interaction assisted AMS. Within $1\,\sigma$, the majority of the data from the analyzed samples accurately reproduce the nominal values for soil and are in agreement with the LSC results for concrete. It has been successfully demonstrated that a "leachate aliquot" approach, which consists of leaching a large sample (10 g) and taking a small liquid aliquot of the leachate for further processing, yields accurate and representative results for the entire sample. This approach significantly improves the problem of obtaining representative AMS results for large samples (> 5 g) without the necessity to fully process the entire sample. In addition to typical LSC nuclides for nuclear decommissioning already measurable by classical AMS, e.g., ^{41}Ca and ^{55}Fe [70, 71], it has been demonstrated that ion-laser-interaction assisted AMS measurements of ^{90}Sr is a fast, simple, cost-efficient, and competitive alternative to radiometric measurements for this purpose.
Despite these accomplishments, the current state achieved for the ALIS setup at the 6 MV AMS facility of CologneAMS does not permit the measurement of ^{90}Sr in environmental samples due to the high LoD. However, there are several known challenges that partially affect each other, including ion beam losses during injection into the ion cooler, low isobar suppression of ^{90}Zr via laser photodetachment, and the not well defined separation of $^{90}Sr^{3+}$ and $^{90}Zr^{3+}$ in the detector. These challenges require further investigations to be undertaken in the near future. Solving these major challenges will most likely result in significant improvements to the AMS measurement of ^{90}Sr at CologneAMS, thereby enabling the measurement of environmental samples. Nonetheless, the low LoD of ^{90}Sr at VERA in conjunction with the newly developed sample preparation protocol, clearly demonstrates the feasibility of ion-laser-interaction assisted AMS measurements of ^{90}Sr on an industrial scale.

A. Code of ion optic simulations at Vienna

In this Appendix, the used Limioptic II [93] code for the simulation of the ion cooler injection and ion cooler extraction at the Vienna test bench is shown. The ion cooler injection ranges from the ion source up to the aperture of the injection system, which is located right in front of the RFQ section of the ion cooler. The ion cooler extraction starts at the end of the RFQ section and ends at the Faraday Cup located at the end of the test bench setup.

Cooler injection code:

```
##########################################
Beam(2, 8.5, 2, 8.5, 0, 0, 1000) # (xmax, x'max, ymax, y'max, dk, dm, delta: 1...360)
##########################################

Drift(0.4) # (length)

######################
#Name('einzel lens 1')
#EinzelLens(INPUT[0]) # for automatic optimization (f, [R])
EinzelLens(0.25) # for ESA K=0.7 (f, [R])
######################

Drift(0.79) # (length)

######################
Name('slits')
Sli(0, 10, 0, 10) #slits fully open
#Waist() # potential waist position for automatic optimizaiton
######################
```

```
Drift(0.61) # (length)

######################
#Name('einzel lens 2')
#EinzelLens(INPUT[1]) #for automatic optimization (f, [R])
EinzelLens(2.53) # for ESA K=0.7 (f, [R])
######################

Drift(.315) # (length)

######################
Name('magnet entrance')
EdgeFocusing(0.75, 26.5, K=0.7)
MSA(0.75, 90, 12.5)
EdgeFocusing(0.75, 26.5, K=0.7)
Name('bending exit')
######################

Drift(1.345) # (length)

######################
Name('slits')
Sli(0, 6, 0, 6) #slits ±6 mm open
#Waist() #potential waist position for automatic optimization
######################

Drift(1.348) # (length)

######################
Name('quadrupole')
#QuadrupolRadFoc(INPUT[2], 0.10,30) #for automatic optimization QuadrupolRadFoc(30.31,
0.10, 30.0)
Drift(0.10) # approximated free drift between quadrupole coils (length)
#QuadrupolAxFoc(INPUT[3], 0.10,30) #for automatic optimization QuadrupolAxFoc(31.44,
0.10, 30.0)
######################

Drift(0.8735) # (length)

######################
Name('injection start')
Sli(0, 11, 0, 11) #use slits as aperture for the smaller grounding electrode
```

```
#Waist() #potential waist position for automatic optimization
######################

Drift(0.3125) # (length)

######################
Name('injection exit (end of ground electrode)')
Slit(0, 11, 0, 11) #use slits as aperture for the smaller grounding electrode
#Waist() #potential waist position for automatic optimization
#BeamProfile() #BeamProfile to check transmission of ions
######################

Drift(0.1) # (length)
```

Cooler extraction code:

```
##########################################
Beam(2, 8.5, 2, 8.5, 0, 0, 1000) # (xmax, x'max, ymax, y'max, dk, dm, delta: 1...360)
##########################################

####################
Name('extraction start')
AddGeo(0,50,0,30)
####################

Drift(0.3125) # (length)

####################
Name('extraction end (end of ground electrode)')
AddGeo(0,50,0,30)
####################

Drift(0.8063) # (length)

####################
Name('einzel lens 3')
#EinzelLens(INPUT[1]) # for automatic optimization (f, [R])
EinzelLens(0.74)
####################
```

```
Drift(1.365) #distance EL to Switcher

####################
Name('magnet')
EdgeFocusing(0.4064, 0.0, K=0.0) # 0; 0.7
MSA(0.4064, 30, 12.5) #beam pipe height 25mm!
EdgeFocusing(0.4064, 0.0, K=0.0) # 0; 0.7
####################

Drift(0.422) # (length)

####################
Name('slits')
Slit(0, 7, 0, 7) #slits used for transmission into Faraday cup (real slits are actually slightly further ahead, approx. 20 mm)
BeamProfile() #BeamProfile to check transmission of ions
Waist() #potential waist position for automatic optimization
####################

Drift(0.1) # (length)
```

B. Rur river batch: Additional sample information

The Appendix provides an overview of the samples obtained from the soil samplers at different sampling sites of the Rur river sample batch. The batch consists of three distinct sampling sites, with a total of 2 - 10 samples retrieved from each site. In Tab. B.1 the sampling sites, the internally used sample IDs, the depth and the coordinates of the sampling site are listed. For the sediment sample, two samples (sediment_3_1 & sediment_3_2) were collected. However, they were merged together to one singular sample prior to the sample preparation. Thus, in section 4.3.1 it is treated as one sample.

Table B.1.: Table summarizing the most important information of the samples from the Rur river batch. The two samples of the sediment sampling site were merged together prior to the sample preparation. Thus, only one sediment sample was processed and measured.

sample ID	depth (cm)	latitude (°)	longitude (°)	sampling site
1A	0 - 21	50.893433	6.379045	island
1B	21 - 30	50.893433	6.379045	island
1C	30 - 46	50.893433	6.379045	island
1D	46 - 58	50.893433	6.379045	island
1E	58 - 62	50.893433	6.379045	island
1F	62 - 71	50.893433	6.379045	island
1G	71 - 77	50.893433	6.379045	island
1H	77 - 84	50.893433	6.379045	island
1I	84 - 95	50.893433	6.379045	island

1J	95 - 101	50.893433	6.379045	island
2A	0 - 6	50.893906	6.379782	meadow
2B	6 - 8	50.893906	6.379782	meadow
2C	8 - 10	50.893906	6.379782	meadow
2D	10 - 12	50.893906	6.379782	meadow
2E	12 - 14	50.893906	6.379782	meadow
2F	14 - 20	50.893906	6.379782	meadow
2G	20 - 33	50.893906	6.379782	meadow
2H	33 - 56	50.893906	6.379782	meadow
2I	56 - 92	50.893906	6.379782	meadow
sediment_3_1	N/A	50.893490	6.380449	sediment
sediment_3_2	N/A	50.893490	6.380449	sediment

C. Complete sample list of all processed samples

This Appendix provides an overview of all samples that were processed for this work. All samples are grouped in accordance with their chronological order of processing, as indicated by their batch number. The internally used sample ID, the batch number, and the sample material are all summarized in Tab. C.1. For this work, a total of 55 samples were processed. The 55 samples are divided into 22 soil samples, 24 concrete samples, one sediment sample, and eight processing blanks. These samples were processed in 8 individual batches. However, in certain instances, bigger batches were divided into sub-batches, e.g., if concrete and soil samples of the same batch were processed separately or to avoid cross-contamination if the ^{90}Sr activity of samples is large. Assuming one batch takes around 40 h of working time, between 400 - 450 h were used for the sample preparation in total. Note that the results obtained by a small minority of the processed samples are not reported in this work, e.g., samples with the addition of NH_3 from batch Nr. 4, as they were additional tests for the development of the sample preparation and were ultimately rejected. Consequently those additional steps are not part of the newly developed protocol described in section 3.5.

Table C.1.: Table summarizing all samples that were processed for this work. The individual sample batches are listed in accordance with their chronological order of processing, as indicated by the batch number. The internally used sample ID and the processed sample material is listed as well.

Batch Nr.	sample ID	sample material
1	400	concrete (AVR)
1	401	concrete (AVR)

1	410	concrete (AVR)
1	411	concrete (AVR)
1	Blank_1	processing blank
2	330_0	concrete drill core (AVR)
2	330_2	concrete drill core (AVR)
2	330_4	concrete drill core (AVR)
2	330_6	concrete drill core (AVR)
2	330_8	concrete drill core (AVR)
2	Blank_2	processing blank
3	330_10	concrete drill core (AVR)
3	340_0	concrete drill core (AVR)
3	340_2	concrete drill core (AVR)
3	340_4	concrete drill core (AVR)
3	340_6	concrete drill core (AVR)
3	Blank_3	processing blank
4	IAEA-447_15M	moss soil (IAEA-447)
4	IAEA-447_15M_ash	moss soil (IAEA-447)
4	IAEA-447_8M (3)	moss soil (IAEA-447)
4	IAEA-447_8M_ash	moss soil (IAEA-447)
4	IAEA-447_15M_NH_3	moss soil (IAEA-447)
4	IAEA-447_15M_NH_3_ash	moss soil (IAEA-447)
4	IAEA-447_8M_NH_3	moss soil (IAEA-447)
4	IAEA-447_8M_NH_3_ash	moss soil (IAEA-447)
4	Blank_4	processing blank
5	375_100	soil (IAEA-375)
5	375_250	soil (IAEA-375)
5	375_500	soil (IAEA-375)
5	IAEA-447_a	moss soil (IAEA-447)
5	IAEA-447_b	moss soil (IAEA-447)
5	Blank_5	processing blank

6	1375_1	soil (Jülich)
6	1375_2	soil (Jülich)
6	Blank_6	processing blank
6	Beton_1_a	concrete (10 g approach)
6	Beton_1_b	concrete (10 g approach)
6	Beton_2_a	concrete (10 g approach)
6	Beton_2_b	concrete (10 g approach)
7	330_0_processed	concrete (Ca removal test)
7	330_0_residue	concrete (Ca removal test)
8	soil_Blank_8	processing blank
8	soil_1A	soil (Rur river, island)
8	soil_1E	soil (Rur river, island)
8	soil_1J	soil (Rur river, island)
8	soil_2A	soil (Rur river, meadow)
8	soil_2E	soil (Rur river, meadow)
8	soil_2I	soil (Rur river, meadow)
8	sediment_3	sediment (Rur river batch)
8	soil_11-1248	soil (Jülich)
8	concrete_Blank_8	processing blank
8	MZFR	concrete (Karlsruhe)
8	RFR	concrete (Dreden-Rossendorf)
8	KNK	concrete (Karlsruhe)
8	330_0	concrete (quality control)

Bibiliography

[1] W. Kutschera. "Applications of accelerator mass spectrometry". *International Journal of Mass Spectrometry* 349-350 (2013). 100 years of Mass Spectrometry, pp. 203–218. ISSN: 1387-3806. URL: https://www.sciencedirect.com/science/article/pii/S1387380613002091.

[2] W. Kutschera et al. "Atom counting with accelerator mass spectrometry". *Rev. Mod. Phys.* 95 (3 2023), p. 035006. URL: https://link.aps.org/doi/10.1103/RevModPhys.95.035006.

[3] Y. Shao et al. "A review of measurement methodologies and their applications to environmental ^{90}Sr". *Journal of Environmental Radioactivity* 192 (2018), pp. 321–333. ISSN: 0265-931X. URL: https://www.sciencedirect.com/science/article/pii/S0265931X18304636.

[4] X. Hou. "Liquid scintillation counting for determination of radionuclides in environmental and nuclear application". *Journal of Radioanalytical and Nuclear Chemistry* 318 (2018), pp. 1597–1628. ISSN: 3. URL: https://doi.org/10.1007/s10967-018-6258-6.

[5] R. Middleton and C. T. Adams. "A close to universal negative ion source". *Nuclear Instruments and Methods* 118.2 (1974), pp. 329–336. ISSN: 0029-554X. URL: https://www.sciencedirect.com/science/article/pii/0029554X7490634X.

[6] R. Middleton. "A versatile high intensity negative ion source". *Nuclear Instruments and Methods in Physics Research* 214.2 (1983), pp. 139–150. ISSN: 0167-5087. URL: https://www.sciencedirect.com/science/article/pii/016750878390580X.

[7] A. Annaluru et al. “HVE ion sources for medium and high-energy accelerator systems”. *Journal of Physics: Conference Series* 2743.1 (2024), p. 012027. URL: https://dx.doi.org/10.1088/1742-6596/2743/1/012027.

[8] H.-A. Synal et al. “MICADAS: A new compact radiocarbon AMS system”. *Nuclear Instruments and Methods in Physics Research Section B: Beam Interactions with Materials and Atoms* 259.1 (2007), pp. 7–13. ISSN: 0168-583X. URL: https://www.sciencedirect.com/science/article/pii/S0168583X07001942.

[9] A. E. Litherland. “Fundamentals of accelerator mass spectrometry”. *Philosophical Transactions of the Royal Society of London. Series A, Mathematical and Physical Sciences* 323 (1987), pp. 5–21. ISSN: 0029-554X. URL: http://doi-org.uaccess.univie.ac.at/10.1098/rsta.1987.0069.

[10] H. Glavish. “Magnet optics for beam transport”. *Nuclear Instruments and Methods in Physics Research* 189.1 (1981), pp. 43–53. ISSN: 0167-5087. URL: https://www.sciencedirect.com/science/article/pii/0029554X81901257.

[11] K. H. Purser. “Ultra-sensitive spectrometer for making mass and elemental analyses”. *US Patent* 4,037,100 (1977). URL: https://patents.google.com/patent/US4037100A/en.

[12] H.-A. Synal. “Developments in accelerator mass spectrometry”. *International Journal of Mass Spectrometry* 349-350 (2013), pp. 192–202. ISSN: 1387-3806. URL: https://doi.org/10.1016/j.ijms.2013.05.008.

[13] S. Jacob et al. “Ion beam interaction with stripper gas – Key for AMS at sub MeV”. *Nuclear Instruments and Methods in Physics Research Section B: Beam Interactions with Materials and Atoms* 172.1 (2000). 8th International Conference on Accelerator Mass Spectrometry, pp. 235–241. ISSN: 0168-583X. URL: https://www.sciencedirect.com/science/article/pii/S0168583X00002056.

[14] J. Lachner et al. "Detection of UH^{3+} and Th^{3+} molecules and 236U background studies with low-energy AMS". *Nuclear Instruments and Methods in Physics Research Section B: Beam Interactions with Materials and Atoms* 294 (2013). Proceedings of the Twelfth International Conference on Accelerator Mass Spectrometry, Wellington, New Zealand, 20-25 March 2011, pp. 364–368. ISSN: 0168-583X. URL: https://www.sciencedirect.com/science/article/pii/S0168583X12000997.

[15] M. Martschini et al. "New and upgraded ionization chambers for AMS at the Australian National University". *Nuclear Instruments and Methods in Physics Research Section B: Beam Interactions with Materials and Atoms* 438 (2019). ISSN: 0168-583X. URL: https://www.sciencedirect.com/science/article/pii/S0168583X18303550.

[16] S. Herb. "Developments at the Cologne 10 MV AMS system for 60Fe measurements". PhD thesis. University of Cologne, Inctitute for Nuclear Physics, 2023.

[17] L. Wacker et al. "Developments in AMS of ^{99}Tc". *Nuclear Instruments and Methods in Physics Research Section B: Beam Interactions with Materials and Atoms* 223-224 (2004), pp. 185–189. ISSN: 0168-583X. URL: https://doi.org/10.1016/j.nimb.2004.04.038.

[18] M. Paul. "Separation of isobars with a gas-filled magnet". *Nuclear Instruments and Methods in Physics Research Section B: Beam Interactions with Materials and Atoms* 52 (3 1990), pp. 315–321. ISSN: 0168-583X. URL: https://doi.org/10.1016/0168-583X(90)90429-X.

[19] K. Knie et al. "AMS at the Munich gas-filled analyzing magnet system GAMS". *Nuclear Instruments and Methods in Physics Research Section B: Beam Interactions with Materials and Atoms* 123 (1 1997), pp. 128–131. ISSN: 0168-583X. URL: https://doi.org/10.1016/S0168-583X(96)00753-7.

[20] A. Wallner et al. "^{60}Fe deposition during the late Pleistocene and the Holocene echoes past supernova activity". *Proceedings of the National Academy*

of Sciences 117.36 (2020), pp. 21873–21879. URL: https://www.pnas.org/doi/abs/10.1073/pnas.1916769117.

[21] M. Schiffer et al. "Method developments for accelerator mass spectrometry at CologneAMS, ^{53}Mn/^{3}He burial dating and ultra-small $^{14}CO_2$ samples". *Global and Planetary Change* 184 (2020), p. 103053. ISSN: 0921-8181. URL: https://www.sciencedirect.com/science/article/pii/S0921818119305387.

[22] G. Raisbeck et al. "Measurement of ^{10}Be with a tandetron accelerator operating at 2 MV". *Nuclear Instruments and Methods in Physics Research Section B: Beam Interactions with Materials and Atoms* 5 (2 1984), pp. 175–178. ISSN: 0168-583X. URL: https://doi.org/10.1016/0168-583X(84)90505-6.

[23] C. Vockenhuber et al. "Development of isobar separation for ^{182}Hf AMS measurements of astrophysical interest". *Nuclear Instruments and Methods in Physics Research Section B: Beam Interactions with Materials and Atoms* 259 (1 2007), pp. 250–255. ISSN: 0168-583X. URL: https://doi.org/10.1016/j.nimb.2007.01.223.

[24] P. Steier et al. "Comparison of methods for the detection of ^{10}Be with AMS and a new approach based on a silicon nitride foil stack". *International Journal of Mass Spectrometry* 444 (2019), p. 116175. ISSN: 1387-3806. URL: https://www.sciencedirect.com/science/article/pii/S1387380619301617.

[25] J. Eliades et al. "Negative ion–gas reaction studies using ion guides and accelerator mass spectrometry II: S^-, SO^- and Cl^- with NO_2 and N_2O". *Nuclear Instruments and Methods in Physics Research Section B: Beam Interactions with Materials and Atoms* 361 (2015). The Thirteenth Accelerator Mass Spectrometry Conference, pp. 300–306. ISSN: 0168-583X. URL: https://www.sciencedirect.com/science/article/pii/S0168583X15005807.

[26] W. E. Kieser et al. "RFQ Reaction Cells for AMS: Developments and Applications". *EPJ Web of Conferences* 63 (2013), p. 03005. URL: https://doi.org/10.1051/epjconf/20136303005.

[27] A. Litherland et al. “Isobar separation at very low energy for AMS”. *Nuclear Instruments and Methods in Physics Research Section B: Beam Interactions with Materials and Atoms* 259.1 (2007). Accelerator Mass Spectrometry, pp. 230–235. ISSN: 0168-583X. URL: https://www.sciencedirect.com/science/article/pii/S0168583X07002340.

[28] M. Martschini et al. “Selective laser photodetachment of intense atomic and molecular negative ion beams with the ILIAS RFQ ion beam cooler”. *International Journal of Mass Spectrometry* 415 (2017), pp. 9–17. ISSN: 1387-3806. URL: https://www.sciencedirect.com/science/article/pii/S1387380616302378.

[29] O. Forstner et al. “The ILIAS project for selective isobar suppression by laser photodetachment”. *Nuclear Instruments and Methods in Physics Research Section B: Beam Interactions with Materials and Atoms* 361 (2015). The Thirteenth Accelerator Mass Spectrometry Conference, pp. 217–221. ISSN: 0168-583X. URL: https://www.sciencedirect.com/science/article/pii/S0168583X15003596.

[30] E. L. Flannigan et al. “Characterization of the isobar separator for anions integrated into the A. E. Lalonde laboratory’s 3 MV AMS system”. *Nuclear Instruments and Methods in Physics Research Section B: Beam Interactions with Materials and Atoms* 528 (2022), pp. 34–39. ISSN: 0168-583X. URL: https://www.sciencedirect.com/science/article/pii/S0168583X22001975.

[31] M. Martschini et al. “5 YEARS OF ION-LASER INTERACTION MASS SPECTROMETRY—STATUS AND PROSPECTS OF ISOBAR SUPPRESSION IN AMS BY LASERS”. *Radiocarbon* 64.3 (2022), pp. 555–568. URL: https://www.cambridge.org/core/journals/radiocarbon/article/5-years-of-ionlaser-interaction-mass-spectrometrystatus-and-prospects-of-isobar-suppression-in-ams-by-lasers/9420439CC2CCE65EE204DC027BCC56EC.

[32] J. Eliades et al. “On-line ion chemistry for the AMS analysis of ^{90}Sr and ^{135,137}Cs”. *Nuclear Instruments and Methods in Physics Research Section B: Beam Interactions with Materials and Atoms* 294 (2013). Proceedings

of the Twelfth International Conference on Accelerator Mass Spectrometry, Wellington, New Zealand, 20-25 March 2011, pp. 361–363. ISSN: 0168-583X. URL: https://www.sciencedirect.com/science/article/pii/S0168583X11010615.

[33] D. MacMahon et al. "Convergence of techniques for the evaluation of discrepant data". *Applied Radiation and Isotopes* 60.2 (2004). Proceedings of the 14th International Conference on Radionuclide Metrology and its Applications, ICRM 2003, pp. 275–281. ISSN: 0969-8043. URL: https://www.sciencedirect.com/science/article/pii/S0969804303003221.

[34] E. E. Lewis. *Fundamental of Nuclear Reactor Physics*. Vol. 1. Academic Press, 2008. ISBN: 978-0-12-370631-7. URL: https://www.sciencedirect.com/book/9780123706317/fundamentals-of-nuclear-reactor-physics.

[35] O. Iwamoto et al. "Japanese evaluated nuclear data library version 5: JENDL-5". *Journal of Nuclear Science and Technology* 60.1 (2023), pp. 1–60. URL: https://doi.org/10.1080/00223131.2022.2141903.

[36] A. Koning et al. "TENDL: Complete Nuclear Data Library for Innovative Nuclear Science and Technology". *Nuclear Data Sheets* 155 (2019). Special Issue on Nuclear Reaction Data, pp. 1–55. ISSN: 0090-3752. URL: https://www.sciencedirect.com/science/article/pii/S009037521930002X.

[37] A. A. Yaroshevsky. "Abundances of chemical elements in the Earth's crust". *Geochemistry International* 44 (1 2006), pp. 48–55. ISSN: 1556-1968. URL: https://doi.org/10.1134/S001670290601006X.

[38] T. R. England and B. F. Rider. "Evaluation and compilation of fission product yields 1993 (LA-SUB–94-170)". *IAEA report* (1995). URL: http://inis.iaea.org/search/search.aspx?orig_q=RN:26035261.

[39] J. Eikenberg et al. "Anthropogenic radionuclide emissions into the environment". *Geological Society Special Publication* 236 (2004), pp. 143–151. URL: https://pubs.geoscienceworld.org/gsl/books/edited-volume/1619/chapter-abstract/107409391/Anthropogenic-radionuclide-emissions-into-the?redirectedFrom=fulltext.

[40] Q.-H. Hu et al. “Sources of anthropogenic radionuclides in the environment: a review”. *Journal of Environmental Radioactivity* 101.6 (2010), pp. 426–437. ISSN: 0265-931X. URL: https://www.sciencedirect.com/science/article/pii/S0265931X08001392.

[41] K. Hirose et al. “Annual Deposition of Sr-90, Cs-137 and Pu-239, 240 from the 1961-1980 Nuclear Explosions: A Simple Model”. *Journal of the Meteorological Society of Japan. Ser. II* 65.2 (1987), pp. 259–277. URL: https://www.jstage.jst.go.jp/article/jmsj1965/65/2/65_2_259/_article.

[42] International Atomic Energy Agency Kinly, D. III (Ed.). “Chernobyl’s legacy: Health, environmental and socio-economic impacts and recommendations to the Governments of Belarus, the Russian Federation and Ukraine The Chernobyl Forum”. *International Atomic Energy Agency (IAEA)* INIS-XA–903 (2006). URL: http://inis.iaea.org/search/search.aspx?orig_q=RN:37086935.

[43] P. Povinec et al. “Radiostrontium in the Western North Pacific: Characteristics, Behavior, and the Fukushima Impact”. *Environmental Science & Technology* 46.28 (1987), pp. 10356–10363. URL: https://doi.org/10.1021/es301997c.

[44] R. Periáñez et al. “Numerical Modeling of the Releases of ^{90}Sr from Fukushima to the Ocean: An Evaluation of the Source Term”. *Environmental Science & Technology* 47.21 (2013), pp. 12305–12313. URL: https://doi.org/10.1021/es4031408.

[45] J. Gray et al. “Discharges to the environment from the Sellafield site, 1951-1992”. *Journal of Radiological Protection* 15.2 (1995), p. 99. URL: https://dx.doi.org/10.1088/0952-4746/15/2/001.

[46] International Atomic Energy Agency. “Inventory of accidents and losses at sea involving radioactive material”. *International Atomic Energy Agency (IAEA)* IAEA-TECDOC–1242 (2001). URL: http://inis.iaea.org/search/search.aspx?orig_q=RN:32051569.

[47] K. Kossert and H. Schrader. “Activity standardization by liquid scintillation counting and half-life measurements of ^{90}Y”. *Applied Radiation and Isotopes* 60.5 (2004), pp. 741–749. ISSN: 0969-8043. URL: https://www.sciencedirect.com/science/article/pii/S0969804304000077.

[48] H. Amano and N. Yanase. “Measurement of ^{90}Sr in environmental samples by cation-exchange and liquid scintillation counting”. *Talanta* 37.6 (1990), pp. 585–590. ISSN: 0039-9140. URL: https://www.sciencedirect.com/science/article/pii/003991409080200Y.

[49] D. Rao et al. “Application of Cherenkov radiation counting for determination of ^{90}Sr in environmental samples”. *Journal of Environmental Radioactivity* 48.1 (2000), pp. 49–57. ISSN: 0265-931X. URL: https://www.sciencedirect.com/science/article/pii/S0265931X99000533.

[50] Z. Zhou et al. “Recent Development on Determination of Low-Level ^{90}Sr in Environmental and Biological Samples: A Review”. *Molecules* 28.1 (2023). ISSN: 1420-3049. URL: https://www.mdpi.com/1420-3049/28/1/90.

[51] N. Vajda and C.-K. Kim. “Determination of radiostrontium isotopes: A review of analytical methodology”. *Applied Radiation and Isotopes* 68.12 (2010), pp. 2306–2326. ISSN: 0969-8043. URL: https://www.sciencedirect.com/science/article/pii/S0969804310002320.

[52] S. Tumey et al. “Further development of accelerator mass spectrometry for the measurement of ^{90}Sr at Lawrence Livermore National Laboratory”. *Journal of Radioanalytical and Nuclear Chemistry* 282 (2009). 100 years of Mass Spectrometry, pp. 821–824. ISSN: 1588-2780. URL: https://doi.org/10.1007/s10967-009-0327-9.

[53] K. Sasa et al. “A sensitive method for Sr-90 analysis by accelerator mass spectrometry”. *Journal of Nuclear Science and Technology* 58.1 (2021), pp. 72–79. URL: https://doi.org/10.1080/00223131.2020.1801530.

[54] M. Martschini. personal communication. 2025.

[55] J. Lachner et al. “Highly sensitive ^{26}Al measurements by Ion-Laser- InterAction Mass Spectrometry”. *International Journal of Mass Spectrometry* 465 (2021), p. 116576. ISSN: 1387-3806. URL: https://www.sciencedirect.com/science/article/pii/S1387380621000567.

[56] W. Bu et al. “Mass spectrometry for the determination of fission products ^{135}Cs, ^{137}Cs and ^{90}Sr: A review of methodology and applications”. *Spectrochimica Acta Part B: Atomic Spectroscopy* 119 (2016), pp. 65–75. ISSN: 0584-8547. URL: https://doi.org/10.1016/j.sab.2016.03.008.

[57] N. Kavasi and S. Sahoo. “Method for ^{90}Sr Analysis in Environmental Samples Using Thermal Ionization Mass Spectrometry with Daly Ion-Counting System”. *Analytical Chemistry* 91 (2019), pp. 2964–2969. ISSN: 4. URL: https://doi.org/10.1021/acs.analchem.8b05184.

[58] J. Feuerstein et al. “Determination of ^{90}Sr in soil samples using inductively coupled plasma mass spectrometry equipped with dynamic reaction cell (ICP-DRC-MS)”. *Journal of Environmental Radioactivity* 99.11 (2008), pp. 1764–1769. ISSN: 0265-931X. URL: https://www.sciencedirect.com/science/article/pii/S0265931X08001173.

[59] T. Ohno et al. “Determination of strontium 90 in environmental samples by triple quadrupole ICP-MS and its application to Fukushima soil samples”. *J. Anal. At. Spectrom.* 33 (6 2018), pp. 1081–1085. URL: http://dx.doi.org/10.1039/C8JA00017D.

[60] J. Aoki et al. “Direct Quantification of Attogram Levels of Strontium-90 in Microscale Biosamples Using Isotope Dilution-Thermal Ionization Mass Spectrometry Assisted by Quadrupole Energy Filtering”. *Analytical Chemistry* 95 (2009), pp. 4932–4939. ISSN: 11. URL: https://doi.org/10.1021/acs.analchem.2c04844.

[61] Bundesrepublik Deutschland. *Verordnung zum Schutz vor der schädlichen Wirkung ionisierender Strahlung*. last accessed: 10 February 2025. 2018. URL: https://www.bmuv.de/gesetz/verordnung-zum-schutz-vor-der-schaedlichen-wirkung-ionisierender-strahlung.

[62] Bundesrepublik Österreich. *Gesamte Rechtsvorschrift für Allgemeine Strahlenschutzverordnung*. last accessed: 10 February 2025. 2020. URL: https://www.ris.bka.gv.at/GeltendeFassung.wxe?Abfrage=Bundesnormen&Gesetzesnummer=20011249.

[63] L. Hahn et al. *Der Versuchsreaktor AVR - Entstehung, Betrieb und Störfälle (Langfassung)*. Tech. rep. last accessed: 15.03.2025. 2014. URL: https://www.fz-juelich.de/de/aktuelles/news/pressemitteilungen/copy_of_2014/docs/bericht-avr-expertengruppe_lang?expand=translations,fzjsettings,nearest-institut.

[64] R. Moormann. "Fission Product Transport and Source Terms in HTRs: Experience from AVR Pebble Bed Reactor". *Science and Technology of Nuclear Installations* 2008.1 (2008), p. 597491. URL: https://onlinelibrary.wiley.com/doi/abs/10.1155/2008/597491.

[65] *The NEA cooperative program on decommissioning — a decade of progress*. last accessed: 18.04.2025. 2006. URL: https://inis.iaea.org/records/5sdkm-wx790.

[66] K. C. Stamoulis et al. "Strontium-90 concentration measurements in human bones and teeth in Greece". *Science of The Total Environment* 229 (3 1999), pp. 165–182. ISSN: 0048-9697. URL: https://doi.org/10.1016/S0048-9697(99)00052-2.

[67] P. Froidevaux et al. "Retention half times in the skeleton of plutonium and 90Sr from above-ground nuclear tests: A retrospective study of the Swiss population". *Chemosphere* 80.5 (2010), pp. 519–524. ISSN: 0045-6535. URL: https://www.sciencedirect.com/science/article/pii/S0045653510004856.

[68] K. Mück et al. "The Long-term Decrease of ^{90}Sr in the Environment and its Transfer to Man after a Nuclear Fallout". *Radiation Protection Dosimetry* 94.3 (Apr. 2001), pp. 251–259. ISSN: 0144-8420. URL: https://doi.org/10.1093/oxfordjournals.rpd.a006497.

[69] J. M. Gould et al. "Strontium-90 in Deciduous Teeth as a Factor in Early Childhood Cancer". *International Journal of Health Services* 30.3 (2000), pp. 515–539. eprint: https://doi.org/10.2190/FTL4-HNG0-BELK-5EMH. URL: https://doi.org/10.2190/FTL4-HNG0-BELK-5EMH.

[70] S. Merchel et al. "Evaluation of a sensitive, reasonable, and fast detection method for ^{55}Fe in steel". *Journal of Radioanalytical and Nuclear Chemistry* 330 (2021), pp. 727–735. ISSN: 3. URL: https://link.springer.com/article/10.1007/s10967-021-08000-7.

[71] D. Hampe et al. "Determination of ^{41}Ca with LSC and AMS: method development, modifications and applications". *Journal of Radioanalytical and Nuclear Chemistry* 296 (2013), pp. 617–624. ISSN: 2. URL: https://link.springer.com/article/10.1007/s10967-012-2145-8.

[72] V. N. Egorov et al. "^{90}Sr and ^{137}Cs in the Black Sea after the Chernobyl NPP accident: inventories, balance and tracer applications". *Journal of Environmental Radioactivity* 43 (2 1999), pp. 137–155. ISSN: 0265-931X. URL: https://doi.org/10.1016/S0265-931X(98)00088-5.

[73] M. A. V. Wasserman et al. "Analysing the behaviour of ^{90}Sr and stable Sr in highly weathered soils: Soil to plant transfer factor and geochemical partitioning". *Journal of Environmental Radioactivity* 271 (2024), p. 107319. ISSN: 0265-931X. URL: https://www.sciencedirect.com/science/article/pii/S0265931X23002126.

[74] L. Dewiere et al. "^{90}Sr migration to the geo-sphere from a waste burial in the Chernobyl exclusion zone". *Journal of Environmental Radioactivity* 74 (1 2004), pp. 139–150. ISSN: 0265-931X. URL: https://doi.org/10.1016/j.jenvrad.2004.01.019.

[75] S. Silber et al. "Two-year clinical follow-up of ^{90}Sr/^{90}Y β-radiation versus placebo control for the treatment of in-stent restenosis". *American Heart Journal* 149.4 (2005), pp. 689–694. ISSN: 0002-8703. URL: https://www.sciencedirect.com/science/article/pii/S0002870304006143.

[76] V. M. L. Cohen et al. “The Use of Strontium-90 Beta Radiotherapy as Adjuvant Treatment for Conjunctival Melanoma”. *Journal of Oncology* 2013.1 (2013), p. 349162. URL: https://onlinelibrary.wiley.com/doi/abs/10.1155/2013/349162.

[77] X. Wang et al. “Critical design features of thermal-based radioisotope generators: A review of the power solution for polar regions and space”. *Renewable and Sustainable Energy Reviews* 119 (2020), p. 109572. ISSN: 1364-0321. URL: https://www.sciencedirect.com/science/article/pii/S1364032119307804.

[78] J. S. Dustin and R. Borrelli. “Assessment of alternative radionuclides for use in a radioisotope thermoelectric generator”. *Nuclear Engineering and Design* 385 (2021), p. 111475. ISSN: 0029-5493. URL: https://www.sciencedirect.com/science/article/pii/S0029549321004271.

[79] R. O’Brien et al. “Safe radioisotope thermoelectric generators and heat sources for space applications”. *Journal of Nuclear Materials* 377.3 (2008), pp. 506–521. ISSN: 0022-3115. URL: https://www.sciencedirect.com/science/article/pii/S0022311508002420.

[80] R. Liljestrand et al. “Target thickness uniformity gauge”. *Nuclear Instruments and Methods* 138 (3 1976), pp. 471–477. ISSN: 0029-554X. URL: https://doi.org/10.1016/0029-554X(76)90313-X.

[81] K. Bikit et al. “Application of ^{90}Sr for industrial purposes and dose assessment”. *Radiation Physics and Chemistry* 179 (2021), p. 109260. ISSN: 0969-806X. URL: https://www.sciencedirect.com/science/article/pii/S0969806X20313426.

[82] P. Rappaport. “The Electron-Voltaic Effect in $p-n$ Junctions Induced by Beta-Particle Bombardment”. *Phys. Rev.* 93 (1 1954), pp. 246–247. URL: https://link.aps.org/doi/10.1103/PhysRev.93.246.2.

[83] Q. Cui et al. “A ^{90}Sr/^{90}Y-radioisotope battery based on betavoltaic and beta-photovoltaic dual effects”. *Materials Science in Semiconductor Processing* 179 (2024), p. 108493. ISSN: 1369-8001. URL: https://www.sciencedirect.com/science/article/pii/S1369800124003895.

[84] W. Paul. "Electromagnetic traps for charged and neutral particles". *Rev. Mod. Phys.* 62 (3 1990), pp. 531–540. URL: https://link.aps.org/doi/10.1103/RevModPhys.62.531.

[85] F. Herfurth et al. "A linear radiofrequency ion trap for accumulation, bunching, and emittance improvement of radioactive ion beams". *Nuclear Instruments and Methods in Physics Research Section A: Accelerators, Spectrometers, Detectors and Associated Equipment* 469.2 (2001), pp. 254–275. ISSN: 0168-9002. URL: https://www.sciencedirect.com/science/article/pii/S0168900201001681.

[86] Y. Liu et al. "Collisional cooling of negative-ion beams". *Nuclear Instruments and Methods in Physics Research Section B: Beam Interactions with Materials and Atoms* 187.1 (2002), pp. 117–131. ISSN: 0168-583X. URL: https://www.sciencedirect.com/science/article/pii/S0168583X01008448.

[87] O. Marchhart et al. "First performance tests of the new advanced radiofrequency quadrupole for ALIS at the test bench setup at VERA". *Nuclear Instruments and Methods in Physics Research Section B: Beam Interactions with Materials and Atoms* 565 (2025), p. 165751. ISSN: 0168-583X. URL: https://www.sciencedirect.com/science/article/pii/S0168583X25001417.

[88] A. Kellerbauer et al. "Buffer gas cooling of ion beams". *Nuclear Instruments and Methods in Physics Research Section A: Accelerators, Spectrometers, Detectors and Associated Equipment* 469.2 (2001), pp. 276–285. ISSN: 0168-9002. URL: https://www.sciencedirect.com/science/article/pii/S0168900201002868.

[89] J. C. Rienstra-Kiracofe et al. "Atomic and Molecular Electron Affinities: Photoelectron Experiments and Theoretical Computations". *Chemical Reviews* 102 (1 2002), pp. 231–282. URL: https://doi.org/10.1021/cr990044u.

[90] J.-F. Alary et al. "Isobar Separator for Anions: Current status". *Nuclear Instruments and Methods in Physics Research Section B: Beam Interactions*

with Materials and Atoms 361 (2015), pp. 197–200. ISSN: 0168-583X. URL: https://doi.org/10.1016/j.nimb.2015.03.059.

[91] M. Schiffer et al. "An advanced radio-frequency quadrupole ion cooler for accelerator mass spectrometry". *Nuclear Instruments and Methods in Physics Research Section B: Beam Interactions with Materials and Atoms* 528 (2022), pp. 27–33. ISSN: 0168-583X. URL: https://www.sciencedirect.com/science/article/pii/S0168583X22001847.

[92] O. Marchhart. "Exploration study for trace detection of long lived fission products at VERA". MA thesis. University of Vienna, Faculty of Physics, 2020.

[93] A. Stolz. *Limioptic II*. Version 20201230. 2020. URL: https://alexander-stolz.github.io/limioptic/.

[94] H. Wollnik. *Optics of Charged Particles*. Academic Press, 1987. ISBN: 978-0-323-15678-3. URL: https://www.lehmanns.de/shop/technik/27035522-9780323156783-optics-of-charged-particles.

[95] A. M. Stolz. "Untersuchung der Ionenoptik des Kölner AMS-Massenspektrometers und Vergleich der ionenoptischen Berechnungen mit realen Messeinstellungen für ausgesuchte Radioisotope ". MA thesis. University of Cologne, Faculty of Mathematics and Natural Sciences, 2012.

[96] Scientific Instrument Services by Adaptas. *Simion*. Version 8.1.1.32. 2013. URL: https://www.sisweb.com/simion.htm.

[97] M. Honda et al. "Novel ^{90}Sr analysis of environmental samples by Ion-Laser InterAction Mass Spectrometry". *Anal. Methods* 14 (28 2022), pp. 2732–2738. URL: http://dx.doi.org/10.1039/D2AY00604A.

[98] H. Honda. personal communication. 2025.

[99] V. Strachnov et al. "Report on the intercomparison run IAEA-375: Radionuclides in Soil". *IAEA/AL/75, IAEA* (1996). last acccessed: 17.12.2024. URL: https://nucleus.iaea.org/sites/AnalyticalReferenceMaterials/Shared%5C%20Documents/ReferenceMaterials/Radionuclides/IAEA-375/AL_075.PDF.

[100] A. Shakhashiro et al. “IAEA-447: A new certified reference material for environmental radioactivity measurements”. *Applied Radiation and Isotopes* 70.8 (2012), pp. 1632–1643. ISSN: 0969-8043. URL: https://www.sciencedirect.com/science/article/pii/S0969804312002254.

[101] D. Walther and D. Degering and S. Großmann and M. Bothe and R. Husar. *VKTA Prüfbericht zur Bestimmung von Radionukliden, Prüfbericht Nr. 3233.6*. The data of the measurement report is not publicly available, but was provided by the JEN mbH. 2023.

[102] S. Merchel et al. “Attempts to understand potential deficiencies in chemical procedures for AMS”. *Nuclear Instruments and Methods in Physics Research Section B: Beam Interactions with Materials and Atoms* 456 (2019), pp. 186–192. ISSN: 0168-583X. URL: https://www.sciencedirect.com/science/article/pii/S0168583X1930309X.

[103] C. Landstetter and G. Wallner. “Determination of strontium-90 in deer bones by liquid scintillation spectrometry after separation on Sr-specific ion exchange columns”. *Journal of Environmental Radioactivity* 87.3 (2006), pp. 315–324. URL: https://www.sciencedirect.com/science/article/pii/S0265931X06000026.

[104] M. L. Dietz et al. “An Improved Method for Determining ^{89}Sr and ^{90}Sr in Urine”. *Health Physics* 61 (1991). ISSN: 6. URL: https://journals.lww.com/health-physics/fulltext/1991/12000/an_improved_method_for_determining_89sr_and_90sr.20.aspx.

[105] R. C. E. Philip Horwitz and M. L. Dietz. “A NOVEL STRONTIUM SELECTIVE EXTRACTION CHROMATOGRAPHIC RESIN*”. *Solvent Extraction and Ion Exchange* 10.2 (1992), pp. 313–336. URL: https://doi.org/10.1080/07366299208918107.

[106] E. P. Horwitz et al. “Separation and preconcentration of strontium from biological, environmental, and nuclear waste samples by extraction chromatography using a crown ether”. *Analytical Chemistry* 63.5 (1991), pp. 522–525. URL: https://doi.org/10.1021/ac00005a027.

[107] TRISKEM International. *SR RESIN, particle size: 100-150µg*. Last accessed: 03 July 2024. URL: https://www.triskem-international.com/catalog/products/resins-and-accessories/sr-resin/bl,product,412,0.

[108] Autodesk Inc. *Fusion360*. Version 2.0.17954. URL: https://www.autodesk.com/.

[109] F. Hinterberger. *Physik der Teilchenbeschleuniger und Ionenoptik*. Vol. 2. Springer, 2008. ISBN: 978-3-540-75281-3. URL: https://link.springer.com/book/10.1007/978-3-540-75282-0.

[110] M. Marock. "Setup of a mass separator for optimisation of negative ion sources". MA thesis. University of Cologne, Faculty of Mathematics and Natural Sciences, 2017.

[111] X.-L. Zhao et al. "Studies of anions from sputtering I: Survey of MF_n^-". *Nuclear Instruments and Methods in Physics Research Section B: Beam Interactions with Materials and Atoms* 268.7 (2010), pp. 807–811. ISSN: 0168-583X. URL: https://www.sciencedirect.com/science/article/pii/S0168583X09010854.

[112] P. Gaggl. "Multiphysics simulation of negative ions in a gas filled RF-quadru pole". MA thesis. University of Vienna, Faculty of Physics, 2021.